
Remote sensing of the diurnal cycle of optically thin cirrus clouds

Dipl.-Met. Stephan Kox

Ludwig-Maximilians-Universität München



Meteorologisches Institut München

Juni 2012

Remote sensing of the diurnal cycle of optically thin cirrus clouds

Dipl.-Met. Stephan Kox

Dissertation

durchgeführt am

Deutschen Zentrum für Luft- und Raumfahrt



vorgelegt von

Dipl.-Met. Stephan Kox

aus München

München, den 28.06.2012

Gutachter der Dissertation:

Erstgutachter: Prof. Dr. Bernhard Mayer

Zweitgutachter: apl. Prof. Dr. Ulrich Schumann

Tag der mündlichen Prüfung: 19.11.2012

Zusammenfassung

Eiswolken und insbesondere hohe Zirruswolken bedecken im globalen jährlichen Mittel bis zu 30 % der Erde und haben deshalb einen signifikanten Einfluß auf das Klima. Eine Besonderheit hoher Eiswolken ist, dass sie einen wärmenden Effekt auf das System Erde und Atmosphäre besitzen können. Dieser wärmende Effekt wird u. a. durch tägliche und saisonale Variationen der optischen Eigenschaften beeinflusst. Um genaue Messungen der optischen Eigenschaften von Aerosolen und Zirruswolken zu erhalten, wurde 2006 die „Cloud-Aerosol Lidar and Infrared Pathfinder Satellite Observations“ (CALIPSO) Mission in einen polaren Orbit gestartet. Mit Hilfe des Hauptinstrumentes, des „Cloud-Aerosol Lidar with Orthogonal Polarization“ (CALIOP), können nun optische Eigenschaften von Aerosol- und dünnen Wolkenschichten mit bisher unerreichter Genauigkeit und Sensitivität bestimmt werden. Allerdings erlaubt dieser Orbit mit einer Wiederkehrdauer von mehr als zwei Wochen keine Ableitung von Tagesgängen der optischen Eigenschaften und des Bedeckungsgrades von Zirruswolken, weshalb in dieser Arbeit der Wolkensensor „Spinning Enhanced Visible and Infrared Imager“ (SEVIRI) auf dem geostationären „METEOSAT Second Generation“ (MSG) Satelliten benutzt wird. SEVIRI deckt mit seinen Messungen fast ein Drittel der Erde ab und reicht von 80° N bis 80° S und von 80° W bis 80° E bei einer räumlichen Auflösung von bis zu 3 km x 3 km im Nadir und einer zeitlichen Auflösung von 15 Minuten.

Im Rahmen dieser Arbeit wurde ein gänzlich neuer Ansatz verfolgt, um die Vorteile beider Instrumente (die hohe Sensitivität und Genauigkeit von CALIOP und die hohe zeitliche und räumliche Auflösung von SEVIRI) miteinander zu verbinden: Der „Cirrus Optical properties derived from CALIOP and SEVIRI during day and night“ (COCS) Algorithmus basiert auf dem Prinzip künstlicher Neuronaler Netze und leitet die optischen Dicken von Zirruswolken und deren Oberkantenhöhen aus Messungen der Infrarotkanäle des Instrumentes SEVIRI ab, was Beobachtungen sowohl in der Nacht als auch am Tage ermöglicht. Dieses Neuronale Netz wurde mit gleichzeitigen Messungen der optischen Dicken und Höhen der Wolkenoberkante von CALIOP trainiert. In dieser Arbeit wird die Entwicklung von COCS und die Validierung mit zwei unterschiedlichen Lidar-Messungen beschrieben, mit denen von CALIOP und mit denen des flugzeuggetragenen „High Spectral Resolution Lidar“ (HSRL). Die Validierungen zeigen die hohe Genauigkeit des hier entwickelten Algorithmus in der Ableitung der optischen Dicken und Höhen der Wolkenoberkante von Zirruswolken. Zusätzlich wurden auch Vergleiche der COCS-Ergebnisse mit zwei weiteren auf SEVIRI basierenden Algorithmen durchgeführt: Zum einen mit dem „METEOSAT Cirrus Detection Algorithm 2“ (MECiDA-2), welcher ebenfalls die thermischen Infrarotkanäle benutzt, zum anderen mit dem „Algorithm for the Physical Investigation of Clouds with SEVIRI“ (APICS), welcher zur Ableitung der optischen Eigenschaften von Wolken sowohl auf den Infrarotkanälen als auch auf Kanälen im sichtbaren Spektral-

bereich basiert.

Die Validierung zeigt hervorragende Ergebnisse für die Erkennung von Zirruswolken mit einer Fehldetektionsrate von unter 5 % und einer Detektionseffizienz von bis zu 99 % ab einer optischen Dicke von $\tau = 0.1$. Ebenfalls wird eine Standardabweichung von $\sigma_\tau = 0.25$ für die optische Dicke und $\sigma_z = 0.75$ km für die Höhe der Wolkenoberkante nachgewiesen. Basierend auf fünf Jahren prozessierter COCS-Daten werden die Tagesgänge von Zirruswolken in verschiedenen Regionen der Erde analysiert und diskutiert. Die Ergebnisse zeigen ausgeprägte Tagesgänge des Zirrusbedeckungsgrades und der optischen Dicke, welche sich von den Vorhersagen des „European Centre for Medium-range Weather Forecasts“ (ECMWF) unterscheiden. Eine Betrachtung des Bedeckungsgrades hoher Wolken, vorhergesagt durch das ECMWF, und der Ergebnisse des COCS Algorithmus zeigt gut übereinstimmende Tagesgänge in konvektiven Regionen, während Unterschiede in nicht-konvektiven Regionen über dem Nord- (NAR) und Südatlantik (SAR) sichtbar werden. Generell wird vor allem in diesen Regionen ein höherer Bedeckungsgrad mit Unterschieden von 3 – 10 % durch COCS errechnet.

Abschließend werden die Unterschiede der NAR und SAR diskutiert, da im Nordatlantik einer der meist frequentierten ozeanischen Flugkorridore liegt. Hier mischen sich die heißen Flugzeugabgase mit kalten Luftmassen und führen zur Bildung von Kondensstreifen. Diese Kondensstreifen verlieren mit der Zeit ihre lineare Form und können anschließend nicht mehr von natürlich entstandenen Zirruswolken unterschieden werden. Grundsätzlich zeigt sich hier eine starke Korrelation des Tagesganges von Bedeckungsgrad und optischer Dicke der Zirruswolken mit der Luftverkehrsdichte. Es werden Unterschiede von bis zu 3 % im Bedeckungsgrad zwischen NAR und SAR detektiert.

Summary

Aim of this thesis is the retrieval of diurnal variations of cirrus cloud optical properties. Ice clouds and especially cirrus clouds cover on average up to 30 % of the Earth and are therefore important for climate. High ice clouds hold an exceptional position within the large variety of clouds, since they generate positive net forcing and therefore make a contribution to warming of Earth's atmosphere. This heating effect is strongly modified by the diurnal and seasonal variations of the optical properties of cirrus clouds. In order to determine optical properties of aerosols and clouds, the Cloud-Aerosol Lidar and Infrared Pathfinder Satellite Observations (CALIPSO) mission was launched into a polar orbit in 2006. Equipped with its main instrument, the Cloud-Aerosol Lidar with Orthogonal Polarization (CALIOP), this satellite is able to retrieve optical properties of aerosol layers and thin clouds with unprecedented accuracy and sensitivity from space. With a repeat cycle of more than two weeks it does not provide diurnal variations in cirrus cloud properties and cirrus coverage, therefore the most advanced geostationary cloud sensor, the Spinning Enhanced Visible and Infrared Imager (SEVIRI) aboard METEOSAT Second Generation (MSG) is used in this work. SEVIRI covers almost one third of Earth (from 80° N to 80° S and from 80° W to 80° E) with a high temporal resolution of 15 min and a spatial resolution of 3 km x 3 km at subsatellite point.

Within the framework of this thesis a completely new approach was followed to combine the advantages of both instruments (high sensitivity and accuracy of CALIOP with the high temporal resolution and spatial coverage of SEVIRI): The Cirrus Optical properties derived from CALIOP and SEVIRI during day and night (COCS) algorithm is based on an artificial neural network, which retrieves cirrus ice optical thickness (IOT) and top altitude (TOP) from the thermal infrared channels of SEVIRI making day and night observations possible. It is trained by coincident CALIPSO cirrus ice optical thickness and top altitude. This work describes the development of COCS and compares the results of the algorithm with two different lidar measurements, CALIOP and an airborne High Spectral Resolution Lidar (HSRL).

The validation with CALIOP and the HSRL proves the accuracy of the retrieved cirrus ice optical thickness and top altitude. Beside this validation the results of the COCS algorithm are further compared with the METEOSAT Cirrus Detection Algorithm 2 (MeCiDA-2), using the thermal infrared channels of SEVIRI to detect cirrus clouds, and the Algorithm for the Physical Investigation of Clouds with SEVIRI (APICS), using a combination of visible and infrared channels to derive optical properties of clouds.

The validation shows excellent results for the detection of thin cirrus clouds with false alarm rates lower than 5 % and detection efficiencies up to 99 % at a cirrus ice optical thickness greater or equal than 0.1. Low standard deviations of $\sigma_\tau = 0.25$ for cirrus ice optical thickness and $\sigma_z = 756$ m for cirrus top altitude are reached.

Based on five years of processed COCS data, diurnal cycles of cirrus clouds in different regions of the Earth are analysed and discussed. The results show distinct features in coverage and ice optical thickness, which slightly disagree with the forecasts of the European Center for Medium-range Weather Forecasts (ECMWF). While the ECMWF high cloud coverage shows a diurnal cycle comparable to COCS in convective regions, the diurnal cycle in non-convective regions over the North and South Atlantic disagrees. Furthermore the COCS derives higher cirrus cloud coverage compared to the high cloud coverage of the ECMWF of 3 – 10 % for the analysed regions. Finally differences in the North and South Atlantic region, NAR and SAR, are discussed, since the NAR is chosen to cover an area with one of the most frequented air corridors, where hot exhausts of aeroplanes mix with cold air leading to contrail formation. These contrails loose their linear shape with time and then fail to be discriminated from natural formed cirrus clouds. A strong correlation between air traffic density (ATD) and the diurnal cycle of cirrus coverage and ice optical thickness was found over the North Atlantic. Furthermore the differences in cirrus coverage between NAR and SAR follow the diurnal cycle of ATD, with an amplitude of up to 3 %.

Contents

1	Preface	1
2	Remote sensing of cirrus clouds	5
2.1	Cirrus clouds	5
2.2	Passive remote sensing	7
2.2.1	Radiative quantities	7
2.2.2	SEVIRI - Meteosat Second Generation	20
2.2.3	Derivation of cirrus cloud properties from passive remote sensing . .	24
2.3	Active remote sensing	27
2.3.1	Lidar principle	27
2.3.2	CALIOP - CALIPSO	28
2.4	Neural Networks	36
2.4.1	Biological Archetype	36
2.4.2	History of Artificial Neural Networks	37
2.4.3	General setup of Artificial Neural Networks	37
2.4.4	Backpropagation Neural Network	38
3	COCS - Cirrus optical properties derived from CALIOP and SEVIRI during day and night	43
3.1	Training dataset	43
3.1.1	CALIOP data	44
3.1.2	SEVIRI data	46
3.1.3	Auxiliary data	49
3.2	Collocation and Parallax-Correction	50
3.3	Training the neural network	51
3.4	COCS examples	51
3.5	Physical background	56
4	Validation and Comparison	61
4.1	Validation with Lidar measurements	61
4.1.1	Spaceborne lidar data	61

4.1.2	Airborne High Spectral Resolution Lidar data	65
4.1.2.1	PAZI Campaign	65
4.1.2.2	High Spectral Resolution Lidar	66
4.1.2.3	Validation with HSRL	66
4.2	Validation with passive remote sensing	69
4.2.1	Comparison with MeCiDA-2	69
4.2.2	Comparison with APICS	73
4.3	Systematic and statistical uncertainty	77
5	Cirrus diurnal cycles	81
5.1	Cirrus cloud coverage	81
5.1.1	Total Cirrus Coverage	84
5.1.2	Seasonal cirrus coverage	85
5.1.2.1	Seasonal cirrus coverage in MED	87
5.1.2.2	Seasonal cirrus coverage in SAC	90
5.1.2.3	Seasonal cirrus coverage in SAR2	93
5.1.2.4	Seasonal cirrus coverage in SAR1	96
5.1.2.5	Seasonal cirrus coverage in NAR	99
5.2	Cirrus Optical thickness	102
5.2.1	Convective regions	102
5.2.2	Non-convective regions	102
5.3	Intercomparison with ECMWF	105
5.4	Differences between North and South Atlantic Region	108
6	Discussion	113
6.1	Method	113
6.2	Results	114
6.2.1	Convective regions	114
6.2.2	Non-convective regions	117
7	Conclusions and outlook	121
	Appendix	125
	Bibliography	131

Chapter 1

Preface

“Burning of fossil fuels increases the concentration of CO₂ within the Earth’s atmosphere, increasing the atmospheric greenhouse effect and thus leading to global warming.” Arrhenius [1896] was the first to quantify the contribution of carbon dioxide to the greenhouse effect with this statement. More recently in 2007, the Intergovernmental Panel on Climate Change (IPCC) declared in its “Fourth Assessment Report”, [IPCC, 2007], that changes in the atmospheric abundance of greenhouse gases and aerosols, in solar radiation, and in land surface properties alter the energy balance of the climate system. In order to compare how a range of anthropogenic and natural factors drives warming or cooling of global climate the Radiative Forcing (RF) metric was established. Each agent causes a different RF. Especially long-living greenhouse gases lead to a positive RF (warming), while other mechanisms, such as the direct aerosol effect, result in negative RF (cooling). Furthermore, total aerosol radiative forcing can be split in the direct effect and the indirect, so-called “cloud albedo” effect. Especially this indirect effect is listed with low scientific understanding.

Not only these aerosol effects are still found to have a low scientific understanding, but also the understanding of feedback mechanisms of clouds on the radiation budget of the Earth’s atmosphere remains highly uncertain, which makes clouds to the biggest uncertainty factor in climate models and their predictions [Forster et al., 2007, IPCC, 2007]. High ice clouds hold an exceptional position within the large variety of clouds since they generate net forcing and therefore contribute to warming of the Earth’s atmosphere. Anthropogenic cirrus clouds are produced by air traffic when the hot exhausts of aeroplanes mix with cold air leading to contrail formation. These contrails lose their linear shape with time and then fail to be discriminated from natural cirrus clouds. The influence of cirrus clouds in general on the Earth’s radiation budget is mainly dominated by their optical properties (i.e. coverage and optical thickness) as well as by sun zenith angle and surface albedo [Meerkötter et al., 1999]. Concerning heating rates or radiative forcing the optical thickness of cirrus clouds is the key factor [Ackerman et al., 1988].

Since 1983 the infrared and visible radiances of imaging radiometers carried on the international constellation of geostationary weather satellites have been collected in the International Satellite Cloud Climatology Project (ISCCP) [Rossow and Schiffer, 1999]. This project was started to provide the climate modelling community with a definitive cloud climatology. The ISCCP data set of cloud amounts and other products is an archive of global observations covering almost 30 years with a nominal spatial resolution of up to 30 km and a temporal resolution of three hours. [Rossow and Schiffer, 1999] analysed the dataset of the ISCCP and found for cirrus clouds a global amount of roughly 20 % for the period from July 1983 to June 1994, which is split up into different domains. In the tropics a cirrus coverage of up to 21.1 % is retrieved, while the Northern and Southern mid-latitudes are covered by 20.7 % and 16.8 %. But they also mentioned, that the accuracy of the ISCCP cloud amount is determined by three factors: The accuracy and the sensitivity of the cloud detection, and the accuracy of the areal cover fraction estimated by counting cloudy pixels with a finite resolution. The first two factors depend on detection thresholds, which vary with scene type in the ISCCP analysis. Especially the upper-level cloudiness is underestimated, which is caused by missed detections of very thin cirrus clouds [Wielicki and Parker, 1992], which is valid for every detection algorithm utilizing passive remote sensors. Higher amounts of cirrus coverage were found by other polar-orbiting satellites. For example, the multispectral High Resolution Infrared Radiation Sounder (HIRS) aboard the NOAA polar-orbiting satellites, detects up to 34 % as an averaged global cirrus coverage, Wylie and Menzel [1998]. The tropics are covered with cirrus clouds by more than 90 %, high clouds are less dominant in higher latitudes with values of less than 40 % . In [Stubenrauch et al., 2006], eight year of cloud properties retrieved from Television Infrared Observation Satellite-N (TIROS-N) Observational Vertical Sounder (TOVS) observations aboard the NOAA polar orbiting satellites are presented. In case of cirrus clouds, a global averaged cirrus coverage of 27.3 %, again with regional variations. In the Northern midlatitudes an averaged cirrus coverage of 24.7 % are found, while a lower coverage of 21.8 % is present in the Southern mid-latitudes. These completely different numbers are mainly caused by the different detection sensitivities of the different sensors.

Coverage and optical properties of high ice clouds can also be derived by measurements of passive geostationary satellites, for example METEOSAT Second Generation (MSG) carrying the Spinning Enhanced Visible and Infrared Imager (SEVIRI). SEVIRI covers about one third of the Earth area from 80° N to 80° S and from 80° W to 80° E with a sampling distance of 3 km x 3 km at the subsatellite point repeating its measurements every 15 minutes. In order to detect cirrus clouds the Meteosat Cirrus Detection Algorithm 2 (MeCiDA-2) uses the thermal infrared channels of the SEVIRI instrument combining morphological and multi-spectral threshold tests [Krebs et al., 2007, Ewald et al., 2012]. Krebs et al. [2007] showed an average cirrus coverage of 29.3 % for a northern hemispheric

region in the year 2004. Nevertheless, this algorithm is found to have low detection sensitivity to cirrus clouds with low optical thickness ($\tau \leq 0.5$) and therefore underestimates cirrus coverage [Ostler, 2011].

In order to characterize the properties of the detected cirrus clouds, MeCiDA-2 is combined with a well-known method to retrieve the optical thickness of a cloud with passive remote sensing, developed by [Nakajima and King, 1990], which uses the properties of reflected sunlight and near infrared radiation in the Algorithm for the Physical Investigation of Clouds with SEVIRI (APICS) [Bugliaro et al., 2011]. For this reason APICS cannot retrieve optical properties during night time. An overview of the different approaches on the detection of cirrus clouds and the retrieval of their properties by passive remote sensing is given in Section 2.2.3.

Nowadays active spaceborne remote sensing, like radio detection and ranging (radar) and light detection and ranging (lidar), provides the capability to obtain vertical profiles of the Earth's atmosphere with high vertical resolution, the global determination of cloud top height, cloud bottom height, multilayer cloud structure, and planetary boundary layer height in combination with different optical properties of aerosols and clouds [Palm, 2005]. While radar is able to penetrate thick clouds and precipitation, the lidar technology is able to detect and measure thin aerosol and cloud layers down to an optical depth of $\tau \sim 0.01$. Until now spaceborne active remote sensing in atmospheric science has not yet become operational providing only low spatial coverage with repeat cycles of more than two weeks.

In April 2006 the Cloud-Aerosol Lidar and Infrared Pathfinder Satellite Observations (CALIPSO) mission was launched carrying the Cloud-Aerosol Lidar with Orthogonal Polarization (CALIOP) [Winker et al., 2002]. Based on different scene classifications and retrieval algorithms in combination with auxiliary datasets, CALIOP provides highly accurate measurements of different optical and physical properties of e.g. cirrus clouds from a polar orbit with a footprint of about 100 m along and 90 m cross track and a vertical resolution of up to 30 m [Vaughan et al., 2004]. Different approaches on the validation of CALIOP measurements showed its high accuracy (Section 2.3.2). But due to this high spatial and vertical resolution together with a repeat cycle of 16 days, the CALIOP instrument is unable to retrieve information on life cycles and diurnal cycles of atmospheric features such as cirrus clouds.

The work described in this thesis focusses on the diurnal cycle of cirrus clouds. As mentioned, it is crucial for e.g. radiative transfer calculations and climate models to have accurate and detailed knowledge of the diurnal cycle of cirrus coverage as well as information on their optical properties in order to calculate their radiative effect and their climate impact, since cirrus clouds can have both, a cooling effect during daytime and a warming effect at night. Therefore a new approach on a synergistic use of geostationary passive and polar-orbiting active remote sensing is presented in this work, which aims to

combine the advantages of both. While SEVIRI offers a good spatial and high temporal resolution, CALIOP is known to retrieve e.g. cirrus ice optical thickness and top altitude with high accuracy, high sensitivity, and high vertical resolution. The aim of this new algorithm based on a backpropagation neural network (Section 2.4) is on the one hand to retrieve cirrus optical thickness and cirrus top altitude by using the brightness temperatures of the thermal infrared channels of SEVIRI aboard MSG (Section 2.2) in order to provide a daytime and nighttime detection of cirrus clouds. On the other hand, this new algorithm is aimed to have higher sensitivity to especially thin cirrus clouds, which are underestimated by passive remote sensing until now. The neural network used in this work was coded in the Interactive Data Language (IDL) by H. Mannstein and was earlier used for tasks like the determination of reflected short-wave radiation from SEVIRI based on model calculations [Vazquez-Navarro et al., 2012]. For the training of the neural network three years of cirrus ice optical thickness and top altitude derived from CALIOP aboard CALIPSO (Section 2.3) are collocated with the infrared brightness temperature measurements of SEVIRI. Therefore the primary setup and especially the hidden layer of the neural network had to be extended. This new algorithm, the Cirrus Optical properties derived from CALIOP and SEVIRI during day and night time (COCS) algorithm (Section 3), is now able to detect even thin cirrus clouds with ice optical thickness down to $\tau \geq 0.1$. Beside high detection efficiencies, it is also important to derive accurate values of cirrus optical properties and top altitudes, which is proven by comparisons and validations with CALIOP itself, an airborne HSRL during the “PAZI” project in 2008, the MeCiDA-2, and the APICS algorithm (Chapter 4).

Within the framework of this thesis, five years of data were processed (2006 - 2010) for the analysis of the diurnal cirrus cycle in five different regions (Chapter 5). Two regions are dominated by convective cloud formation, and two regions are located over the South Atlantic, where only little or no influence of convection is present. Additionally a region over the North Atlantic was analysed in order to provide indications of the possible influence of air traffic on cirrus cloud coverage and microphysical properties as found in [Graf et al., 2009]. This North Atlantic region covers an area with one of the most frequented oceanic air corridors, the North Atlantic flight corridor. Additionally, a comparison of one year of high cloud coverage derived from the Integrated Forecast System (IFS) of the European Centre for Medium-range Weather Forecasts (ECMWF) and the cirrus coverage derived by COCS is presented, where differences are found in most of the analysed regions. The highest discrepancies are detected in the North Atlantic region. Thus the diurnal changes in cirrus coverage and ice optical thickness of two different regions, one influenced by the North Atlantic flight corridor and one “air traffic free” region over the South Atlantic, are compared to the air traffic density over the North Atlantic and the disparities are analysed and discussed, Section 5.4.

Chapter 2

Remote sensing of cirrus clouds

This chapter provides a brief overview of cirrus clouds and their formation processes (Section 2.1) followed by an introduction of radiative transfer (Section 2.2.1) and its utilization for spaceborne remote sensing on Meteosat Second Generation (MSG) (Section 2.2.2). Secondly, the light detection and ranging (lidar) principle is introduced focussing on the Cloud-Aerosol Lidar with Orthogonal Polarisation (CALIOP) instrument aboard the Cloud-Aerosol Lidar and Infrared Pathfinder Satellite Observations (CALIPSO) mission and its different algorithms for the retrieval of cirrus optical properties. Finally the theory of artificial neural networks and especially backpropagation neural networks is explained.

2.1 Cirrus clouds

Historically the family of cirrus clouds has been defined on the basis of visual observations by trained observers [Lynch et al., 2002]. They appear at great altitudes in the upper troposphere and can visually be identified by their texture, color, and associated phenomena such as parhelia and halos. Cirrus clouds solely consist of ice particles and are often optically thin. The ice particles show various nonspherical shapes (see Hallett et al. [2002], Heymsfield and McFarquhar [2002], Dowling and Radke [1990]). The basic microphysical conditions, in addition to their dissimilar temperatures and altitudes in the troposphere, have fundamental implications in terms of radiative transfer [Liou, 2002]. According to the World Meteorological Organisation (WMO)[WMO and World Meteorological Organisation, 1987, 1995] cirrus clouds are defined as:

“**Cirrus:** Detached clouds in the form of white, delicate filaments or white or mostly white patches or narrow bands. These clouds have a fibrous (hair-like) appearance, or a silky sheen, or both.”

“**Cirrocumulus:** Thin, white patch, sheet or layer of cloud without shading, composed of very small elements in the form of rains, ripples etc., merged or separate, and more

Category	Mechanism
Synoptic (jet stream, frontal, etc.)	Top-down generation
Injection cirrus	Thunderstorm anvil-derived
Mountain-wave updraft	Orographic, terrain-induced
Cold trap	Tropopause-topped thin layer
Contrail cirrus	Rapid cooling of aircraft exhausts

Table 2.1: Breakdown of cirrus clouds by generating mechanisms, adapted from Sassen and Mace [2002].

or less regularly arranged; most of the elements have an apparent width of less than one degree.”

“**Cirrostratus:** Transparent, whitish cloud veil of fibrous (hair-like) or smooth appearance, totally or partly covering the sky, and generally halo phenomena.”

These definitions are split in different species and varieties [Lynch et al., 2002], but are entirely based on visual observation. For example, a well recognized cirrus clouds class, the so-called subvisible cirrus, is missing as well as contrails and contrail cirrus formed by aviation. Later lidar studies [Sassen and Cho, 1992] estimated a typical optical depth of $\tau < 0.03$ for subvisible cirrus, $0.03 < \tau < 0.3$ for thin (i.e. bluish coloured), and $0.3 < \tau < 3.0$ (white or grayish) for opaque colours.

Table 2.1 summarizes the generating mechanisms responsible for cirrus cloud formation, according to Sassen and Mace [2002]. These mechanisms demonstrate the connections between cirrus cloud generation and weather processes [Wylie, 2002]. A common feature over mid-latitude land and ocean are synoptic cirrus like cirrus clouds formed in connection with jet streams, and frontal and low-pressure systems. These clouds tend to form from cloud top ice nucleating zones where ice supersaturations are relatively high from the homogeneous nucleating of haze particles [De Mott, 2002, Khvorostyanov and Sassen, 2002]. The temperature for this homogeneous nucleation was found to be around 236 K [Wood et al., 2002].

Cumulonimbus clouds generally cover regions over land and ocean. Most frequently they occur in the Intertropical Convergence Zone (ITCZ) and other tropical regions. Deep convection generates large amounts of spreading anvils associated with long-lived cirrus. According to Mace et al. [2006] other cirrus formation mechanisms play an additional role in the tropics. Over land long persisting mountain-wave cirrus are formed orographically in local updrafts downwind of the responsible terrain [Wylie, 2002]. Only recently recognized, the so-called cold trap cirrus occur primarily in the tropics at very high altitudes and the coldest encountered tropospheric temperatures. The moisture supply of these optically very thin cirrus clouds seems related to thunderstorm activity, although their

extended lifetimes suggest long-lived maintenance processes involving radiative or tropical wave processes [Sassen et al., 2008].

Finally, an anthropogenic class of cirrus clouds has to be recognized. Exhausts of aeroplanes can induce contrails, if the surrounding air is cold and humid. The Schmidt-Applemann criteria quantifies such atmospheric conditions. If the surrounding atmosphere is ice supersaturated, ice crystals grow by absorbing the surrounding humidity, while contrails expand by turbulent mixing and wind shear, [Schmidt, 1941, Appleman, 1953, Schumann, 2002]. With growing lifetime these contrails loose their shape and form contrail cirrus clouds [Schumann, 2005].

2.2 Passive remote sensing

Passive remote sensing is based on the theory of electromagnetic radiation and its transfer through the atmosphere. In order to retrieve information about the actual atmospheric condition from a measured radiative quantity good knowledge of the theory of radiative transfer is necessary. This section introduces the basics of radiative transfer in the atmosphere, which are used in this work, followed by a presentation of the Spinning Enhanced Visible and Infrared Imager (SEVIRI) aboard the geostationary METEOSAT Second Generation (MSG) satellites and its operating principle, which is based on collecting radiation from a target area and focussing it on detectors sensitive to different bands of the electromagnetic spectrum.

2.2.1 Radiative quantities

The propagation of radiance through a medium is quantitatively described by the theory of radiative transfer, which is dominated by the wave-particle duality, since one part of its phenomena is explained by wave mechanics (e.g. Rayleigh and Mie scattering), another part is completely described by quantum mechanics (e.g. absorption, Planckfunction). Electromagnetic waves are characterized by their wavelength λ , $[\frac{1}{m}]$, or their frequency ν , $[s^{-1}]$:

$$\lambda = \frac{c}{\nu}. \quad (2.1)$$

The velocity of light c is measured to be $299,792,458 \frac{m}{s}$ in vacuum. For Earth's atmosphere the ratio of light speed in a medium to its speed in vacuum is given by the refractive index n with $n > 1$, since light is propagating slower in the atmosphere than in space due to interaction with molecules. The wave number $k = \frac{1}{\lambda}$ is also used to describe

electromagnetic waves [m^{-1}] (or not SI conform as [cm^{-1}]).

Radiation is usually quantified by the energy it transports. The amount of energy E transported per unit time is defined as the radiation power Φ :

$$\Phi = \frac{dE}{dt}. \quad (2.2)$$

The flux through an unit area dA with given orientation describes the irradiance F :

$$F = \frac{d\Phi}{dA}. \quad (2.3)$$

The most important quantity in spaceborne remote sensing is the radiance $L = L(\vec{r}, \vec{\Omega}, t)$, which is defined as the radiation energy $d\Phi$ through the area element dA with the surface normal \vec{n} at a location \vec{r} during the time dt through the solid angle element $d\Omega$ along the direction $\vec{\Omega}$ with the unit [$\frac{W}{m^2sr}$]. The angle between the direction $\vec{\Omega}$ and the surface normal \vec{n} is denoted as Θ (Fig. 2.1):

$$L = \frac{d^2\Phi}{d\Omega dA \cos\Theta}, \quad (2.4)$$

with $\cos\Theta = \vec{n}\vec{\Omega}$ multiplied by dA is the projection of the surface element onto the plane normal to $\vec{\Omega}$. The infinitesimal element $d\Omega$ is expressed in Steradian, [sr], and is calculated in polar coordinates (Fig. 2.2):

$$d\Omega = \sin\Theta d\Theta d\phi. \quad (2.5)$$

By combining Eq. 2.3 and 2.4, the irradiance over a hemisphere is related to the radiance by:

$$F = \int_0^{2\pi} \int_0^{\pi/2} L \cos\Theta \sin\Theta d\Theta d\phi. \quad (2.6)$$

In case of isotropic radiation, i.e. $L(\vec{r}, \vec{\Omega}, t) = L(\vec{r}, t)$, the integration of Eq. 2.6 over the upper hemisphere leads to:

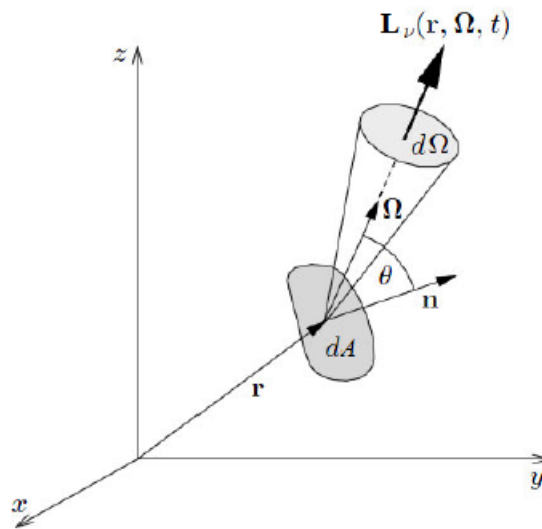


Figure 2.1: Radiant energy transmitted through the infinitesimal area element dA with the surface normal \vec{n} located at \vec{r} into the solid angle element $d\Omega$ along the direction $\vec{\Omega}$ of the photons, adapted from [Zdunkowski et al., 2007].

$$F = \pi L. \quad (2.7)$$

The solid angle of a unity sphere has a value of 4π sr, the half of the unity sphere is therefore calculated as 2π sr. For the radiance L at a specific wavelength λ (frequency ν , or wave number k), L_λ (or L_ν or L_k) is called the spectral or monochromatic radiance and is computed as:

$$L_\lambda = \frac{dL}{d\lambda}. \quad (2.8)$$

Thermal emission

Any matter emits electromagnetic radiation depending on its temperature. An idealized physical body that absorbs all incoming electromagnetic radiation is called “blackbody”. A blackbody at a constant temperature emits electromagnetic radiation at all wavelengths and into all directions. The amount of electromagnetic radiation emitted by a blackbody has a spectrum that is determined by the temperature alone according to Planck’s law, [Planck, 1901]. The spectral radiance $B_\lambda(T)$ is called Planck function relates the spectral radiance to the temperature T of the emitting body:

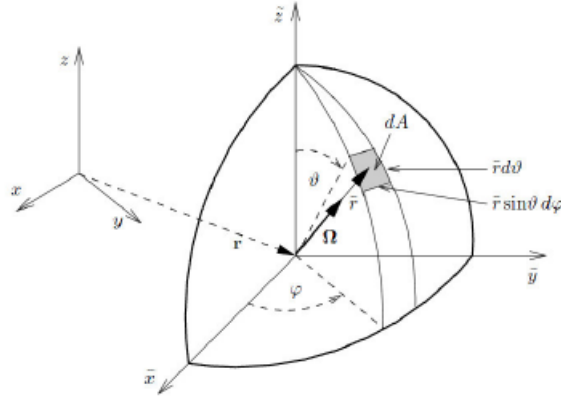


Figure 2.2: Definition of the local, spheric $(\tilde{r}, \varphi, \vartheta)$ coordinate system and the direction Ω [Zdunkowski et al., 2007].

$$B_{\lambda}(T) = \frac{2hc^2}{\lambda^5} \frac{1}{\left(\exp\left(\frac{hc}{k_B\lambda T}\right) - 1\right)}, \quad (2.9)$$

with the Boltzmann constant $k_B = 1.381 \cdot 10^{-23} \text{ JK}^{-1}$ and the Planck constant $h = 6.62606957 \cdot 10^{-34} \text{ Js}$.

An important quantity concerning the measurements of spaceborne radiometers is the brightness temperature T_b , which is the temperature a blackbody should have to produce the measured spectral radiance L_m at a wavelength λ . Therefore the inversion of the Planck function gives the monochromatic brightness temperature T_b :

$$T_b = \frac{2hc}{k_b\lambda} \left(\ln\left(\frac{2hc}{\lambda^5 L_m}\right) + 1 \right). \quad (2.10)$$

In general, this fundamental equation allows to translate the radiances measured by spaceborne radiometers into brightness temperatures, but the spectral band of wavelengths of each channel has to be concerned (Eq. 2.46).

By assuming that the Sun is blackbody with a temperature $T = 5700 \text{ K}$ and taking into account the distance from the Sun, the solar spectrum can be calculated. The irradiance F_S is emitted by the Sun at distance R to the Earth through an area of $A = 4R^2\pi$. Therefore, the values of the Planck function are multiplied with the ratio $\frac{R_S^2}{R^2}$, where R_S is the radius of the Sun.

By integrating the Planck function (Eq. 2.9) over all wavelengths the integrated blackbody irradiance can be derived:

$$B(T) = \int_0^{\infty} B_{\lambda}(T) d\lambda = \int_0^{\infty} \frac{2hc^2 \lambda^{-5}}{\exp\left(\frac{hc}{k_B \lambda T}\right) - 1} d\lambda. \quad (2.11)$$

With $x = \frac{hc}{k_B \lambda T}$, Eq. 2.11 can be written as:

$$B(T) = \frac{2k_B^4 T^4}{h^3 c^2} \int_0^{\infty} \frac{x^3}{(\exp(x) - 1)} dx. \quad (2.12)$$

The integral term in Eq. 2.12 is equal to $\frac{\pi}{15}$. Therefore, defining $b = \frac{\sigma}{2\pi}$, the result is:

$$B(T) = bT^4. \quad (2.13)$$

The irradiance F emitted by a blackbody (Eq 2.7), since $B_{\lambda}(T)$ is isotropic, can be written as:

$$F = \pi B_{\lambda}(T) = \sigma T^4. \quad (2.14)$$

This equation is known as the ‘‘Stefan-Boltzmann-Law’’ with the Stefan-Boltzmann constant $\sigma = \pi b \cong 5.678 \cdot 10^{-8} \frac{\text{W}}{\text{m}^2 \text{K}^4}$ [Stefan, 1879, Boltzmann, 1884]. The emission capability of a real body compared to the idealized blackbody with similar temperature can be quantified by the emissivity ϵ_{λ} :

$$\epsilon_{\lambda} = \frac{L_{\lambda}}{B_{\lambda}(T)}, \quad (2.15)$$

with the real emitted spectral radiance L_{λ} at a wavelength λ and the idealized blackbody radiance $B_{\lambda}(T)$ calculated with the Planck function.

The relationship between absorptivity a_{λ} and emissivity ϵ_{λ} can be expressed according to Kirchhoff’s law:

$$\epsilon_{\lambda} = a_{\lambda}. \quad (2.16)$$

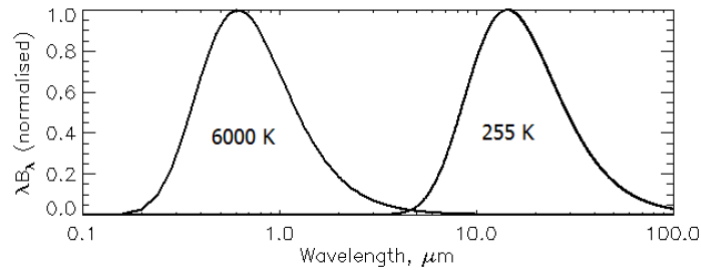


Figure 2.3: Solar ($T = 6000$ K) and terrestrial ($T = 255$ K) normalized spectra [Tjemkes and Schmetz, 1998].

Kirchhoff's law is only valid for systems in a local thermodynamical equilibrium. This thermodynamical balance is found in Earth's atmosphere up to an altitude of 100 km, where air molecules exchange their energy very fast by hitting each other, and therefore generate a specific temperature. According to Kidder and von der Haar [1995], this thermodynamical balance of the atmosphere can be assumed for most applications in spaceborne meteorology.

Wien displacement law

In order to obtain the wavelength of the maximum emission of a blackbody at a temperature T , the Planck function (Eq. 2.9) is differentiated with respect to wavelength. By setting the result equal zero the Wien displacement law is obtained:

$$\lambda T = 2897 \mu\text{m K}. \quad (2.17)$$

This equation enables the determination of the temperature of a radiation source from its emission spectrum.

Based on Planck's law two different spectra are depicted in Fig. 2.3. On the left, the spectrum with a temperature close to the temperature of the Sun is shown ($T = 6000$ K), while on the right the emission spectrum of a body with a temperature of 255 K representing the effective temperature of the Earth is depicted. This second spectrum is also known as the terrestrial spectrum. Solar and terrestrial spectrum can be separated because of their virtual absence of overlap. Solar emission of radiation is mainly produced in the visible and near-infrared parts of the spectrum, while terrestrial emission is limited to the infrared wavelengths. The maximum emission takes place at around $0.5\mu\text{m}$ and around $11.0\mu\text{m}$.

The most important sources of electromagnetic radiation in Earth's atmosphere are the Sun and the Earth itself. In Fig. 2.4 the solar spectrum is calculated with a radiative

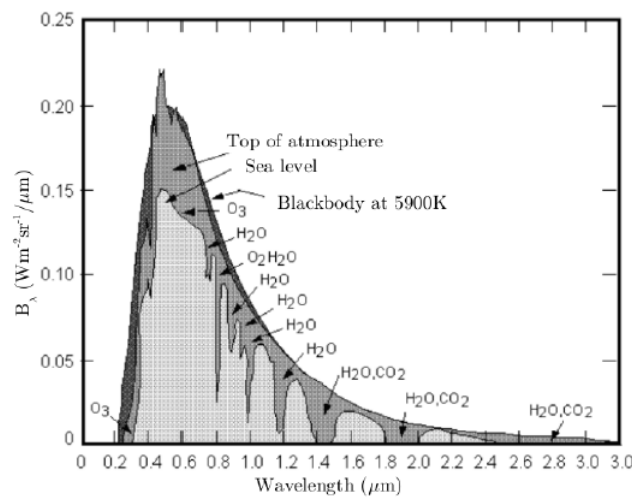


Figure 2.4: Solar spectrum at TOA and at sea level and comparison to the black body spectrum calculated with the Planck function $B_\lambda(T)$ for $T = 5900$ K [Wallace and Hobbs, 1977].

transfer model at Earth’s surface (sea level) after passing through the atmosphere and at the top of atmosphere (TOA) representing the solar spectrum before absorption in the atmosphere takes place. Both curves are compared to the idealized emission spectrum of a blackbody with the temperature of the Sun $T = 5900$ K, calculated with the Planck function (Eq. 2.9). The structure of both calculated spectra is caused by atmospheric absorption as well as absorption lines in the solar spectrum, the so called “Fraunhofer lines”, and differs from the idealized blackbody. Radiation is absorbed by air molecules and particles and is transformed into heat or chemical energy on the one hand. On the other hand radiation is scattered into/away from its direction of propagation.

Atmospheric absorption

Absorption is the process by which incoming radiant energy is retained by i.e. the atmosphere. When Earth’s atmosphere absorbs energy, the result is an irreversible transformation of radiation into another form of energy. For this work especially the absorption coefficient α_a is important. The absorption cross-section σ_a is the effective area which governs the probability of absorption taking place. It is calculated by the absorption efficiency of the particle Q_a is calculated with the absorption cross-section and the area cross-section A :

$$Q_a = \frac{\sigma_a}{A}. \quad (2.18)$$

Thus, the absorption coefficient α_a describes a medium containing particle with absorption cross-section σ_a at a concentration described as volume density ρ_a :

$$\alpha_a = \rho_a \sigma_a. \quad (2.19)$$

Scattering

As explained above, the intensity of radiation travelling through a medium is weakened by its interaction with matter. Beside absorption scattering is the second main contributor to the change of radiation in Earth's atmosphere. Its direction is changed to the direction of propagation after being scattered by air molecules and particles. Since scattering depends on the ratio of particle radius r and wavelength λ , it is necessary to choose the right scattering mechanism due to both properties. The size of particles in the atmosphere varies from $\sim 10^{-4} \mu\text{m}$ for gas molecules to $\sim 10 - 10^2 \mu\text{m}$ for ice crystals up to rain drops and hail up with sizes of $\sim \text{cm}$. Thus, the scale parameter x is defined as:

$$x \equiv \frac{2\pi r}{\lambda}, \quad (2.20)$$

with r is the radius of a spheric particle. In case of non-spheric particles, r can be estimated from the radius of spheric particles with similar volume or surface.

For the description of the angular distribution of the scattered radiation (e.g. in Earth's atmosphere) the phase function \check{P} is essential, [Liou, 2002]:

$$\frac{1}{4\pi} \int_{4\pi} \check{P}(\vec{\Omega}', \vec{\Omega}) d\Omega = 1. \quad (2.21)$$

This function \check{P} is a measure for the scattering probability of electromagnetic radiation with the incident direction $\vec{\Omega}'$ being scattered into the direction $\vec{\Omega}$ [Zdunkowski et al., 2007] and is normalised according to Eq. 2.20.

The scattering at spheric or randomly orientated, non-spheric particles (such as ice crystals) can be expressed as a function of the scattering angle alone:

$$\check{P}(\Omega', \Omega) = \check{P}(\Theta). \quad (2.22)$$

The scattering angle Θ is the angle between incoming and scattered radiation.

Rayleigh scattering

For scale parameters $x \ll 1$ the theory of Rayleigh scattering is used [Rayleigh, 1871]. In this case, the size of the particle is very small compared to the wavelength of the incoming radiation.

Thus, the electric field \vec{E}_0 of the incoming radiation induces a dipole moment $\vec{p}_0 = \chi \vec{E}_0$ to a particle, where χ is the polarization of the particle. In turn this dipole emits polarized electromagnetic waves, the scattered radiation.

The phase function \check{P} for the Rayleigh scattering is then computed as:

$$\check{P}(\cos\Theta) = \frac{3}{4}(1 + \cos^2\Theta). \quad (2.23)$$

According to Liou [2002] the scattered radiance $L(\Theta)$ depending on the incoming radiance L_0 can be written as:

$$L(\Theta) = \frac{L_0}{R^2} \chi^2 \frac{128\pi^5}{3\lambda^4} \frac{\check{P}(\Theta)}{4\pi}. \quad (2.24)$$

Thus, the scattered intensity is direct proportional to the phase function and λ^{-4} .

Mie scattering

For scale parameters $x \geq 1$ scattering can be described according to the Mie theory. The Mie theory describes the scattering of light at homogeneous, spheric particles and is based on the Maxwell equations. This section will just point out the essentials of the theory, more details can be found in Liou [2002] and Zdunkowski et al. [2007].

According to the Mie theory, the scattered radiance $L(\theta)$ is given by:

$$L(\Theta) = L_0 \left(\frac{\sigma_S}{R^2} \right) \frac{\check{P}(\Theta)}{4\pi}, \quad (2.25)$$

where L_0 is the incoming radiance. The scattering cross section σ_S , which describes the likelihood of radiation being scattered by a particle, can be expressed by the following series expansion:

$$\frac{\sigma_S}{\pi r^2} = Q_S = c_1 x^4 (1 + c_2 x^2 + c_3 x^4 + \dots). \quad (2.26)$$

This relation of the scattering cross section to the surface of the particle is also defined as the scattering efficiency Q_S .

In case of non-absorbing particles, the first two coefficients are defined as:

$$c_1 = \frac{8}{3} \left(\frac{m^2 - 1}{m^2 + 2} \right)^2, \quad (2.27)$$

$$c_2 = \frac{6}{5} \left(\frac{m^2 - 1}{m^2 + 2} \right)^2, \quad (2.28)$$

with the refractive index m of the particle, which is the number that describes how light, or any other radiation, propagates through that particle or medium. For scattering processes with a scale parameter $x \ll 1$ all terms are negligible apart from the first term, which represents the contribution of the dipole. Therefore, Rayleigh scattering is found to be a special case of the Mie theory.

Similar to the absorption coefficient α_a , the scattering coefficient α_s is calculated as:

$$\alpha_s = \rho_s \sigma_s. \quad (2.29)$$

Atmospheric extinction

In order to quantify the degree of attenuation of radiation the extinction coefficient α is used. It is defined as the sum of absorption α_a and scattering coefficient α_s :

$$\alpha = \alpha_a + \alpha_s, \quad (2.30)$$

with units of $\frac{1}{m}$.

Another important parameter in the theory of radiative transfer is the single scattering albedo, which describes the ratio of scattering to absorption in a medium:

$$\omega_0 = \frac{\alpha_s}{\alpha}. \quad (2.31)$$

The attenuation of electromagnetic radiation through a medium with the extinction coefficient α after a path length $\Delta s = s_2 - s_1$ is calculated by the Lambert-Beer law:

$$L_\lambda(s_2) = L_\lambda(s_1)e^{\left[-\int_{s_1}^{s_2} \alpha(s)ds\right]}, \quad (2.32)$$

where the term in the exponent is denoted as the optical thickness τ :

$$\tau(s_1, s_2) = \int_{s_1}^{s_2} \alpha(s)ds. \quad (2.33)$$

The transmission t_s along this path is defined as:

$$t_s(s_1, s_2) = e^{-\tau(s_1, s_2)}, \quad (2.34)$$

with values between 0 (for $\tau \rightarrow \infty$) and 1 (for $\tau = 0$).

Since many parameters of the Earth's atmosphere, like air pressure, density, temperature, and its chemical composition show a larger vertical variability than a horizontal variability, it is often assumed that:

$$\alpha(x, y, z) \approx \alpha(z). \quad (2.35)$$

With this so-called plane parallel approximation, the optical thickness of an atmospheric layer just depends on the zenith angle θ of the incoming radiation and the vertical distance z . The path length s of radiation travelling through the atmosphere can be calculated as (Fig. 2.5):

$$s = \frac{z}{\mu}, \text{ with } \mu = \cos\theta. \quad (2.36)$$

Thus the optical thickness τ of the atmospheric layer between z_1 and z_2 , where $z_2 < z_1$ can be calculated as:

$$\tau(z_1, z_2) = \int_{z_1}^{z_2} \alpha(z)dz = \tau(z_2) - \tau(z_1), \quad (2.37)$$

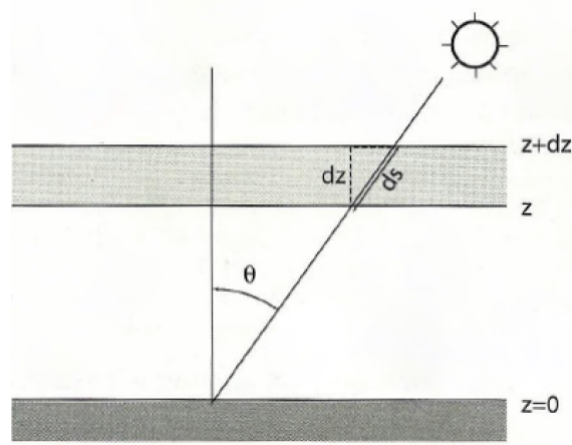


Figure 2.5: Relationship between slant path and vertical path of a plan parallel atmosphere [Petty, 2006].

and the transmission t_s for the layer

$$t_s(z_1, z_2) = e^{-\frac{1}{\mu}\tau(z_1, z_2)} = \frac{t_s(z_1)}{t_s(z_2)}. \quad (2.38)$$

Radiative transfer equation

The transfer of electromagnetic radiation through a defined volume is described by the radiative transfer equation [Chandrasekhar, 1950]. The radiance is reduced by absorption and scattering, while scattering and thermal emission have a positive contribution. In polar coordinates, the radiative transfer equation reads as:

$$\frac{1}{\alpha} \frac{dL_\lambda(\theta, \varphi)}{dz} = -\mu L_\lambda(\theta', \varphi') + \mu \frac{\omega_0}{4\pi} \int_0^\pi \int_0^{2\pi} \check{P}_\lambda(\theta', \varphi', \theta, \varphi) L(\theta', \varphi') \sin\theta' d\theta' d\varphi' + \mu(1 - \omega_0) B_\lambda(T). \quad (2.39)$$

The first term on the right hand side describes the attenuation of radiation according to the Lambert-Beer law, while the second term characterises the scattering in the optical path. The third term represents the emission within the optical path. θ', φ' and θ, φ denote the direction of the photons before and after being scattered. $B_\lambda(T(p))$ is the emitted radiance of a black body at the atmospheric temperature T . The emissivity is calculated as $\alpha(1 - \omega_0) = \alpha_a$.

The monochromatic radiance L_λ at a wavelength λ emitted along a vertical path at the

top of the atmosphere and incident at a spaceborne instrument is given as the solution of Eq. 2.39 by neglecting atmospheric scattering:

$$L_\lambda = (L_0)_\lambda t_{s,\lambda}(z_0) + \int_{z_0}^{\infty} B_\lambda(T(z)) W_\lambda(z) dz, \quad (2.40)$$

where L_0 is the emission from the Earth's surface at height z_0 , $t_{s,\lambda}$ is the vertical transmittance at height z to space, $T(z)$ is the vertical temperature profile, and $B_\lambda(T(z))$ is the corresponding Planck function profile. The so called weighting function

$$W_\lambda(z) = \frac{dt_{s,\lambda}(z)}{dz}, \quad (2.41)$$

defines the change of the total transmittance with respect to altitude. It specifies the vertical location of the atmosphere from which the radiation measured by the satellite channel was emitted, and, therefore determines the region of the atmosphere which can be sensed from space at this wavelength. Since it is the derivative of the transmittance, the weighting function has its maximum values in those regions where the absorption of radiation at specific wavelengths is strongest. Of course, it depends on viewing angle and atmospheric composition.

Cloud properties

Clouds consist of water drops and/or ice particles. The particle size of ice crystals and water droplets in a cloud is characterized by the effective radius r_{eff} , which is a fundamental size to describe scattered radiation [Foot, 1988]. For particles with arbitrary shape and known size distribution, the volume effective radius is defined as:

$$r_{eff} = \frac{3 V}{4 A_p}, \quad (2.42)$$

with the mean volume V of the particle ensemble and its mean projected cross-section area A_p . For spherical particles r_{eff} is calculated as:

$$r_{eff} = \frac{\int_0^{\infty} \pi r^3 n(r) dr}{\int_0^{\infty} \pi r^2 n(r) dr}, \quad (2.43)$$

where the number of particles per unit volume with radius between r and $r + dr$ is defined as $n(r)dr$. In combination with the optical thickness τ (Eq. 2.37), the effective radius r_{eff} is essential for an estimate of the ice water content IWC of an ice cloud as parametrized by Key et al. [2002]:

$$\frac{\alpha}{IWC} = \sum_{n=0}^3 a_n \frac{1}{r_{eff}^n}, \quad (2.44)$$

with the fitting coefficient of a non-linear regression a_n . Therefore, the relationship between IWC and τ can be written with $\alpha = \frac{d\tau}{dz}$ as:

$$\tau = \Delta z IWC \sum_{n=0}^3 a_n \frac{1}{r_{eff}^n}. \quad (2.45)$$

2.2.2 SEVIRI - Meteosat Second Generation

The METEOSAT Second Generation (MSG) program consists of four equal satellites (MSG-1, MSG-2, MSG-3, MSG-4), which are developed for meteorological observations of the Earth's atmosphere until at least 2018. Each satellite has an expected lifetime of seven years. The MSG program is established as a cooperation of the European Space Agency (ESA) and the European Organisation for the Exploitation of Meteorological Satellites (EUMETSAT). The satellites are operated in a geostationary orbit at an altitude of around 36.000 km and at geographical longitudes around 0°.

The main instrument aboard MSG, the Spinning Enhanced Visible and Infrared Imager (SEVIRI) covers one third of the Earth's surface with its 12 spectral channels listed in Table 2.2. The satellite itself spins with 100 rpm while SEVIRI measures the Earth's radiation as shown in Fig. 2.6. It combines the East-West scan generated by the satellite spin motion and the South to North micro-step scan of the mirror.

The 11 low resolution (LR) channels cover the whole "disc" from around 80° N to 80° S latitude and 80° W to 80° E longitude every 15 minutes with a sampling distance of 3 km at subsatellite point. This resolution decreases for growing viewing zenith angle due to the curvature of Earth's surface. At each spin of the satellite, SEVIRI's LR channels scan three lines. This procedure lasts approximately 12 minutes, while three additional minutes are required e.g. for resetting the scan mirror to the start position and for data handling. Channel 12 is the so-called High Resolution Visible (HRV) channel, which covers half of the MSG disc in the East-West direction and the complete disc in the North-South direction [Schmetz et al., 2002]. The HRV channel follows the LR scanning

Channel number	Channel name	Central wavelength / μm	Spectral band / μm	Subsatellite point resolution
1	VIS06	0.635	0.56 - 0.71	3 km x 3 km
2	VIS08	0.81	0.74 - 0.88	3 km x 3 km
3	NIR16	1.64	1.50 - 1.78	3 km x 3 km
4	IR039	3.92	3.48 - 4.36	3 km x 3 km
5	WV062	6.25	5.35 - 7.15	3 km x 3 km
6	WV073	7.35	6.85 - 7.85	3 km x 3 km
7	IR087	8.70	8.30 - 9.10	3 km x 3 km
8	IR097	9.66	9.38 - 9.94	3 km x 3 km
9	IR108	10.8	9.80 - 11.80	3 km x 3 km
10	IR120	12.0	11.00 - 13.00	3 km x 3 km
11	IR134	13.4	12.40 - 14.40	3 km x 3 km
12	HRV	-	0.40 - 1.10	1 km x 1 km

Table 2.2: SEVIRI channels [Schmetz et al., 2002].

procedure, but scans nine lines at each satellite spin. The Rapid Scan Service (RSS) from MSG-2 started mid-2008, which provides data every 5 instead of 15 minutes. It covers the northern part of the MSG disc from approximately 15° N to 70° N. To provide accurate measurements, SEVIRI uses the deep space as a cold source and an internal blackbody as a warm source for the calibration of the infrared channels, [Pili, 2000].

In order to make a day and night time observation of atmospheric processes possible SEVIRI is suited with seven channels in the thermal infrared (channels 5 to 11 with wavelengths from around 6 to 14 μm). The interpretation of these observations is easier when using equivalent brightness temperatures. However, Eq. 2.10 cannot be applied directly, because SEVIRI channels extend over a finite spectral interval. To consider this effect, Tjemkes [2005] derived an approximated analytical relationship:

$$T_b = \frac{\frac{\frac{hc}{k_B} \nu_C}{\log\left(\frac{2hc^2\nu^3}{I_{\Delta\lambda}} + 1\right)} - B}{A}, \quad (2.46)$$

with $C_1 = 2hc^2$ and $C_2 = \frac{hc}{k_B}$, where $c = 299,792,458 \frac{\text{m}}{\text{s}}$ is the speed of light, $h = 6.625 \cdot 10^{-34} \text{ Js}$ is the Planck constant, and $k_B = 1.3806503 \cdot 10^{-23} \frac{\text{m}^2\text{kg}}{\text{s}^2\text{K}}$ is the Boltzmann constant. ν_C is the central wave number, A and B are non-linear regression coefficients of the thermal channels of SEVIRI (Table 2.3). The coefficients A and B are chosen with the boundary condition that the minimum square deviation of the equivalent brightness temperature T_b from the exact value between 150 and 350 K is smaller than 0.05 K. The result of a high spectral resolution radiative transfer model (line-by-line) for a “mid-latitude summer” atmosphere is shown in Fig. 2.7 [Tjemkes and Schmetz, 1998]. Radiances are

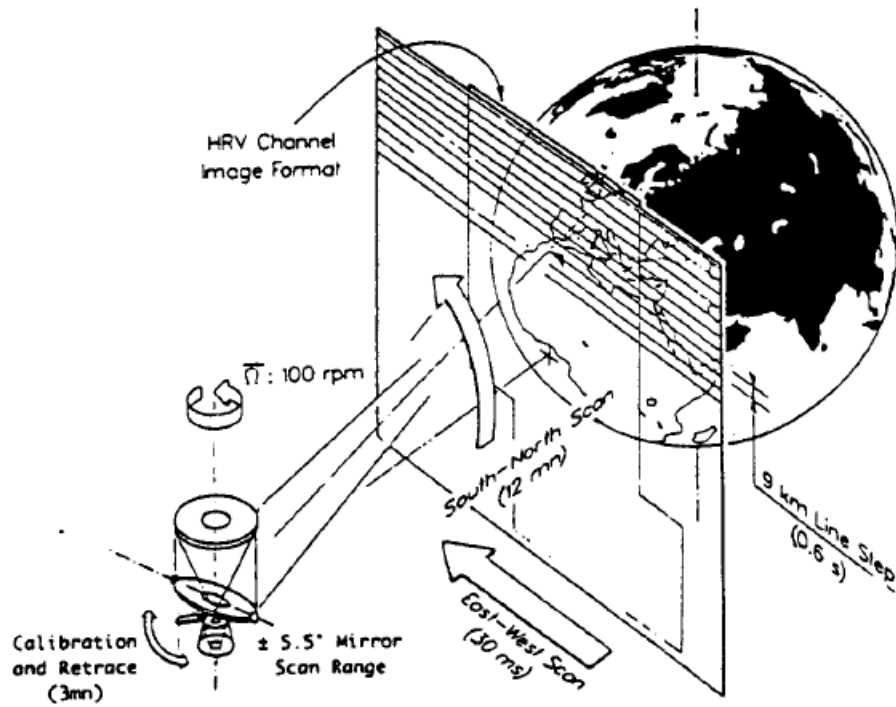


Figure 2.6: Earth imaging principle of SEVIRI [EUMETSAT, 2010].

Channel	ν_C/cm^{-1}	A	B
WV062	1598.566	0.9963	2.219
WV073	1362.142	0.9991	0.485
IR087	1149.083	0.9996	0.181
IR097	1034.345	0.9999	0.060
IR108	930.659	0.9983	0.627
IR120	839.661	0.9988	0.397
IR134	752.381	0.9981	0.576

Table 2.3: Central wavenumber ν_C in $[\frac{1}{\text{cm}}]$, coefficients A and B for the analytical relationship (Eq. 2.46) between temperature and radiance, [Tjemkes, 2005].

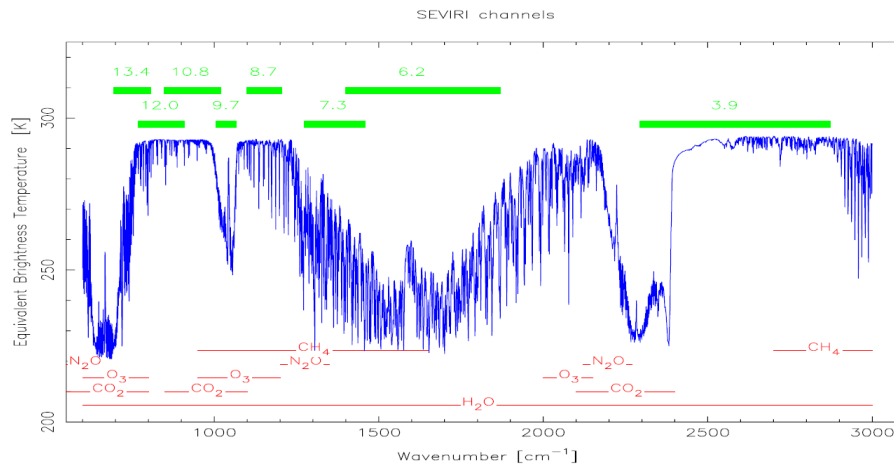


Figure 2.7: Upwards directed radiances at the upper limit of the “mid-latitude summer” atmosphere, transformed to the equivalent brightness temperature and plotted as a function of the wave number. Depicted are also the spectral region of the main influencing atmospheric constituents [Tjemkes and Schmetz, 1998].

transformed to equivalent brightness temperatures, Eq. 2.46, and are plotted as a function of wave number. Fig. 2.7 points out that the so-called window channels IR087, IR108, and IR120 are in a spectral region with low gas absorption. In the IR134 channel, water vapour as well as carbon dioxide absorb radiation. In the so-called water vapour channels WV062 and WV073 high absorption due to water vapour is present. In the spectrum of the IR097 absorption by ozone is dominant along with methane and carbon dioxide. Methane absorption can also be observed in the WV073 channel. Since atmospheric absorption is not uniform with altitude, each SEVIRI channel has a varying sensitivity to different atmospheric layers. Fig. 2.8 shows the weighting function [Tjemkes, 2005] for the thermal infrared channels of SEVIRI for a satellite viewing angle of 55° for a “mid-latitude summer” atmosphere.

The weighting functions of channels IR087, IR108, and IR120 reach down to the Earth’s surface, while the water vapour channels WV062, WV073 have lower or no contribution from the lower atmospheric layers, so the measured brightness temperatures are almost independent from the surface temperature. Although in very dry areas the WV073 channel is still influenced by surface temperature, in more moist regions the weighting function is altered so that the ground is not detected any more. In particular, in regions with optical thick water or ice clouds the WV073 observations only contains information from the cloud top and above due to the strong absorption of clouds.

The absorption of water and ice particles forming clouds in the Earth’s atmosphere is depicted in Fig. 2.9, where one should focus on the thermal infrared channels marked as columns with wavelengths greater than $6.2 \mu\text{m}$. The red line represents the absorption

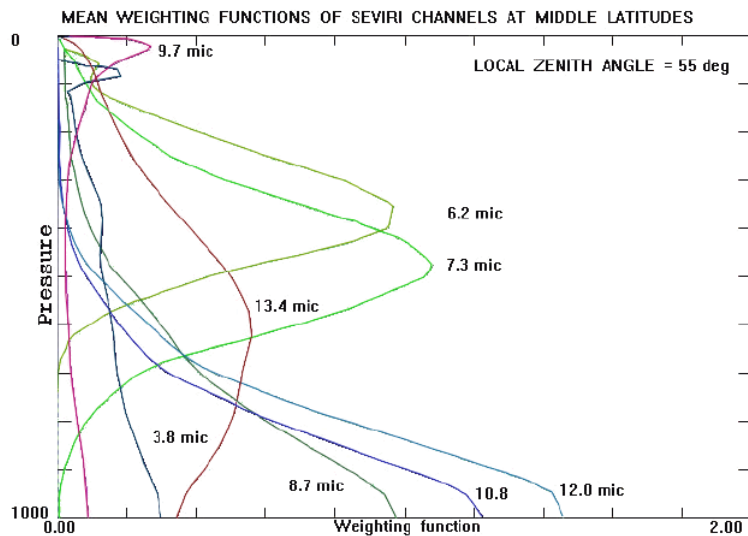


Figure 2.8: Weighting functions of the infrared channels of SEVIRI for a “mid-lat summer” atmosphere and a viewing angle of 55° typical for Europe [Tjemkes, 2005].

of ice, the blue line is valid for water. Different absorption characteristics are found for the single channels: While ice and water particles absorb radiation in the whole thermal spectrum, differences in the absorption makes the discrimination of ice and water clouds possible. Especially the two water vapour (WV062 and WV073) and the split window channels (IR108 and IR120) show larger imaginary refraction indices for ice particles than for water.

In case of optically thin cirrus clouds, the window channels still receive information from the ground. In this case, only a combination of the different infrared channels can provide quantitative information about the cloud temperature, its optical properties, or height (see Section 3).

2.2.3 Derivation of cirrus cloud properties from passive remote sensing

Several passive remote sensing instrument aboard numerous geostationary and polar orbiting satellites have already been used in the past decades to detect cirrus clouds and to retrieve their properties. These remote sensing applications aim to extract parameters of the medium (i.e. cirrus clouds) from a set of radiative measurements, namely the radiances or brightness temperatures sampled in several illumination and observation conditions and spectral bands. Liou [1977] presented a hypothetical retrieval to determine the surface temperature, the thickness and the transmissivity of cirrus clouds based on four different infrared channels (8.7, 9.0, 10.5, and $11.0 \mu\text{m}$) located in the $10 \mu\text{m}$ window region. Justified by radiative transfer calculations, two assumptions were made for these

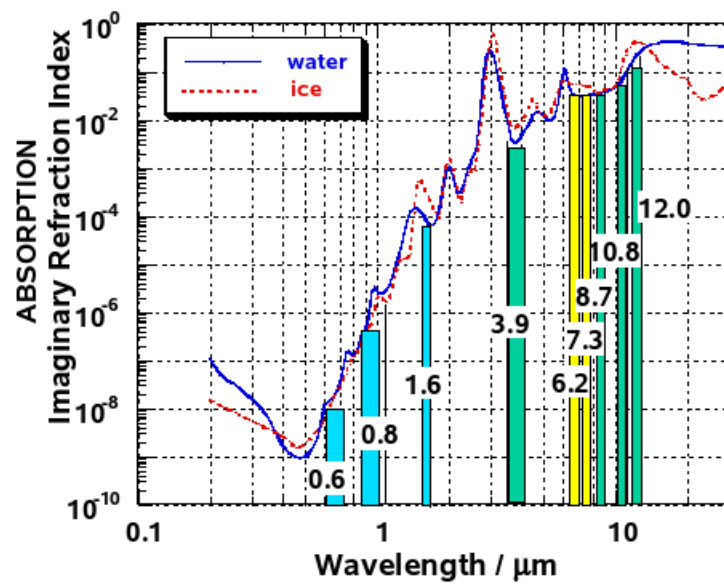


Figure 2.9: The absorption (Imaginary Refractive Index) of ice (red) and water (blue) depicted as a function of wavelength. Green and yellow columns mark the spectral bands of the infrared channels of the SEVIRI instrument, adapted from D. Rosenfeld, EUMETSAT MSG Interpretation Guide.

theoretical analysis: Water vapour effects above cirrus clouds are negligible and the ratios of transmissivities are linear functions of the cloud thickness. Szejwach [1982] developed a technique using the water vapour absorption channel ($5.7 - 7.1 \mu\text{m}$) and the so-called window channel $10.5 - 12.5 \mu\text{m}$ of the Meteosat geostationary satellites to derive cirrus cloud temperature, emissivity, and height (known as the H_2O -intercept method).

Both utilized the existence of different emissivities of cirrus clouds in the different infrared channels due to scattering and absorption of ice crystals in the cloud. Based on radiative transfer calculation with calculated vertical profiles of e.g. temperature and moisture the cirrus top altitude can be derived from the measured radiances [Menzel et al., 1983, Wylie and Menzel, 1989]. This last method is also called CO_2 -slicing, since one specific wavelength (around $13 - 14 \mu\text{m}$) sensitive to the absorption of CO_2 is used.

In case of non-opaque thin cirrus clouds, measured radiances or brightness temperatures include contributions from the cirrus cloud as well as from the surface and atmosphere below. Thus, the detection of cirrus clouds and especially thin cirrus clouds is supported by several multi-spectral techniques. E.g. the semi-transparency or “split-window” test based on two infrared channels, 10.8 , and $12.0 \mu\text{m}$, is often used [Inoue, 1985]. Again the physical basis of this algorithm is the difference in the single scattering properties of ice clouds at these two wavelengths. Additionally, Krebs et al. [2007] exploits the morphological properties of cirrus in the water vapor channels like 6.2 , and $7.3 \mu\text{m}$ on SEVIRI. Water vapor channels are ideally suited for cirrus detection, as absorption and emission

by atmospheric water vapor effectively shields surface and lower clouds.

In order to retrieve the microphysical properties of cirrus clouds two kinds of approaches emerged: empirical parameterizations derived from in situ measurements, and physical methods using optimization techniques and/or look-up tables. Liou [1977] already stated, that once the geometrical thickness and transmissivity at a given wavelength of a cirrus cloud have been derived, the vertical ice content of that cloud may be estimated. In Liou et al. [1990] a dual-channel technique was developed using 6.5 and 10.5 μm wavelengths for the retrieval of the temperature and optical thickness of tropical cirrus clouds. This technique is based on a theoretical parametrisation of the cloud emissivity as a function of the optical depth.

Nowadays the retrieval of microphysical properties of cirrus clouds is often based on a method developed by Nakajima and King [1990]. In order to derive these microphysical properties like ice optical thickness and particular effective radius, look-up tables are calculated with radiative transfer models. In these look-up tables reflectivities are calculated and stored as a function of several parameters such as sun zenith angle, sensor zenith angle, relative azimuth angle, surface albedo, cloud optical thickness, and effective particle radius [Bugliaro et al., 2011]. These methods are based on the fact that the reflection function of clouds in the visible is primarily a function of cloud optical thickness, whereas the reflection function in the near-infrared depends primarily on the cloud particle size [Arking and Childs, 1985, Han et al., 1994, 1995], which limits their applicability to daylight measurements. During nighttime, the retrieval of microphysical properties is more complex, because the radiances retrieved in the infrared bands depend on every cloud parameter. In these cases, applied methods are based on the fact that the optical properties of clouds are different at each infrared wavelength [Baum et al., 1994, 2003]. Thus, the different thermal infrared channels of SEVIRI covering wavelengths from 6.2, and 13.4 μm (Section 2.2.2) are well suited to detect cirrus clouds and to retrieve their optical thickness and top altitude during day and night. The functional relationship of brightness temperatures and brightness temperature differences to the retrieved properties of cirrus clouds is shown in Section 3.5.

2.3 Active remote sensing

The influence of active remote sensing on atmospheric science has grown in the last decade. Especially active remote sensing like light detection and ranging (lidar) and radio detection and ranging (radar) has become fairly common. Like radar, lidar is mainly used for profiling the Earth's atmosphere. High spatial resolution of the measurements, the potential of covering the height range from the ground to high altitudes, observations during night, including the high flexibility like measurements from an aircraft or even from space make this kind of observations even more attractive (for an overview of lidar and its atmospheric applications see Weitkamp [2005]).

2.3.1 Lidar principle

In general, a lidar consists of three subsystems: the transmitter, the receiver, and the detection system. The light amplification by stimulated emission of radiation (laser) transmitter is the light source, which emits photons in a pulsed beam. As already mentioned, those photons are scattered by atmospheric molecules (oxygen, nitrogen, etc.) and particles (clouds and aerosols). Rayleigh scattering occurs when the wavelength of the propagating light is much larger than the diameter of the particles. Due to the wavelength dependency of the intensity of Rayleigh scattering with λ^{-4} , shorter wavelengths are scattered far more than larger wavelengths. Aerosols and clouds, which are atmospheric particles with a diameter close to, or even larger than the wavelength of the radiated light scatter radiation according to Mie theory. Here, the intensity of the backscattered light depends on the particle concentration and not or only slightly on the wavelength. It increases simultaneously with air pollution, clouds, fog, and haze. Fig. 2.10 shows a schematic overview of a spaceborne lidar, such as the instrument CALIOP aboard the CALIPSO satellite (see Section 2.3.2). The receiver collects the light backscattered by the atmosphere with a telescope. The transmitter emits laser pulses (red) in direction of the lidar line-of-sight (yellow). These pulses are backscattered by atmospheric molecules, aerosols, cloud particles, and the surface. The collected signal is time-dependent. Using the equation $R = \frac{c \cdot t}{2}$, the time t between the transmission of the laser pulse and the reception of the backscattered signal can be directly related to the range R , where the scattering occurs. The typical signal of a spaceborne lidar is shown at the right top of Fig. 2.10, where the first and second peak are caused by aerosols and clouds respectively, whereas the strongest peak is the ground return signal. The number of photons received by the lidar at a range z from a range-bin depends on the one hand on the lidar system itself, e.g. the number of photons emitted by the laser and the length of the so-called sampling interval, described by the lidar constant K . On the other hand, as mentioned

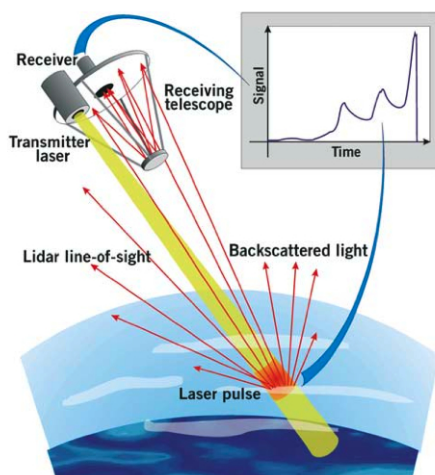


Figure 2.10: Schematic description of a spaceborne lidar [Endemann, 2006].

above, the received number of photons strongly depends on atmospheric conditions, such as the efficiency of the backscattering of particles and air molecules at range z to the lidar, and on the probability that emitted photons are backscattered to the receiver from range z without being absorbed or scattered in arbitrary directions. The number of photons received by a lidar can be calculated with the lidar equation in terms of the received energy $E(z, \lambda)$ from a range-bin at range z at a wavelength λ :

$$E(z, \lambda) = K \frac{\beta_m(z, \lambda) + \beta_p(z, \lambda)}{z^2} \exp \left\{ -2 \int_0^z [\alpha_m(z', \lambda) + \alpha_p(z', \lambda)] dz' \right\}, \quad (2.47)$$

where K is the above mentioned lidar constant, and backscatter and extinction coefficients are denoted as β in units of $[\text{km}^{-1}\text{sr}^{-1}]$ and α in units of $[\text{km}^{-1}]$, respectively. The subscripts p and m are added to distinguish between the contributions of particles and molecules. The two-way transmission between the lidar and the range z is written as the exponential term on the right hand side to describe the loss of photons due to atmospheric extinction by particles and molecules.

2.3.2 CALIOP - CALIPSO

Spacecraft

Launched in April 2006, the CALIPSO mission provides global observations of aerosols and clouds with its onboard lidar Cloud-Aerosol Lidar with Orthogonal Polarization (CALIOP), the Imaging Infrared Radiometer (IIR), and the Wide Field Camera (WFC). CALIPSO flies as a part of the National Aeronautic and Space Administration (NASA)

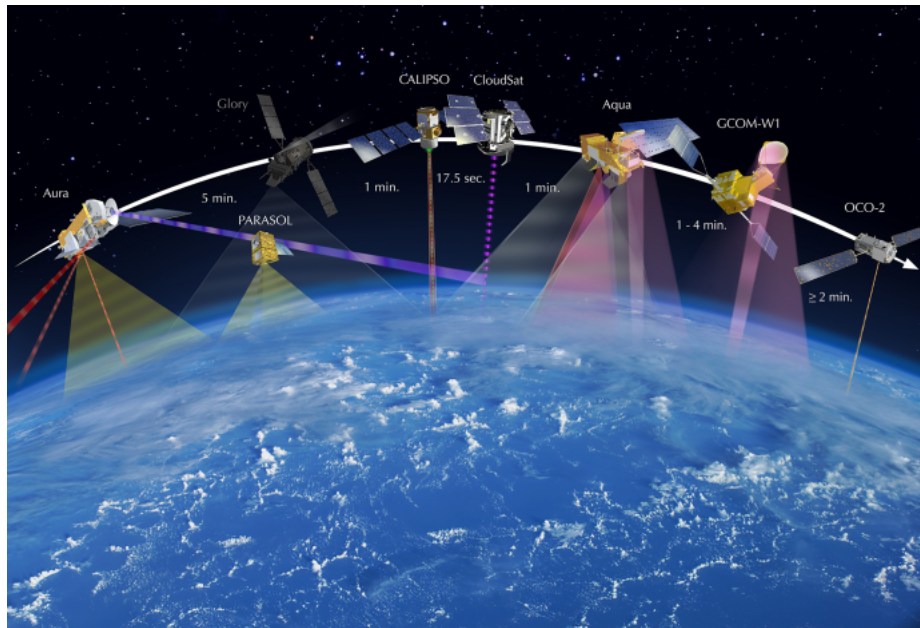


Figure 2.11: NASA afternoon train [<http://atrain.nasa.gov/images.php>].

afternoon constellation (A-Train) together with Aqua, CloudSat, PARASOL, and Aura (Fig. 2.11). The Global Change Observation Mission - Water (GCOM-W1) and the Orbiting Carbon Observatory (OCO-2) are going to be launched in 2012 and 2013 respectively. Unfortunately the GLORY spacecraft failed to reach its orbit after liftoff in March 2011. CALIPSO was injected into a polar orbit of 705 km with a repeat cycle of 16 days. All satellites together provide simultaneous measurements of aerosols, clouds, relative humidity, temperature, and radiative fluxes for the first time [Winker et al., 2002].

CALIOP

For this purpose CALIOP uses a Nd:YAG laser emitting simultaneous, co-aligned pulses at wavelengths of 1064 nm and 532 nm with a repetition rate of 20.16 Hz equal to a distance of 333 m between two profiles each with a footprint of 100 m along and 90 m cross track, a 1 m-diameter telescope, and three receiver channels, which collect the backscattered signals. One channel measures the 1064 nm backscatter intensity and two channels measure orthogonally polarized components of the 532 nm backscatter signal. Hence, it is possible to derive the backscatter coefficients (532 nm and 1064 nm), the color ratio of the backscatter coefficients ($\frac{532 \text{ nm}}{1064 \text{ nm}}$), and the depolarization ratio of the 532 nm channels [Winker et al., 2007]. As with ground-based depolarization lidars, CALIOP relies on polarization information to determine cloud phase, based on the assumption that water cloud particles are spheres and ice clouds are composed of nonspherical particles Hu et al. [2009]. Beside vertical profiles of aerosols, CALIPSO delivers vertical profiles of clouds,

primarily from the 532 nm channel. The vertical resolution of the 532 nm channel is altitude dependent from 30 m (up to 8.2 km) to 300 m (30 – 40 km), which is similar to the resolution of the 1064 nm channel.

Algorithms

For each profile of CALIOP, cloud and aerosol layers are detected by a threshold detection technique [Vaughan et al., 2004, 2005, 2008, Winker et al., 2009].

Before the retrieval of extinction coefficients can be performed, clouds must be located and discriminated from aerosol, and water clouds must be discriminated from ice clouds. Therefore the Selective Iterated Boundary Locator (SIBYL) detects layers, the Scene Classification Algorithm (SCA) classifies these layers, and the Hybrid Extinction Retrieval Algorithms (HERA) perform extinction retrievals. The location of cloud and aerosol layers and the determination of cloud ice/water phase are necessary precursors to extinction retrieval. Assuming, that the CALIOP profile data has been properly geolocated and calibrated during the first step of data processing, the primary measurement quantity used in the Level 2 data processing here will be range-resolved profiles of attenuated backscatter coefficients, $\beta'(\lambda, r)$:

$$\beta'(\lambda, r) = \frac{r^2 P(\lambda, r)}{K} = [\beta_m(\lambda, r) + \beta_p(\lambda, r)] T_m^2(\lambda, r) T_p^2(\lambda, r) T_{O_3}^2(\lambda, r). \quad (2.48)$$

Again, K represents the system constant similar to Eq. 2.47 and $P(\lambda, r)$ is the received lidar signal at range r from the satellite. The single backscatter coefficients are given by $\beta(\lambda, r)$ with the subscript m for molecules and p for particles. The two-way transmittance due to any scattering or absorbing species is given by T^2 with the subscript O_3 for ozone additional to particulate and molecular contributions. The task of this feature finding algorithm is to separate features in the retrieved signal from the noise. The fundamental algorithm to locate any layer within a profile measured by CALIOP is the SIBYL algorithm, which is driven by a profile-scanning engine originally developed for application to ground-based observations [Winker and Vaughan, 1994] and later adapted to the Lidar In-space Technology Experiment (LITE) [Platt et al., 1999]. The scanning for the feature begins at the top of the profile and data points are examined sequentially, with features being identified at those regions where the profile data exceed their corresponding threshold values over an altitude range greater than some predetermined minimum feature thickness. The scanning procedure is applied to the 532 nm attenuated scattering ratios R' :

$$R'(r) = \frac{\beta'(r)}{\beta_m(r)t_{s,m}^2(r)t_{s,O_3}^2(r)} = \left(1 + \frac{\beta_p(r)}{\beta_m(r)}\right) t_{s,p}^2(r). \quad (2.49)$$

These attenuated scattering ratio profiles are analysed in order to exploit a very specific geometric structure. In case of a noise-free profile, the slope of R' with respect to altitude would be exactly zero, which is essentially the case for high altitudes in the measured data. This fact is shown in Fig. 2.12, where R' derived from LITE data is depicted as a function of altitude. On the left hand side “clear air regions” show values of $R' \approx 0$ at altitudes from 22 to 17.5 km and from 12 to 3 km. The adaptive thresholding scheme incorporated into the CALIOP profile scanner uses local topographical information to identify regions of clear air at feature base, and to adjust the threshold array to compensate for the signal attenuation imparted by the newly located feature. In the center of Fig. 2.12, the initial threshold (in red) calculated at the beginning of the scan is depicted. There the cirrus cloud at an altitude between 17.4 and 13.2 km lies above this threshold and thus is detected. But the aerosol layer between 1.6 km and the surface would be dismissed since its scattering ratio lies below the initial threshold. Therefore, the revised threshold (in red), depicted in Fig. 2.12 right, is automatically computed upon exiting the base of the cirrus layer. The regions identified as features are now plotted in green, while regions not exceeding the revised threshold are drawn in grey. This automated scaling of the threshold array for every profile to account for signal attenuation due to detected features makes the subsequent detection of underlying features possible, which would be missed otherwise. Finally the integrated attenuated backscatter of the feature γ_{feature} can be calculated as:

$$\gamma_{\text{feature}} = \int_{\text{top}}^{\text{base}} \beta_p(r) \cdot t_{s,p}^2(R) dR, \quad (2.50)$$

where $\beta_p(R)$ is the particular backscatter and $T_p^2(R)$ is the particulate two-way transmittance.

Once all the features are identified by SIBYL, another set of algorithms is applied in the second step, the so-called the Scene Classification Algorithm (SCA). The SCA classifies the features found by SIBYL by type. The SCA decides whether the detected layer is a feature or a non-feature by using the flag derived by SIBYL. Atmospheric features first have to be distinguished in clouds and aerosols. In a second step these features are then classified in sub-types. Non-features are regions of clear air, surface, subsurface, or total attenuation, where no underlying layers or surface can be detected. If the region is labelled as surface, subsurface, or totally attenuated, the SCA records this in

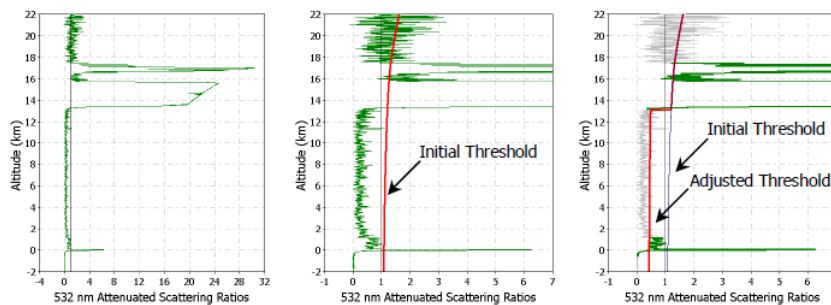


Figure 2.12: Adaptive threshold technique applied to attenuated scattering ratios measured during LITE [Vaughan et al., 2004].

the Vertical Feature Mask (VFM). In case of clear-air the SCA records the appropriate clear-air lidar ratio for the region in the VFM. Is the detected region a feature the SCA checks, if the feature is elevated (molecular scattering signal has to be available above and below the feature). For an elevated feature the SCA calculates the lidar ratio by using the transmittance-constraint method. As mentioned above, the transmittance method requires clear air (molecular scattering) above and below the detected layer, from which the layer transmittance and therefore the optical depth can be determined, [Fernald et al., 1972, Young, 1995]. The extinction-to-backscatter ratio or the lidar-ratio S is generally defined as:

$$S = \frac{\alpha}{\beta}, \quad (2.51)$$

where α is the extinction and β is backscatter coefficient. The lidar ratio depends primarily on properties such as size distribution, particle shape, and composition. Concerning aerosols these factors are the source of the aerosols, mixing, transport, and hydration. This method is based on the relationship between optical thickness τ and integrated attenuated backscatter, Equation 2.50, which is described by the following equation, [Platt, 1973]:

$$\gamma' = \frac{1 - \exp(-2\eta\tau)}{2\eta S}. \quad (2.52)$$

Here γ' is the integrated attenuated backscatter from layer top to layer base, Eq. 2.50. τ is the optical thickness and η is a layer-effective multiple scattering parameter. It is important to mention, that Eq. 2.52 is only valid for the single component layers where molecular scattering is negligibly small compared to particular scattering (e.g.

in clouds). In aerosol layers the molecular scattering can be significant and must be taken into account in using Eq. 2.52 to compute the lidar ratio. To use Eq. 2.52, a technique has been developed to correct for the molecular scattering. The molecular scattering correction technique approximates the molecular scattering contribution to the total integrated attenuated backscatter, [Liu et al., 2005].

Furthermore, Liu et al. [2005] defines an effective lidar ratio, $S^* = \eta \cdot S$ and substitutes the effective two-way transmittance, $t_s^2 = \exp(-2 \cdot \eta \cdot \tau)$, therefore Equation 2.52 can be rewritten as:

$$S^* = \frac{1 - t_s^2}{2\gamma'}. \quad (2.53)$$

The effective two-way transmittance is obtained by fitting the return above and below a feature to a reference profile, [Young, 1995]. The uncertainties in the observationally approximated value of S are estimated and the SCA then sets a flag indicating whether the extinction retrieval should perform a retrieval using the observational value or the model value. If the feature is non-elevated the transmittance method fails to be applied and a lidar ratio is selected based on different models corresponding to the identified feature type. In case of aerosols the underlying paradigm of the type classification is that the variety of emission sources and atmospheric processes will act to produce air masses with a typical identifiable aerosol type, [Liu et al., 2005]. The aerosol lidar ratio S_a is based on several studies, [Ansmann et al., 2001, Masonis et al., 2002, Liu et al., 2002, Voss et al., 2001]. A detailed overview is given in Liu et al. [2005] with the single lidar ratios for the different aerosol types such as marine aerosol, polluted dust, and biomass burning. For clouds the Cloud Model Algorithm (CMA) determines consistent values of the cloud lidar ratio S_c and the multiple scattering function $\eta_c(z)$ for all cloud layers. For water clouds the SCA chooses a constant value of the lidar ratio $S_c = 18$ sr, based on theoretical studies, [Pinnick et al., 1983]. For cirrus clouds an empirical relation between temperature and the lidar ratio S_c is selected according to the simple rule:

$$S_c = -1.2591 \cdot T - 6.698, \quad (2.54)$$

where T is the mid-cloud temperature in °C derived from the observed cloud layer heights using the ancillary data product of the Global Modelling and Assimilation Office (GMAO). As a last algorithm the Hybrid Extinction Retrieval Algorithm (HERA) is applied. It calculates and corrects for the attenuation within all features in order to produce profiles of extinction and backscatter at both wavelengths, 532 nm and 1064 nm. The fundamental

algorithms in HERA take as inputs a collection of integrated quantities derived from some segments of a profile in case of the SCA (e.g. ice/water phase). The outputs are either a derived profile of optical parameters (e.g. particulate extinction coefficients), the integral of such profiles (e.g. optical thickness), or some additional information about the content or structure of the input profile (e.g. base and top altitude). The detailed formulas and error estimations can be found in Young et al. [2008], but finally the solution of HERA is the extinction coefficient $\alpha_p(r)$:

$$\alpha_p(r) = S_p \cdot \beta_p(r). \quad (2.55)$$

With the calculated extinction coefficient HERA finally derives the optical thickness τ_p for each detected layer:

$$\tau_p = \int_{r_0}^{r_1} \alpha_p(r) dr. \quad (2.56)$$

In version 2.01 and version 2.02 the HERA retrieval only calculates cloud extinction coefficients of the 532 nm channel in contrast to the aerosol extinction coefficient, which are derived for both wavelengths, 532 nm and 1064 nm. Therefore, the ice optical thickness of the 532 nm channel is used in this work.

Several attempts to validate the retrieved cirrus cloud properties of CALIOP were accomplished in the past few years. Rogers et al. [2011] used measurements of the airborne High Spectral Resolution Lidar (HSRL) of the NASA Langley Research Center in June 2006 to validate the 532 nm total attenuated backscatter. The CALIOP measurements were found to agree to the backscatter coefficients derived by HSRL with a slight underestimation of $2.7 \% \pm 2.1 \%$ during nighttime and $2.9 \% \pm 3.9 \%$ during daytime.

During the CIRCLE-2 experiment in May 2007 the extinction coefficients for thin cirrus clouds derived by CALIOP were compared to in situ measurements of a Polar Nephelometer aboard the research aircraft Falcon of the DLR [Mioche et al., 2010]. On the one hand both extinction coefficients were found to agree (slope parameters of the linear fits greater than 0.9) with a very good correlation for thin cirrus clouds and extinction coefficients between 0.6 to 1.2 km^{-1} for irregular-shaped ice crystals. On the other hand an overestimation of the CALIOP extinction coefficients was found due to pristine-plate crystals with sizes up to $300 \mu\text{m}$. In order to avoid subsequent biases in CALIPSO retrieval products, the CALIOP laser beam has been tilted 3° ahead of the nadir direction since November 2007. Most recently Hlavka et al. [2012] published validation

results on cirrus cloud optical properties derived from CALIOP measurements during the CALIPSO-CloudSat Validation Experiment (CC-VEX). Compared to the airborne Cloud Physics Lidar (CPL) differences in the resulting optical thickness of only $\sim 7\%$ for the values derived by CALIOP was found in case of agreeing lidar ratios. However in case of disagreeing lidar ratios of both systems, the resulting optical depth difference is significant (31 %).

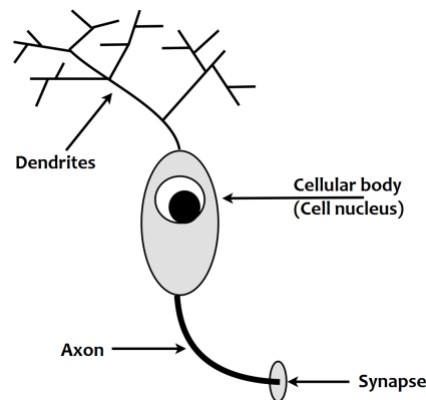


Figure 2.13: Scheme of a biological archetype of a neuron.

2.4 Neural Networks

This section explains the theory of artificial neural networks with the main focus on back-propagation neural networks on which the algorithm developed in this thesis is based. Artificial Neural Networks try to emulate the human brain. As millions of our interconnected brain cells are trainable and then take over control task, we would like to empower computer programs to handle new situations with learned informations in a similar way.

2.4.1 Biological Archetype

In 1943 Warren McCulloch and Walter Pitts tried to understand how the human brain can carry out highly complex relationships such as reading by using many basic cells that are connected with each other [McCulloch and Pitts, 1943]. The biological archetype (Fig. 2.13) is only described briefly here, since it is not essential to understand the theory of artificial neurons. For a more detailed disquisition on the biological background, please see Zeil [1997]. Dendrites are the branched projection of a neuron that act to conduct the electrochemical stimulation received from other neural cells to the cell body of the neuron from which the dendrites project and remits it to the cell nucleus. The axon is a long, slender projection of a neuron that typically conducts electrical impulses away from the neuron's cell body to the dendrites of other cells. A biological neuron has some thousand connections to other neurons. The connection of the axon of one neuron to the dendrite of another neuron is called synapse. In computer science, an artificial neural network is a mathematical or computational model inspired by the structure and functional aspect of these biological networks.

2.4.2 History of Artificial Neural Networks

With their publication McCulloch and Pitts [1943] gave a very simplified mathematical model of these biological neurons, which highly contributed to the development of artificial neural networks. Four years later, in 1947, both stated that pattern recognition in general is possible using artificial neural networks, [Pitts and McCulloch, 1947]. An example of pattern recognition is classification, which attempts to assign each input value to one given set of classes (e.g. whether an email is “spam” or “no-spam”). The first to define learning rules for an artificial neural network was Donald O. Hebb two years later. In the so-called Hebbian theory or Hebb’s rules he stated [Hebb, 1949]: “Let us assume that the persistence or repetition of a reverberatory activity (or “trace”) tends to induce lasting cellular changes that add to its stability. When an axon of cell A is near enough to excite a cell B and repeatedly or persistently takes part in firing it, some growth process or metabolic change takes place in one or both cells such that A’s efficiency, as one of the cells firing B, is increased.”

This statement aims to explain “associative learning” , in which simultaneous activation of cells leads to pronounced increases in synaptic strength between those cells, or, in other words, the connection between both neurons becomes more important and is strengthened. Accordingly, this rule is often generalized as:

$$\Delta\omega_i = \eta x_i y , \tag{2.57}$$

where the change in the i -th synaptic weight $\Delta\omega_i$ is equal to a learning rate η times the i -th input x_i times the postsynaptic response y , which is somewhat the output of the neuron. In 1950 Karl Lashley found that memories are stored in a decentral process all over the brain [Lashley, 1950]. During the next 20 years first attempts to match patterns with neuron computers were successful. Some time later in 1974, Paul Werbos wrote down the first description of training an artificial neural network by back propagating errors [Werbos, 1974].

2.4.3 General setup of Artificial Neural Networks

As mentioned above, neural networks consist of several neurons that are used to gather informations from ambience or other neurons and to send this information back to ambience in a modified way or again to other neurons. In general, artificial neural networks consist of three different types of neurons: Input neurons, hidden neurons, and output neurons:

- Input neurons: Neurons that receive signals (stimuli, pattern, etc.) from ambience

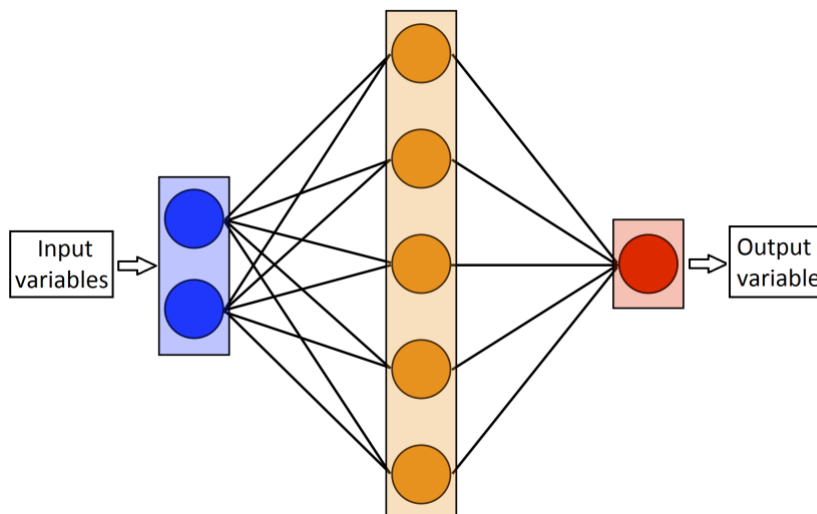


Figure 2.14: Setup of a simple neural network with input neurons in blue, hidden neurons in orange, and output neurons in red.

- Hidden neurons: Neurons between input and output Neurons, internal representation of environment.
- Output neurons: Neurons to transmit signals to ambience. They combine the signals from the hidden layer(s).

Neurons of the same type are combined to layers (Fig. 2.14). The neurons of the input layer are connected to the neurons of the hidden layer, which are once again connected to the output layer neurons. The strength of the connection between two neurons is defined by a weight. The higher its value the greater is the influence of one neuron on the other. Those weights represent the memory of an artificial neural network.

2.4.4 Backpropagation Neural Network

An artificial neural network is generally based on a process with three steps.

In the first step the input variables are “received” by the neurons of the input layer. Thus, if ten input variables $n = 10$ are used ten corresponding input neurons are selected for the input layer. Within each input neuron the variable is transformed by a function, the so-called “activation function”. In biologically-inspired neural networks, the activation function is usually an abstraction representing the rate of action potential firing in the cell. The simplest function is the so-called Heaviside / step function, which is a discontinuous function with values of zero or one deciding whether the neuron is “activated” or “firing”. A linear activation function with variable slope may also be used to reflect the increase in firing rate that occurs as input current increases. Neural networks based on this function

show numerical instabilities because neuron inputs along favoured paths tend to increase without bound. In case of backpropagation neural networks, the activation function has to be bounded and continuously differentiable. For that purpose, the sigmoid function $\phi(t)$ is used in most cases, which is defined for the real domain with exactly one inflexion point. Furthermore, its first derivative is throughout positive or negative. The sigmoid function is defined for $0 \leq \phi(t) \leq 1$ as:

$$\phi(t) = \frac{1}{1 + \exp(-t)}, t \in \mathbb{R}. \quad (2.58)$$

Thus, in case of the input layer, for each of the $n = 10$ neurons the sigmoid function for $t_n = \text{Input}_n$ is calculated in the first step and send via the connections to the neurons of the hidden layer, where again the sigmoid function is applied.

According to the Hebbian theory these connections are weighted by the synaptic strength $g_{i,n}$. The amount of connections and therefore the number of connections between input and output neurons is determined by the number of connections between input and hidden layer neurons. So, assuming that exemplary 100 neurons are used here and since each neuron of the input layer is connected to every neuron of the hidden layer, 1000 connections between the $n = 10$ input neurons and the $i = 100$ hidden neurons have 1000 weights $g_{i,n}$. In the hidden layer neurons the sigmoid function is again applied to the result of each input neuron $\phi(t_n)$. But since the connection between these neurons is weighted by $g_{i,n}$, each hidden layer neuron receives the values from the input neurons:

$$u_i = \sum_{n=1}^m \phi(t_n) \cdot g_{i,n}. \quad (2.59)$$

Thus, the value for each of the $i = 100$ hidden layer neurons is assigned to $\phi(u_i)$. Fig. 2.15 gives a schematic overview in which way the neurons of one layer (here: the input layer) are connected to one neuron of the following layer (here: hidden layer). As mentioned above, the strength of the connections are weighted with the factors $g_{i,n}$, which are randomly distributed in the beginning. n is the number of inputs, i is the number of hidden layer neurons. On the left of Fig. 2.15, the input variables are depicted.

In the second step (Fig. 2.16) the value of each output layer neuron is determined again with the sigmoid function (Eq. 2.58). The number of output layer neurons depends on the variables the neural network shall determine. Here, for example, two variables shall be determined. Therefore, $o = 2$ output layer neurons are chosen, which are connected to each of the hidden layer neurons forming 200 connections. Again the strength of the

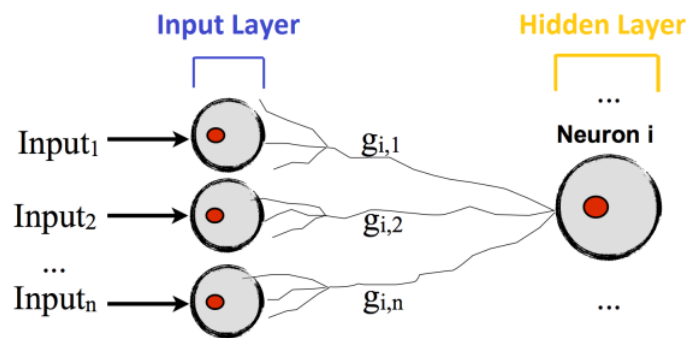


Figure 2.15: Schematic overview of connections, weights $g_{i,n}$, and neurons of the input and hidden layer in an artificial neural network.

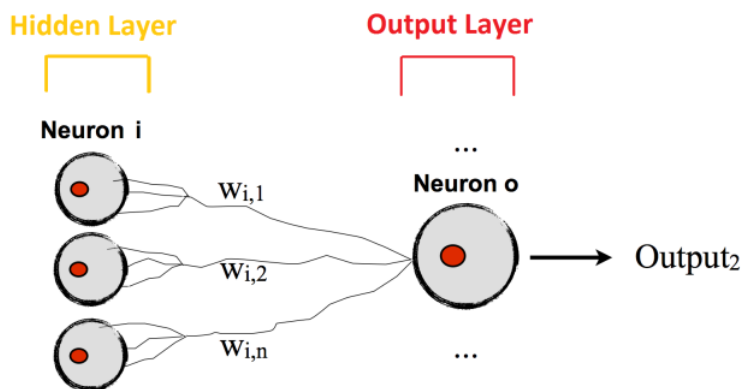


Figure 2.16: Schematic overview of connections, weights, and neurons of the hidden and output layer in an artificial neural network.

connections are weighted with $w_{i,o}$. Consequently, the value received by an output neuron from the hidden layer neurons forms as

$$v_o = \sum_{i=1}^m \phi(u_i) \cdot w_{i,o}, \quad (2.60)$$

and the sigmoid function $\phi(v_o)$ is applied once more to determine the value of the output neurons. Finally, the third step is the eponym of the backpropagation neural network. Here, the calculated output values of the neural network are compared to the expected output values, also called target values x_o , by inverting the value of each output neuron calculated by the sigmoid function $\phi(v_o)$. The difference between both values is then

deemed as error. Thus, the quality of a neural network is given by the error function E :

$$E = \frac{1}{2} \sum_{o=1}^m (\phi(x_o) - \phi(v_o))^2. \quad (2.61)$$

The factor $\frac{1}{2}$ is used to alleviate the later used deviation of E . This error now has to be propagated back from the output layer to the input layer by changing the weights of the connections between single pairs of neurons depending on their influence on the error. The error backpropagation is done for each weight in the neural network exemplified in the following (Fig. 2.17).

In order to minimise the error the weight $w_{i,2}$ has to be changed with:

$$\Delta w_{i,2} = -\eta \frac{\partial E}{\partial w_{i,2}}. \quad (2.62)$$

The partial derivative of the error function $\frac{\partial E}{\partial w_{i,2}}$ can be calculated according to the chain rule:

$$\frac{\partial E}{\partial w_{i,2}} = \frac{\partial E}{\partial \phi(v_2)} \cdot \frac{\partial \phi(v_2)}{\partial v_2} \cdot \frac{\partial v_2}{\partial w_{i,2}}. \quad (2.63)$$

Finally this leads to:

$$\Delta w_{i,2} = -\eta \delta_{\phi v_2} x_2, \quad (2.64)$$

with the so-called learning rate η , which is chosen to influence the speed and the precision of the error minimisation and

$$\delta_{\phi v_2} = \frac{d\phi(v_2)}{dv_2} \cdot (\phi(x_2) - \phi(v_2)) = \phi(v_2) \cdot (1 - \phi(v_2)) \cdot (\phi(x_2) - \phi(v_2)). \quad (2.65)$$

Therefore, the weight $w_{i,2}$ in this example is updated by

$$w_{i,2}^{new} = w_{i,2} + \eta \cdot \delta_{\phi(v_2)} \cdot \phi(v_2). \quad (2.66)$$

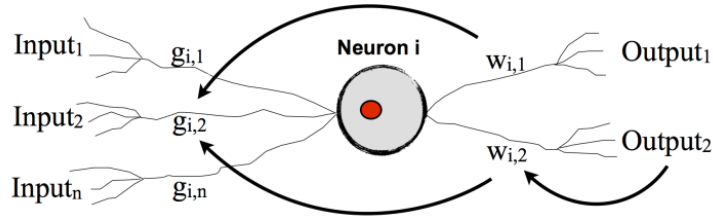


Figure 2.17: Schematic overview of the error backpropagation in an artificial neural network.

Eq. 2.65 is only valid for the weights between neurons of the hidden and the output layer (Fig. 2.17). For changing the weights $g_{i,n}$ between input and hidden layer, the changes in these weights have to be calculated indirectly, since the output neuron is not directly connected to the input layer.

For example the weight $g_{i,2}$ is updated similar to Eq. 2.66:

$$g_{i,2}^{new} = g_{i,2} + \eta \cdot \delta_{\phi(u_2)} \cdot \phi(u_2), \quad (2.67)$$

with the difference, that $\delta\phi(u_2)$ reads as

$$\delta_{\phi(u_2)} = \phi(u_2) \cdot (1 - \phi(u_2)) \cdot (\delta_{\phi(v_1)} \cdot w_{i,1} + \delta_{\phi(v_2)} \cdot w_{i,2}), \quad (2.68)$$

with the weights of the connections of the hidden neuron $w_{i,1}$ and $w_{i,2}$ to the output neurons $Output_1$ and $Output_2$.

As one can imagine, the error minimisation of a backpropagation neural network is an iterative process. Once the three steps described here are finished, the training can be repeated generally with different values for the input variables and the target values. This dataset is the so-called “training dataset”. After the training of the neural network with this dataset is finished it can be repeated aiming to minimise the error of the calculated results and the target value with every iteration. Depending on the information and quality of the training dataset several thousands of such iterations are needed until the error is as low as possible.

In general an artificial neural network combines an extremely flexible way to describe a parametric functional dependency of an output vector to an input vector with a method to determine its parameters (weights).

Chapter 3

COCS - Cirrus optical properties derived from CALIOP and SEVIRI during day and night

As described in Section 2.2.3 the retrieval of cirrus cloud properties from thermal infrared radiances/brightness temperatures is complex. Several brightness temperatures and brightness temperature differences have to be combined, each containing some information on the properties and altitude of the cirrus cloud. The majority of cloud retrieval algorithms is based on heuristically defined threshold to detect cirrus clouds and to retrieve their properties. The neural network approach aims to combine these information in a fast and accurate algorithm. This chapter introduces the Cirrus Optical properties derived from CALIOP and SEVIRI during day and night (COCS) algorithm, which is based on a backpropagation neural network (Section 2.4.4) and is applied on brightness temperatures derived by SEVIRI. In order to minimise the error between the calculated output and the expected value, the training dataset of SEVIRI and CALIOP measurements has to be as extensive as possible. The different data of CALIOP and SEVIRI utilized here as well as some auxiliary data are described, before a first example of the COCS algorithm is shown. Finally, the functional relationship between cirrus properties and brightness temperatures is shown.

3.1 Training dataset

The training dataset of COCS consists of three datasets: The first and most important data are the cirrus optical thickness τ and the cirrus top height z derived from CALIOP (Section 3.1.1). The second set of data are seven different infrared brightness temperatures and brightness temperature differences measured by SEVIRI (Section 3.1.2). The third set of data are so-called auxiliary data, such as latitude, viewing zenith angle of

SEVIRI, and a land-sea-mask (Section 3.1.3). In a total, the training dataset consists of nine million collocated measurements of SEVIRI and CALIOP for the timespan from July 2006 to June 2009.

Before May 2008 the calibrated radiances of the infrared channels of SEVIRI were provided as spectral radiances [EUMETSAT, 2007]. Brightness temperatures had therefore to be calculated by inverting the Planck function at the central wavelength of the channels. From May 2008 the radiance definition was changed so that it now represents the “effective radiance” over the instrument spectral response. Equivalent blackbody brightness temperatures must be computed now according to Eq. 2.46. This change in the radiance calculation results in differences of the retrieved brightness temperatures of up to 1.5 K in the single channels. Until now the archive at DLR contains data with both definitions. Thus, the dataset is divided in two parts and therefore two different neural networks are trained and applied later. The first covers the period from July 2006 to April 2008. The second dataset covers the time from May 2008 to June 2009.

Secondly the two datasets of SEVIRI brightness temperatures, auxiliary data, and CALIOP measurements are split once again. For both periods a total of eight million measurements are used for training of the two neural networks (COCS period 1 and 2) covering the periods above. Additionally one million measurements are separated from the training dataset and used for further validation and testing of COCS, which is again separated in two test dataset according to the periods defined above.

3.1.1 CALIOP data

According to Section 2.3.2, cirrus ice optical thickness τ and top altitude z are derived from the CALIOP 5 km Cloud Layer product. These measurements are used for the training of the neural network as the so-called target values (Section 2.4.3). During a preliminary analysis, the Cloud Layer products in versions 2.01 and 2.02 were found to contain inaccurate classifications, where cirrus free parts of the atmosphere were labelled as cirrus clouds. In order to remove these false alarms from the training dataset, the CALIOP data have been filtered according to the following criteria:

First the mid-layer temperature as a part of the CALIOP Cloud Layer product, which is calculated for each layer by the GMAO at the geometric midpoint of the layer, is taken into account. By testing the CALIOP dataset an optimal threshold for the mid-layer temperature of the detected cirrus layer was found to be 243 K in order to achieve a low frequency of misclassification, since cirrus clouds generally form at high altitudes and low temperatures when water vapour undergoes deposition and forms ice crystals (Section 2.1).

Secondly and in order to complete the pre-filtering another threshold, the so-called “climatology dependent threshold” is applied. This threshold function aims to prevent the

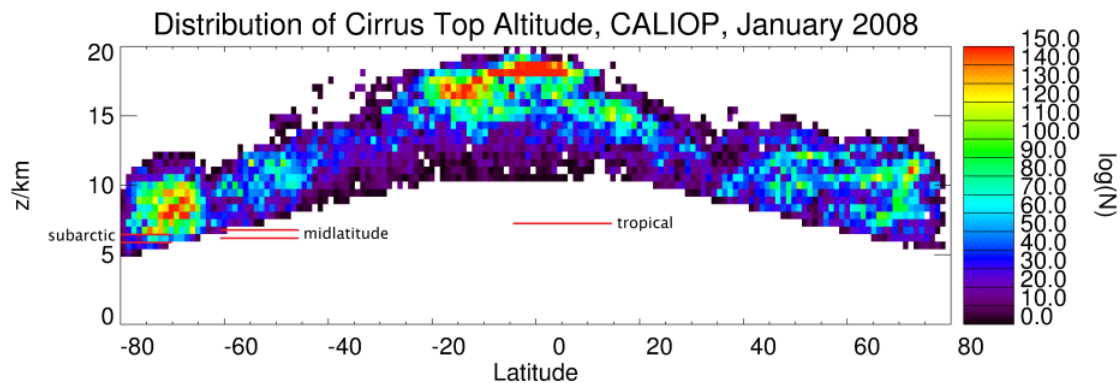


Figure 3.1: Cirrus top altitude distribution after applying all filters, January 2008. Red lines depict the 450hPa-level for different summer and winter U.S. Standard Atmospheres: subarctic winter/summer, midlatitude winter/summer and tropical standard atmosphere.

classifications of aerosols as cirrus clouds, which was found especially over tropical maritime regions at low altitudes. For absolute values of the latitude $|lat|$ greater than 22° the minimum top altitude of a cirrus cloud can be calculated as:

$$\text{limit}_{\text{top}}(lat) = 4.5 \text{ km} + \left(\frac{5.0 \text{ km}}{58.0} \right) (80.0 - |lat|). \quad (3.1)$$

For latitudes with $|lat| \leq 22^\circ$ the threshold altitude is kept constant at a value of $\text{limit}_{\text{top}}(lat) = 9.5 \text{ km}$. The threshold $\text{limit}_{\text{top}}$ is a simple approach based on the atmospheric temperature profile of Earth’s atmosphere. In high latitude regions it assumes that the cirrus cloud temperature of 243 K can be reached at altitudes of 4.5 km, while this altitude raises up to 9.5 km in tropical regions. This linear function is shown exemplarily for the distribution of CALIOP measured top altitudes in January 2008 (Fig. 3.1) over the MSG disc.

Logically, if the initial dataset of CALIOP contains cirrus-free measurements (no cirrus layer is detected by CALIOP) the cirrus ice optical thickness is set to zero. The same is valid for measurements of cloud-free scenes. A final filter criterium based on the accuracy of the retrieved cloud properties takes the extinction derived by HERA into account. The extinction quality flag is reported for each cloud layer where an extinction coefficient was calculated by the CALIOP retrieval. This flag is a bit-mapped 16-bit integer and contains information about whether the extinction retrieval is constrained or unconstrained, and if the lidar ratio was reduced or increased. In Fig. 3.2 left a histogram of the ice optical thickness of the 5 km Cloud Layer Product shows a bimodal distribution. The right peak, at $\tau \sim 2.5$, appears to be an artefact due to the behaviour of the retrieval

algorithm, when the initial retrieval diverges and the lidar ratio is reduced in order to produce a convergent solution. In most cases this happens in totally attenuating, opaque clouds, and when the true cirrus lidar ratio is significantly smaller than the initial value assumed by the algorithm [Atmospheric Science Data Center, 2011]. If the lidar ratio is kept unchanged the extinction quality flag is equal zero representing the highest retrieval quality and the second peak disappears (Fig. 3.2right). In case of a constrained retrieval, changed lidar ratios, or any other retrieval issues the quality flag is reported with values greater equal one. This also illustrates a general limitation of lidar measurements. The absorption of an aerosol or cloud layer increases until the signal gets totally attenuated and CALIOP fails to penetrate through the specific layer. This behaviour is observed for optical thickness τ greater than 3 – 5, [Winker et al., 2010]. Since the main focus of the COCS algorithm is on thin cirrus clouds the maximum value of the ice optical thickness of a cirrus layer is limited to $\tau = 2.5$.

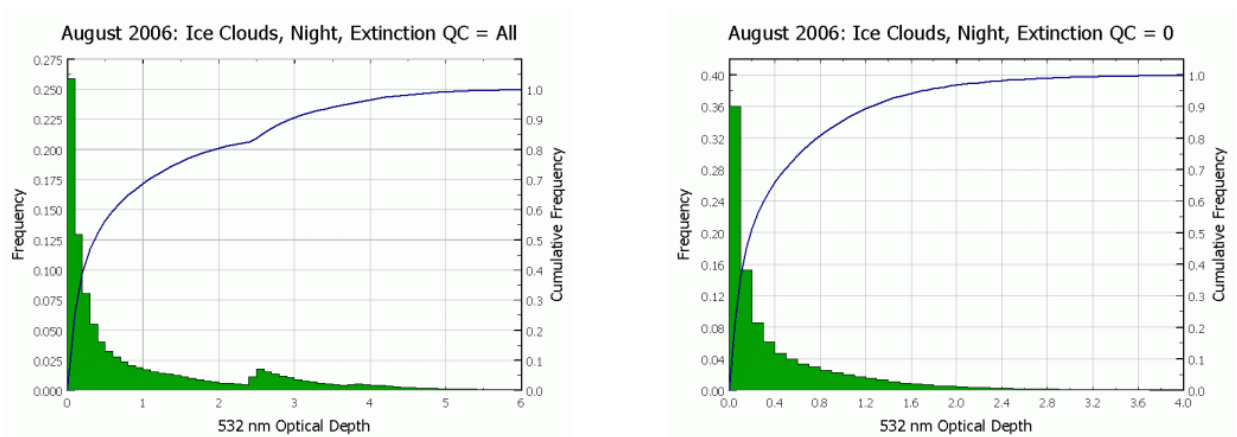


Figure 3.2: Histogram of ice optical thickness retrieved from CALIOP in August 2006 during night time [Atmospheric Science Data Center, 2011]. All extinction quality flags (left), only extinction quality flags equal zero (right).

3.1.2 SEVIRI data

A brief overview on the SEVIRI instrument and the algorithms to retrieve the equivalent brightness temperatures of the infrared channels is given in Section 2.2.2. Different studies on cirrus clouds have already proven the possibility to retrieve cirrus cloud coverage and cloud properties by using the equivalent brightness temperatures of the thermal infrared channels alone or in combination with the visible and short-wave infrared channels (Section 2.2.3. Since COCS shall be able to detect thin cirrus clouds during day and night time the thermal infrared channels of SEVIRI are used as input of the neural network. Hence, infrared brightness temperatures (BT) of the channels WV073, IR097, IR120, and

BT	BTD
WV073	WV062 - WV073
IR097	IR087 - IR120
IR120	IR108 - IR120
IR134	

Table 3.1: Brightness temperature (BT) and brightness temperature differences (BTD) utilized by the COCS algorithm.

IR134 are selected as well as the brightness temperature differences (BTD) of the channel combinations WV062 and WV073, IR087 and IR120, and IR108 and IR120 (Table 3.1). In order to support the error minimisation in the backpropagation neural network three BTD were chosen beside the four BT, since their sensitivity to cirrus cloud properties has been already used in several other retrieval algorithms (Section 2.2.3).

Fig. 3.3 and 3.4 aim to illustrate the signature of a cirrus cloud over the North Atlantic and are based on measurements taken by SEVIRI on 01 December 2010 at 12:00 UTC. This scene covers an area from 8° W to 34° W longitude and 34° N to 53° N latitude. As mentioned earlier (Section 2.2.2) atmospheric absorption is not uniform with altitude. Therefore each SEVIRI channel has a varying sensitivity to different atmospheric altitude levels (Fig. 2.8). The two water vapour channels, WV062 and WV073, show different brightness temperatures. WV073 (Fig. 3.3b) registers high temperature differences between warm water clouds at low altitudes and cold ice clouds at higher altitudes, while WV062 (Fig. 3.3a) shows lower contrasts between those different cloud type, due to its sensitivity to higher levels of the atmosphere. Both channels are located in the absorption bands of water vapour, where absorption occurs strongly at mid-tropospheric levels, so that radiances cannot penetrate through the higher absorbing water vapour. With the homogeneous water vapour background, the BTD of WV062-WV073 shows cirrus clouds with low values close to zero and higher values for water clouds reaching up to 20 K (Fig. 3.3c).

The discrimination of ice and water clouds is supported by the IR087 and IR120 channels (Fig. 3.3d, g) where again a BTD of both channels is used. The IR087 channel shows cirrus clouds with cold temperatures (lower than 260 K), while warm water clouds occur with higher temperatures up to 290 K. The IR120 channel detects slightly lower brightness temperatures for the cirrus cloud up to a difference of 7 K, while the lower water clouds are detected with similar temperatures. The BTD of the IR087 and the IR120 channel in Fig. 3.4a shows this differences, which are especially found for thin cirrus clouds.

The BT of the IR097 channels results in similar contrasts compared for example to the IR108 channel with a good contrast between high ice and low water clouds (Fig. 3.3e). With the so-called split window test, the BT of the IR108 and the IR120 channel (Fig. 3.3f,

3. COCS - Cirrus optical properties derived from CALIOP and SEVIRI during day and night

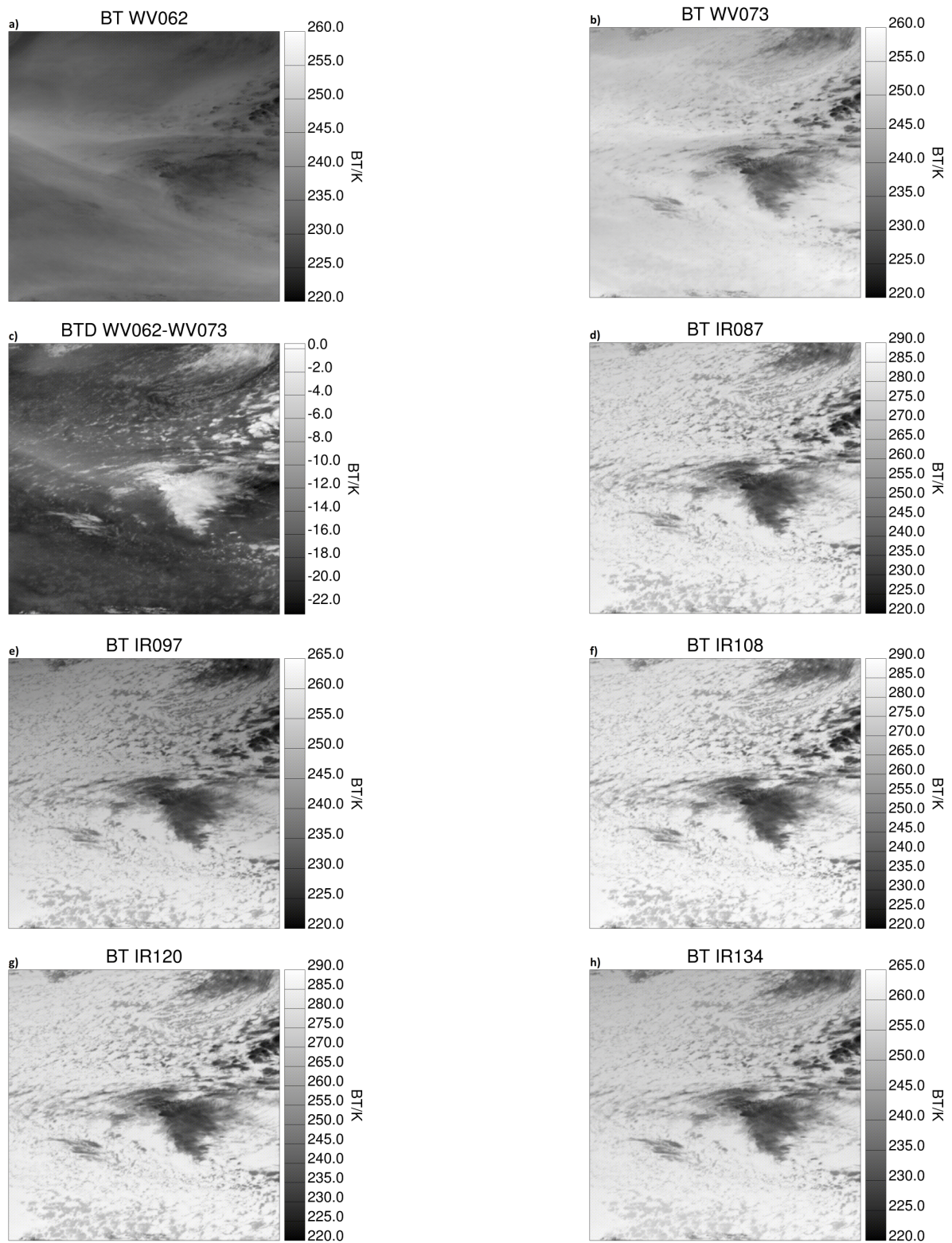


Figure 3.3: 01 December 2010 at 12:00 UTC covering an area from 8° W to 34° W longitude and 34° N to 53° N latitude: BT of (a) WV062, (b) WV073, (d) IR087, (e) IR097, (f) IR108, (g) IR120, (h) IR134, and the BTD of (c) WV062-WV073.

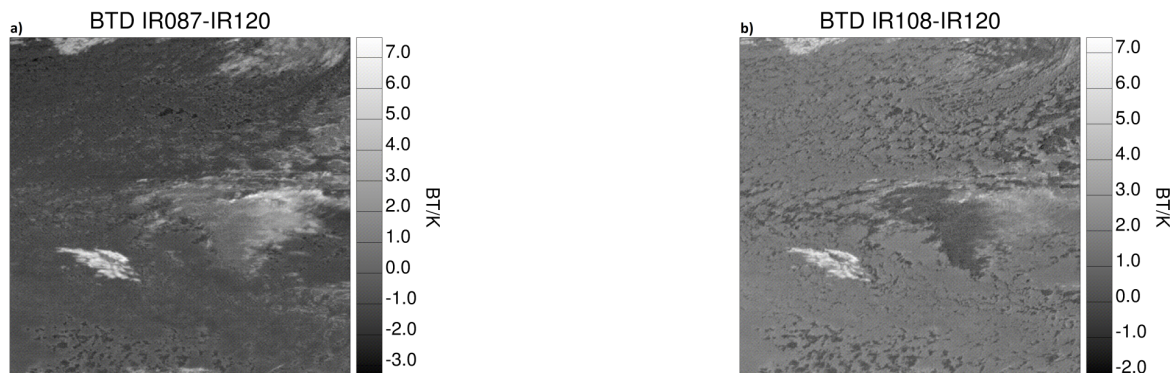


Figure 3.4: 01 December 2010 at 12:00 UTC covering an area from 8° W to 34° W longitude and 34° N to 53° N latitude: BTD of (a) IR087-IR120, and (b) IR108-IR120.

g), are taken into account. The calculated BT of the IR108 and the IR120 channel show differences for high clouds with higher temperatures of 7 K in case of IR108, whereas the temperatures for low clouds remain almost constant in both spectral intervals. These differences become evident in the BTD of both channels (Fig. 3.4b), which is highly sensitive to cirrus clouds with an ice optical thickness between 0.1 and 2.0 [Krebs et al., 2007], where thin cirrus clouds appear with high BTD signals. Channel IR134 finally supports the discrimination of ice clouds with low temperatures against the warm background of Earth’s surface and water clouds in low altitudes (Fig. 3.3h).

Furthermore, the BT and BTD also includes information on the particle size, which cannot be used in the COCS algorithm as it is not contained in the CALIOP cloud layer product version 2 [Wang et al., 2011].

3.1.3 Auxiliary data

In addition to CALIOP and SEVIRI data, COCS uses three auxiliary datasets, latitude, viewing zenith angle of SEVIRI, and a land-sea mask. The latitudes and the viewing zenith angles are mapped and matched to the SEVIRI-pixels. The viewing zenith angle gives the algorithm an information on the resolution of SEVIRI, which decreases with growing viewing zenith angle, while latitudes support COCS to determine the top altitude of cirrus clouds. The land-sea mask is based on a map with a $0.5'$ resolution in latitude and longitude (≈ 0.2 km) constructed by the Group for High Resolution Sea Surface Temperature [Kaiser-Weiss, 2011], and covers latitudes from 80° N to 80° S. The information on whether the surface consists of water or land is important for the infrared channels in order, since in case of cloud-free atmosphere the thermal infrared channels of SEVIRI reach down to Earth’s surface and detect different temperatures for example for warm water and colder land surface. As this map has a much higher resolution than SEVIRI, the mapped SEVIRI land-sea mask contains values of zero for sea and water,

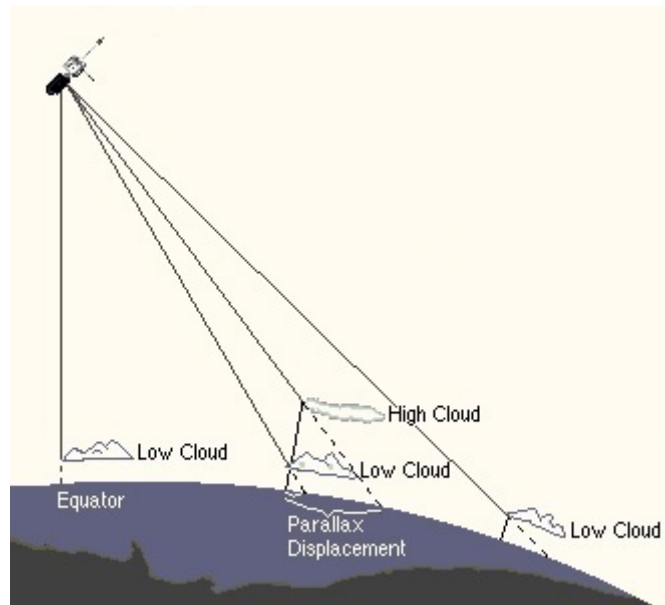


Figure 3.5: Illustration of the parallax displacement. High clouds are displaced further than low clouds [Geerts, 1999].

one for land surface, and fractions for coastal lines, lake shores, and riversides in some pixels.

3.2 Collocation and Parallax-Correction

For the overpasses of CALIPSO the data of CALIOP and SEVIRI are spatially and temporally collocated. Collocation in time and space is necessary in order to guarantee that both satellite instruments observe the same cloud at the same time. The time of each atmospheric profile in the 5 km Cloud Layer product of CALIOP is compared to the imaging time of SEVIRI and the closest time slot of SEVIRI is chosen to minimise the temporal deviation. As SEVIRI has a repeat cycle of 15 min a maximum difference of approximately 7.5 min remains. For a geostationary satellite such as MSG, it is a straightforward geometric exercise to calculate sensor resolution, sampling frequencies, and viewing angles relative to Earth's surface. As the radiometer scans away from the subsatellite point, the effective resolution of SEVIRI data is decreased due to the curvature of the Earth and the increasing distance to the satellite. Therefore the cloud is detected by SEVIRI with a so-called parallax displacement (Fig. 3.5). Depending on the viewing zenith angle and on the altitude of the cloud, its displacement compared to its correct position "over ground" can be calculated by using latitude, longitude, and the top altitude of the cirrus layer. Latitude and longitude of CALIOP are directly translated to the SEVIRI-pixel grid, while the cirrus top altitude is directly measured by CALIOP. With

this information on the position of a cirrus cloud, the parallax displacement is corrected and the exact SEVIRI pixel is chosen for the cirrus cloud detected by CALIOP. A similar derivation of the parallax displacement is done in Radová and Seidl [2008].

3.3 Training the neural network

Before the training of the backpropagation neural network is initialized the final setup of COCS needs to be determined (Section 2.4.4).

According to the schematic setup of a neural network in Fig. 2.14, ten neurons in the input layer (SEVIRI and auxiliary data) and two neurons in the output layer (cirrus ice optical thickness and top altitude) are set by the input and output dataset. The number of hidden neurons was chosen by considering two properties of the neural network. On the one hand, more hidden layer neurons generate more accurate results. On the other hand, neural networks with less neurons perform faster. Since the final algorithm shall be able to perform as fast as possible in combination with sufficient accuracy, 600 neurons for the hidden layer are found by testing different setups to be good trade-off. This leads to 6000 connection weights between input and hidden layer and 1200 weights between hidden and output layer.

The training of COCS follows the same steps described in Section 2.4.4 and the training dataset is presented to the network in random order until no change in the performance expressed by the sum of the quadratic deviations is observed. This error was minimized until no further improvement in the results was achieved reaching a standard deviation of $\sigma_\tau^2 = 0.3$ and $\sigma_z^2 = 0.8$ km for both neural networks, COCS period 1 and COCS period 2. These deviations are further analysed in Section 4.1.1.

3.4 COCS examples

Once the training is finished, COCS is applied to SEVIRI measurements. With the high temporal resolution of 15 minutes and the good spatial resolution of up to 3 km x 3 km at subsatellite point, COCS covers almost one third of Earth's surface from 80° N to 80° S and from 80° W to 80° E and is now able to detect thin cirrus clouds and to determine their optical thickness τ and top altitude z with the heritage of high accuracy and sensitivity of CALIOP. For each 15 minute timeslot of SEVIRI with 3712 x 3712 pixels the processing of τ and z takes around 500 seconds on a common office desktop computer including the preparation of the input data. The retrieved data are stored as byte arrays in order to save disc space. In the false colour composite of SEVIRI (Fig. 3.6) three different channels (VIS006, VIS008, IR108) are combined to give an overview of several atmospheric features on the 11 September 2010 at 15:00 UTC. Water clouds are coloured in light yellow and



Figure 3.6: False colour composite of SEVIRI (VIS006, VIS008, IR108) at 15:00 UTC on the 11 September 2010.

grey, while ice clouds appear in white and light blue/violet.

The belt of the Inertropical Convergence Zone (ITCZ) is covered by a relatively high amount of cirrus clouds, while the northern and southern parts of the African continent show only small amounts of cirrus clouds. Two tropical cloud clusters, which might be remains of a tropical cyclone, are detected over the Atlantic west of Africa and in the Caribbean Sea. Another tropical storm is located north of Madagascar, which is not clearly visible due to the sunset at the eastern limits of the MSG disc. South west of Africa maritime stratocumulus clouds cover wide areas. The very south of the Atlantic is strongly covered with cirrus clouds, while the Atlantic north of the Equator shows water and ice clouds. Frontal systems over Europe and the North Atlantic are distinguishable.

In Fig. 3.7 and 3.8 the results of COCS, τ_{COCS} and z_{COCS} , are shown for the same time slot with coastlines for a better orientation. The cirrus clouds described above can all be identified on these images. The ITCZ, the tropical cyclone, and even the frontal systems show up with varying and inhomogeneous τ_{COCS} and z_{COCS} . It is remarkable that both variables show no influence of whether the background is sea or land and succeed in detecting ice clouds, while the algorithm ignores water clouds like the maritime stratocumulus clouds west of Namibia and Angola. Especially the large cirrus cloud field south of Greenland in the Northern Atlantic is noteworthy. The North Atlantic Region and parts of Europe are enlarged in Fig. 3.9 and 3.10 for again the same timeslot. A large cirrus cloud field, mentioned above, reaches from the coast of the United States almost to the South of Iceland. Obviously fine structures of the cirrus clouds are present with top altitudes from 8 to 13 km and optical thickness from 0.1 to 2.3. Additionally the center of a low-pressure area can be found North of England together with small amounts of cirrus clouds over Morocco. The images in Fig. 3.7 to 3.10 aim to show an example of the application of COCS and to give an idea on the resolution it provides. As one can see different structures of cirrus clouds are found in different regions of the MSG disc containing clouds with highly variable ice optical thickness and top altitude.

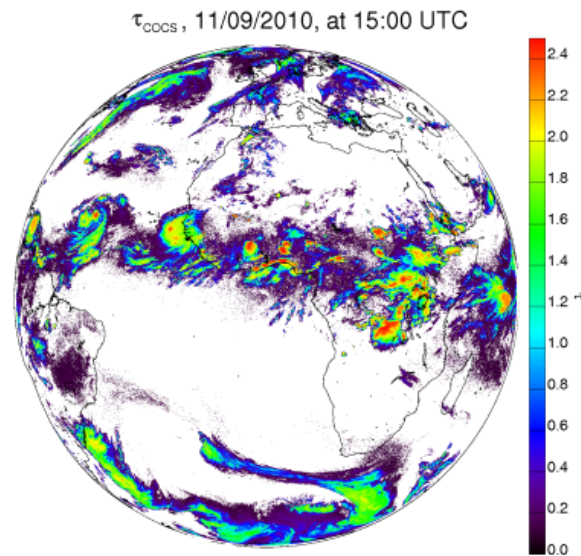


Figure 3.7: 11 September 2010 at 15:00 UTC: Ice optical thickness τ of cirrus clouds calculated by COCS. Coast lines are coloured black.

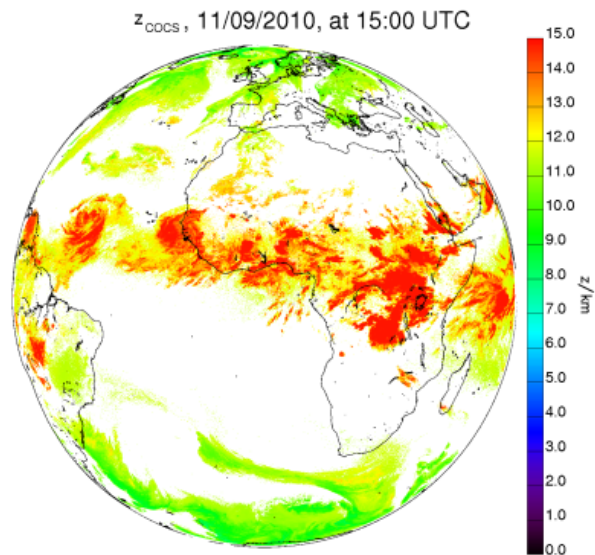


Figure 3.8: 11 September 2010 at 15:00 UTC: Top altitude z of cirrus clouds calculated by COCS. Coast lines are coloured black.

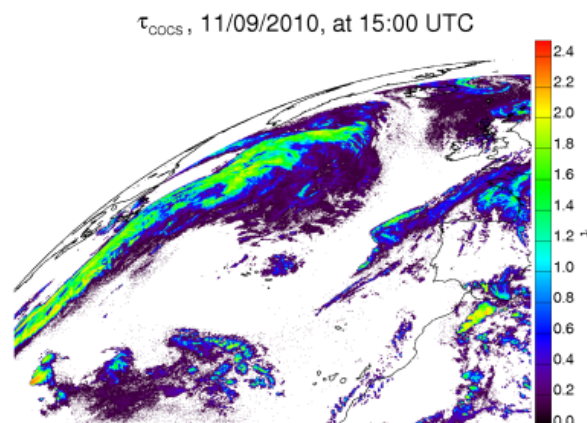


Figure 3.9: 11 September 2010 at 15:00 UTC: Enlarged view on the North Atlantic Region of ice optical thickness τ calculated by COCS. Coast lines are coloured black.

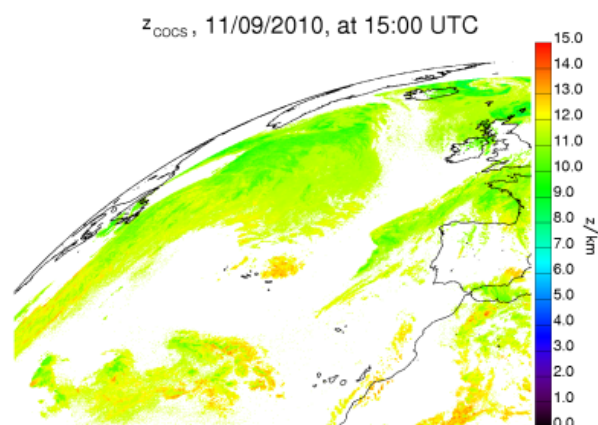


Figure 3.10: 11 September 2010 at 15:00 UTC: Enlarged view on the North Atlantic Region of top altitude z calculated by COCS. Coast lines are coloured black.

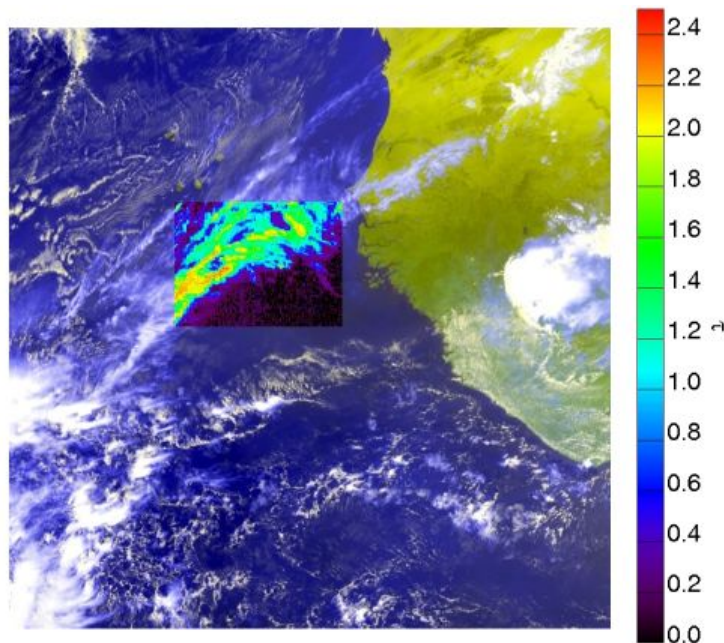


Figure 3.11: False color composite derived from SEVIRI on the 12 May 2010 at 12:00 UTC. The scene is located West of Africa with the Canarian Islands in the upper third. A cirrus cloud over homogeneous background of the Atlantic Ocean is analysed by COCS, the derived ice optical thickness is depicted here for an area of 220×170 pixels.

3.5 Physical background

After first results of τ_{COCS} and z_{COCS} were shown in Section 3.4, this section aims at showing the connection between the derived variables and the different infrared brightness temperatures (BT) and brightness temperature differences (BTD) respectively (Section 2.2.3).

A typical cirrus scene is depicted in Fig. 3.11. The false color composite, derived from SEVIRI on the 12 May 2010 at 12:00 UTC, shows a scene of cirrus and water clouds located west of Africa with the Canarian Islands in the upper third. Wide areas are covered with tropical cirrus clouds, coloured in blueish/white colors and some lower liquid water clouds (greyish/yellowish color). The results of τ_{COCS} derived for a limited amount of ~ 4000 pixels in this scene is plotted with values of $0.1 \leq \tau_{COCS} \leq 2.3$ over the homogeneous background of the tropical Atlantic Ocean. Fig. 3.12 left and right depict the mean values of the four infrared BT and the three infrared BTD used by COCS as a function of τ_{COCS} for bins of $\Delta\tau = 0.05$, while Fig. 3.14 left and right show the dependency on z_{COCS} in bins of $\Delta z = 0.1$ for the altitude range of these cirrus clouds of $11.9 \text{ km} \leq z_{COCS} \leq 16.5 \text{ km}$. For the intervals of τ_{COCS} and z_{COCS} the mean BT and BTD is depicted for the analysed part of the cirrus cloud in Fig. 3.11.

The error bars in Fig. 3.12 and 3.14 represent the standard deviations of brightness tem-

peratures and brightness temperature differences used in order to calculate the interval mean values. Fig. 3.12 left shows that the four thermal infrared BT of the channels IR073, IR097, IR120, and IR134 decrease for growing ice optical thickness, and reach their minimum temperature for the maximum ice optical thickness of the cloud at around $\tau_{COCS} = 2.3$. In case of semi-transparent cirrus clouds with low optical thickness “warm” atmospheric layers and the Earth’s surface below the cirrus cloud contribute highly to the BT measured by SEVIRI. In opposition opaque clouds absorb these parts of the measured radiances and therefore lead to colder brightness temperatures. For pixels with low τ_{COCS} the four BT differ by ~ 30 K, but for thick cirrus clouds only small differences of ~ 10 K are detected within all channels. The standard deviations for all four channels is small for the whole range of τ_{COCS} with values of only 1 – 2 K. The BTD IR087-IR120 and IR108-IR120 (Fig. 3.12 right) are found to form small differences of 2 K and 0.5 K for thin cirrus clouds. These BTDs increase for cirrus clouds with higher optical thickness, and decrease for cirrus clouds with $\tau_{COCS} > 1.5$. Especially the split-window test (BTD IR108-IR120) has been used in the past to detect thin cirrus clouds [Inoue, 1985] due to the different absorption behaviour of ice particles in the different wavelength, but it is less sensitive to opaque cirrus clouds, which absorb radiation as mentioned above. A similar behaviour is seen for the BTD IR087-IR120. The BTD of the two water vapour channels WV062-WV073 has high negative differences for low optical thickness of up to -22 K. With growing ice optical thick this BTD increase to values of almost zero. This BTD is on the one hand sensitive to the optical thickness of cirrus clouds in general, on the other hand information on the cirrus clouds altitude is contained in this BTD as well [Krebs et al., 2007]. Especially for cirrus clouds with $\tau_{COCS} \geq 1.0$ the standard deviation of the BTD IR087-IR120 increase up to 2 K, while for the other BTDs only small standard deviations up to 1 K are calculated.

The relationship of cirrus optical thickness and different brightness temperatures and brightness temperature differences is once more depicted in Fig. 3.13, where other than in Fig. 3.12 the x-axis is linear. Again, each BT shows decreasing values for growing optical thickness, Fig. 3.13 left, while the different dependencies of the BTDs are shown in Fig. 3.13 right. Especially due to the strong decay in the brightness temperatures for low cirrus optical thicknesses, Fig. 3.13 left, even thin cirrus clouds can be detected by the COCS algorithm. For cirrus clouds with higher optical thickness the plotted curves are expected to have an asymptotic approach to low brightness temperatures, which is suggested by the BT-curves for $\tau_{COCS} \geq 1.9$.

Beside their dependency on the optical properties (optical thickness, effective radius, etc.) of cirrus clouds, the thermal infrared channels contain also information on the top altitude of the cirrus clouds. Figure 3.14 left shows the dependency of the BT on the top altitude of the cirrus cloud. With increasing z_{COCS} the brightness temperatures decrease until a value of $z_{COCS} > 15.5$ km is reached. For higher altitudes the temperatures increase

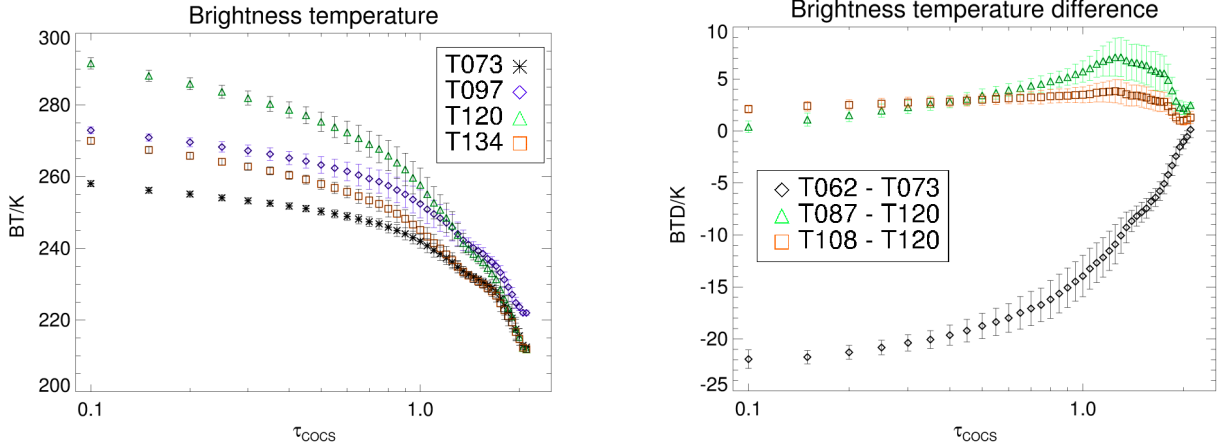


Figure 3.12: Brightness temperatures (left) and brightness temperature differences (right) depicted as a function of cirrus optical thickness τ_{COCS} derived by COCS. The errorbars represent the standard deviation.

again. Hence, the brightness temperatures alone are not sufficient to retrieve the correct cirrus top altitude as well as it is the case for the cirrus ice optical thickness, which shows the difficulty in the retrieval of accurate top altitudes of cirrus clouds with passive remote sensing. While the altitude derivation of opaque cirrus clouds shows an almost linear decrease in the BTs with growing z_{COCS} depending on e.g. the vertical profile of temperature and moisture, semi-transparent clouds are detected at $z_{COCS} > 15.5$ km with increasing BTs due to the contribution of Earth's surface and the atmosphere below the clouds. The standard deviations for each brightness temperature used to derive the cirrus top altitude show variations of up to 10 K in the single channels, while the standard variations of especially two BTD in Fig. 3.14 right, the BTDs of IR087-IR120 and IR108-IR120, have very small values. This suggests, that especially the two BTDs, IR087-IR120 and IR108-IR120, are the main contributors to the exact determination for z_{COCS} in the whole altitude range. These two BTDs show an almost linear increase with altitude. The BTD of the two water vapour channels shows high standard deviations. Especially at cirrus top altitudes greater than 15.5 km an increase in the BTD of WV062-WV073 is observed similar to the BTs (Fig. 3.14 left).

These different BTs and BTDs (Fig. 3.12 to 3.14) enable the COCS algorithm to separate between cirrus/ice and water clouds and to retrieve their properties even in case of thin cirrus clouds. Especially in case of the top altitude, but also for the retrieval of cirrus optical thickness, Fig. 3.12 to 3.14 aim to illustrate, that the use of only one BT or BTD would be ambiguous, since especially in case of the cirrus top altitude single BTs or BTDs can hardly be assigned to one top altitude. Therefore, the neural network combines the different dependencies and relationships of all BTs and BTDs with the desired output during its training to detect cirrus clouds and to retrieve their optical properties in one step unlikely previous algorithms, which first had to detect a cirrus cloud before retrieving

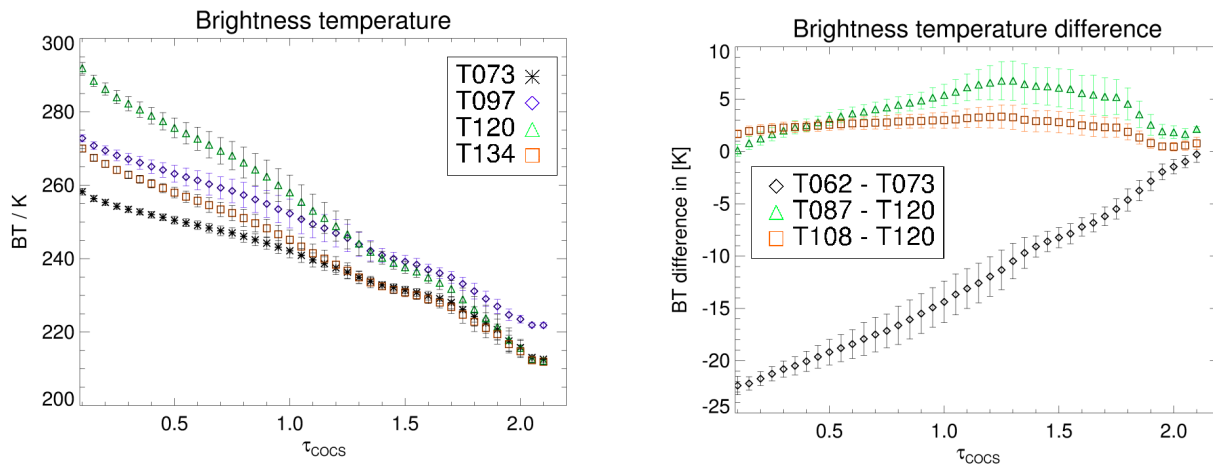


Figure 3.13: Similar to Fig. 3.12: Brightness temperatures (left) and brightness temperature differences (right) depicted as a function of cirrus optical thickness τ_{COCS} derived by COCS, but here with linear x-axis. The errorbars represent the standard deviation.

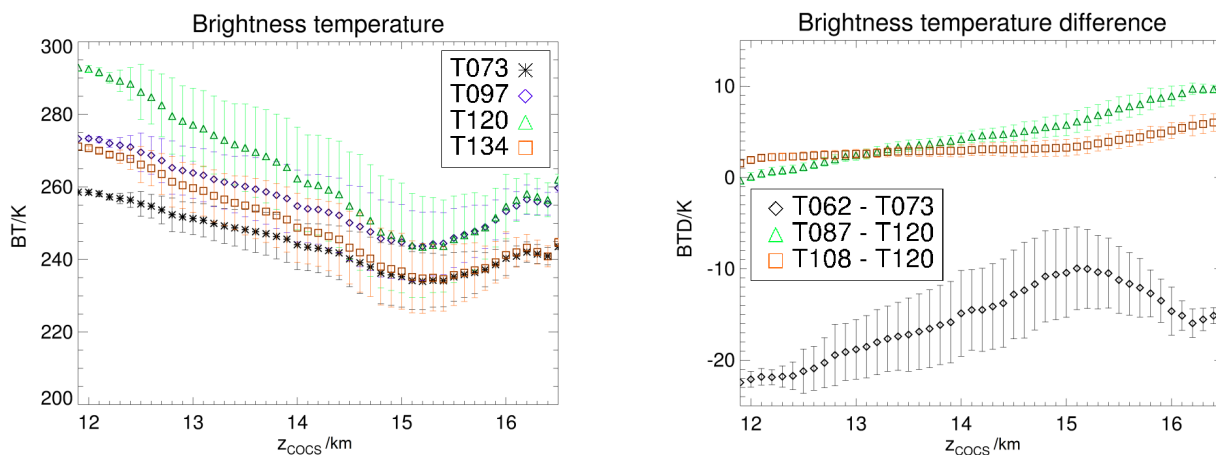


Figure 3.14: Brightness temperatures (left) and brightness temperature differences (right) depicted as a function of the cirrus top altitude z_{COCS} derived by COCS. The errorbars represent the standard deviation.

its optical properties. In particular this difference results in a very fast runtime of the COCS algorithm of around 500 s for each MSG disc.

Another advantage of COCS is mentioned in Ostler [2011], when semi-transparent cirrus clouds are located above water clouds. COCS succeeds in separating those cirrus clouds and deriving their properties even in those difficult situation. This capability is caused by the dataset derived by CALIOP, where a general separation of ice and water clouds is guaranteed by the filter criteria applied to the Cloud Layer products (Section 3.1.1). Due to the applied altitude- and temperature-dependent thresholds the neural network can be trained to only detect cirrus clouds above a specific altitude. Therefore the training dataset contains four classes of atmospheric situations: Only high cirrus clouds, cirrus clouds above layer(s) of water clouds, water clouds, and absolutely cloud-free situations. As described, these measurements are collocated and combined to the BTs and BTDs measured by SEVIRI, which are dependent on altitude (Fig. 2.8). Especially the water vapour channels WV062 and WV073 have their maximum contribution to the brightness temperatures at relatively high altitude (roughly above 6 km) with almost no contribution of low atmospheric layers (Section 2.2.3), since radiation from low atmospheric layers and Earth's surface is absorbed by the high concentration of moisture already in low altitudes.

Chapter 4

Validation and Comparison

As mentioned, the dataset of collocated CALIOP and SEVIRI measurements was split into a training and a test dataset for both neural networks, period 1 is used for the time before April 2008 and period 2 starting with May 2008.

In order to retrieve information about sensitivity and accuracy of the COCS algorithm a validation with the test dataset of CALIOP is shown in this section as well as a validation with an airborne High Spectral Resolution Lidar (HSRL) measuring thin cirrus clouds during a field campaign in 2008. Additionally, comparisons with the Meteosat Cirrus Detection Algorithm 2 (MeCiDA-2) and the Algorithm for the Physical Investigation of Clouds with SEVIRI (APICS), which calculates inter alia optical thickness of ice and water clouds during day time, are presented. Finally, error and bias of COCS are calculated.

4.1 Validation with Lidar measurements

4.1.1 Spaceborne lidar data

As mentioned in Section 3.1 the dataset of combined CALIOP (cirrus ice optical thickness τ and top altitude z) and SEVIRI measurements (brightness temperatures and brightness temperature differences) covers a period from July 2006 to June 2009: COCS period 1 and COCS period 2.

In order to test the good performance of the COCS algorithm, one ninth of the datasets is separated and has therefore no influence on the training of COCS. This independent test dataset will be used for the initial validation with CALIOP in the following. Fig. 4.1 represents the quality of cirrus optical thickness measurements τ_{COCS} compared to the CALIOP measurements τ_{CALIOP} shown as a two dimensional histogram with logarithmic scale. COCS period 1 on the left shows an overall good performance. However, COCS period 1 tends to underestimate the ice optical thickness for $\tau_{\text{CALIOP}} > 1.7$, while for $\tau_{\text{COCS}} \leq 1.0$ a slight overestimation of the ice optical thickness measured by CALIOP is

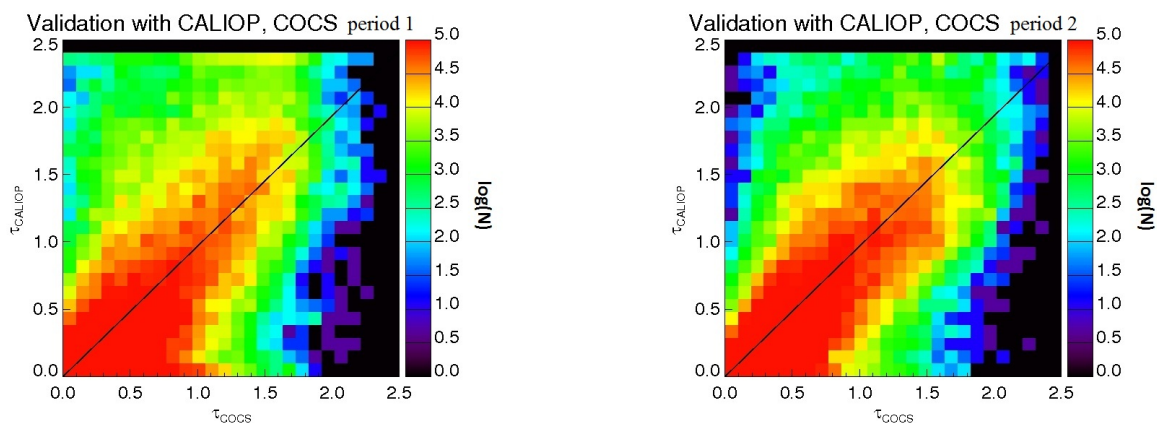


Figure 4.1: Scatter plot of the ice optical thickness τ of CALIOP and COCS: period 1 (left) and period 2 (right). Colours show the number of occurrences on a logarithmic scale.

present. COCS period 2 on the right results in an even higher accuracy, which is caused by EUMETSAT's new definition of measured radiances in order to retrieve brightness temperatures, Section 3.1. For low values a high agreement of τ_{CALIOP} and τ_{COCS} is found. For $\tau_{\text{CALIOP}} \leq 2.0$ only low deviations are found. The tendency to underestimate high values of τ_{CALIOP} is lower in COCS period 2 compared to period 1.

For both periods, the standard deviation of τ , σ_τ , calculated as

$$\sigma_\tau = \sqrt{\frac{1}{N} \sum_{i=1}^N (\tau_{\text{COCS},i} - \tau_{\text{CALIOP},i})^2}, \quad (4.1)$$

with N is the number of compared observations, results in 0.25 for period 1, and 0.24 for period 2.

The validation of the second cirrus property retrieved by COCS, the cirrus top altitude z_{COCS} , is shown in Fig. 4.2. Again, COCS period 1 (left) and COCS period 2 (right) are compared to the result of CALIOP, z_{CALIOP} . In COCS period 1 the z_{COCS} is derived in a good correspondence to z_{CALIOP} . For altitudes z_{CALIOP} between 10 and 15 km a high agreement between COCS and CALIOP is detected, while for low altitudes COCS overestimates the top altitude. For $z_{\text{CALIOP}} > 15$ km a slight underestimation of the cirrus top altitude is found.

COCS period 2 differs only slightly from COCS period 1. A very good agreement is observed again for altitude ranges from 10 to 15 km. For $z_{\text{CALIOP}} > 15$ km COCS underestimates high cirrus clouds, while low top altitudes are overestimated. The standard deviation σ_z of the cirrus top altitude for both periods is $\sigma_{z_{p1}} = 708$ m for period 1 and $\sigma_{z_{p2}} = 756$ m for period 2.

One reason for the resulting standard deviation of cirrus optical thickness and top al-

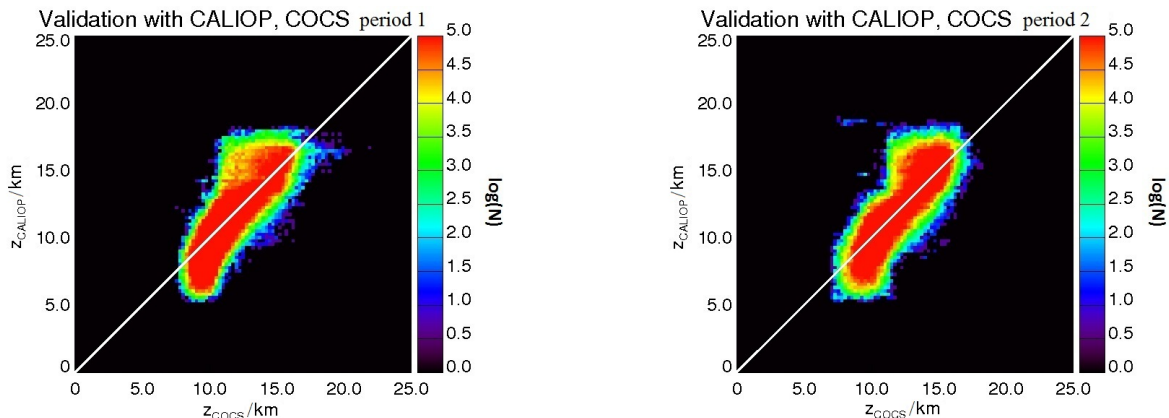


Figure 4.2: Scatter plot of the cirrus top altitude in km of CALIOP and COCS: Period 1 (left) and period 2 (right). Colours show the number of occurrences on a logarithmic scale.

titude is caused by the different resolution of both instruments. As already mentioned in Section 2.3.2, the cloud layer product of CALIOP used in this work has a horizontal resolution of 5 km, while the cross section of the lidar footprint is narrow with only 90 m. Each 5 km in this cloud layer product is achieved by averaging 15 single profiles. These profiles are depicted as yellow circles in Fig. 4.3. As a red parallelogram the size of one SEVIRI pixel of around 3 km x 3 km is marked. While one SEVIRI pixel covers at least an area of 9 km² at subsatellite point, CALIOPs 5 km cloud layer product only “cuts” through a small part of the cloud within one SEVIRI pixel. The sampling area of one SEVIRI pixel is even greater, depicted in blueish color. In case of broken clouds within the sampling area (which is used in the processing of SEVIRI data to reduce radiometric noise) of one SEVIRI pixel it is possible on the one hand, that CALIOP either misses to retrieve the correct cirrus optical thickness and top altitude, or even misses to detect the cirrus cloud. On the other hand, inhomogeneous and probably thin cirrus clouds, which are located within the SEVIRI pixel / sampling area and detected by CALIOP, might not result in brightness temperatures detected by SEVIRI lower than those of the atmosphere below. Another reason for the different performance of COCS period 1 and period 2 is the change in the EUMETSATs retrieval of spectral to effective radiances, as already mentioned in Section 3. Two further characteristics of the algorithm are investigated for a final assessment of the sensitivity of COCS. The first property is the detection efficiency, $eff_{det}(\tau)$, which is determined for equidistant intervals of ice optical thickness τ , $\Delta\tau = 0.01$. Please be aware that $\tau = \tau_{CALIOP}$:

$$eff_{det}(\tau) = \frac{N_{COCS}(\tau)}{N_{CALIOP}(\tau)} \cdot 100 \% , \quad (4.2)$$



Figure 4.3: Schematic intercomparison of CALIOP single profile footprints (yellow circles) and SEVIRI pixels (red parallelograms). In blueish color the sampling area of one SEVIRI pixel is sketched. Please note, that this is an exemplary plot to represent the different scales.

with $N_{COCS}(\tau)$ is the number of pixels where COCS detects a cirrus cloud, and $N_{CALIOP}(\tau)$ the number of pixels with a cirrus cloud detected by CALIOP. The second important property, the false alarm rate $far(\tau_{COCS})$, describes the rate of false detections of COCS again for the same equidistant intervals of $\Delta\tau = 0.01$. This false alarm rate shows how many false alarms contribute to each interval of optical thickness. It is calculated as:

$$far(\tau) = \frac{N_F(\tau)}{N_H(\tau) + N_F(\tau)} \cdot 100 \% , \quad (4.3)$$

with $N_F(\tau)$ representing the number of pixels where COCS detects a cirrus cloud, while CALIOP detects no cirrus cloud. $N_H(\tau)$ is the number of pixel where both, COCS and CALIOP detect a cirrus cloud. The subscripts H and F are the abbreviations for *Hits* and *Falsealarms* respectively.

In Fig. 4.4 the detection efficiencies (blue) of COCS, COCS period 1 (left) and period 2 (right), are depicted for the equidistant interval of $\Delta\tau = 0.01$. The detection efficiency is found to show very high efficiencies of $eff_{det} > 95 \%$ for $\tau = 0.01$, raising up to $eff_{det} = 100 \%$.

The false alarm rates far of COCS period 1 and period 2 show different behaviours. Both neural networks start with relatively high rates up to $\sim 25 \%$ for the false alarms at $\tau < 0.1$, but show a rapid decrease in the far in combination with high detection efficiencies at $\tau \geq 0.1$. Therefore, a threshold of $\tau_{COCS} \geq 0.1$ is selected to provide a very high detection efficiency of 97.41 % for period 1 and 99.34 % for period 2 in combination

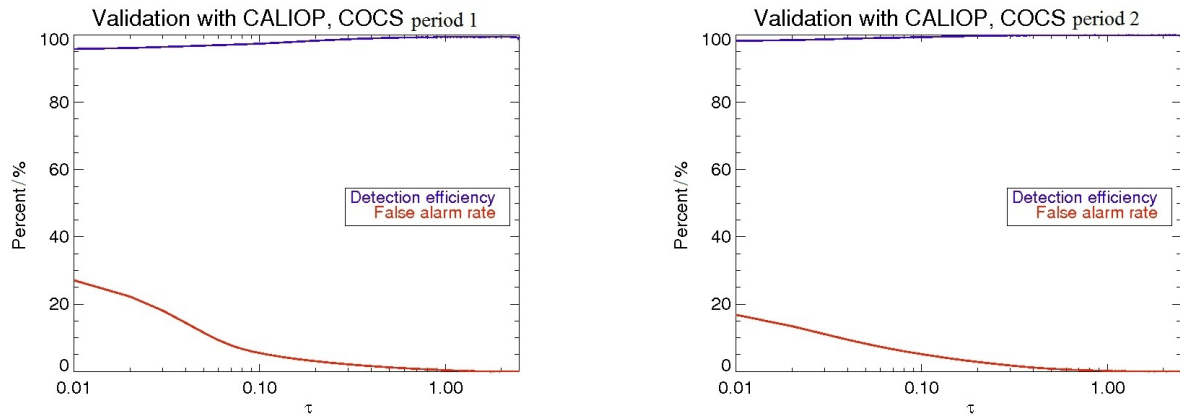


Figure 4.4: Detection efficiency eff_{det} (blue) and false alarm rate far (red) for COCS compared with CALIOP. COCS period 1 (left), COCS period 2 (right).

with a low false alarm rate of 5.05 % and 4.80 % respectively.

	period 1	period 2
$eff_{det}(\tau = 0.1)$	97.4071 %	99.3401 %
$far(\tau = 0.1)$	5.05230 %	4.80072 %

4.1.2 Airborne High Spectral Resolution Lidar data

In addition to the validation with CALIPSO, airborne lidar measurements during a flight of the DLR-project “PAZI” (Particles and Cirrus Clouds) in autumn 2008 are compared to the results of COCS. A more detailed validation of different passive remote sensing algorithms exploiting this dataset including the COCS algorithm is shown in [Ostler, 2011].

4.1.2.1 PAZI Campaign

In this section data, e.g. cirrus ice optical thicknesses, derived from the airborne High Spectral Resolution Lidar (HSRL) of the German Aerospace Center (DLR) are used. These data were measured during a flight within the DLR-project “PAZI” in autumn 2008, where amongst other things optical properties of thin cirrus and contrail cirrus clouds were measured. The aim of the PAZI project at DLR was to better understand the formation of the ice phase in cirrus clouds from natural and anthropogenic aerosols and to improve microphysical and optical parameterizations of cirrus clouds in global models.

In the following, results of Ostler [2011] are discussed and used for the validation of COCS, which focusses on one specific flight on 18 October 2011. The scientific research aircraft of the DLR, the Dassault Falcon, started at around 13:00 UTC at DLR, Oberpfaffenhofen

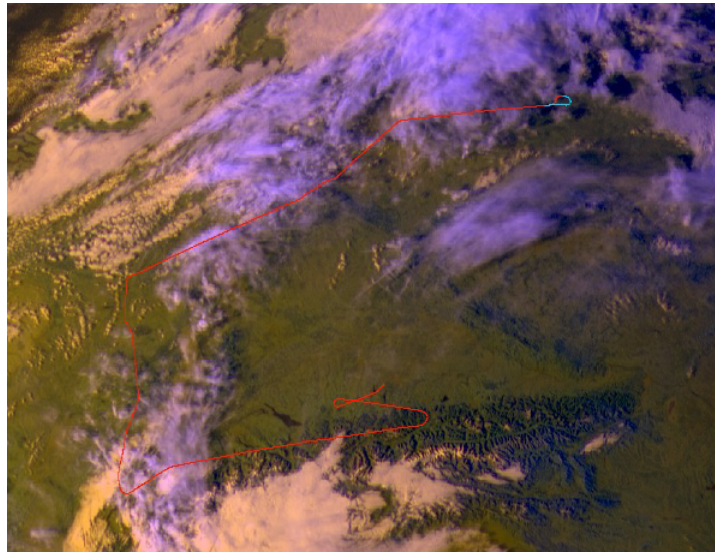


Figure 4.5: Flight route of the FALCON aircraft carrying the HSRL during the DLR-project “PaZi” on the 18 October 2010. The route sketched on a false colour composite of SEVIRI measured at 14:50 UTC [Ostler, 2011].

routing along the Alps, turning North along the Rhine valley, and finally heading East across Germany to Lindenberg. At 16:00 UTC the aircraft returned to Oberpfaffenhofen. A part of the flight path is shown in Fig. 4.5 as a false colour composite containing information from the VIS006, IR108 and the HRV channel. High cirrus clouds are coloured in light blue / violet, while lower water clouds are coloured in light yellow.

4.1.2.2 High Spectral Resolution Lidar

The HSRL is a lidar (Section 2.3.1) that works similarly to CALIPSO (Section 2.3.2) with one big advantage: It calculates the atmospheric extinction and backscatter coefficients without assuming the lidar ratio (Section 2.3.2, Eq. 2.54). The atmospheric backscatter signal, containing molecular and particulate scattering, is separated in two different receiver channels [Esselborn, 2008]. In one channel particulate scattering is suppressed by a iodine vapour filter and therefore measuring almost pure molecular scattering. The second channel measures both molecular and particulate scattering. Thus, this type of lidar is able to directly measure the optical thickness of e.g. a cirrus cloud.

4.1.2.3 Validation with HSRL

In order to validate the results of COCS, the different spatial and temporal resolutions of the HSRL and the SEVIRI data have to be accounted for. The HSRL provides ice optical thickness at a 1 s temporal resolution, which is equivalent to a distance of 200 m assuming the speed of the Falcon aircraft of 720 km/h with a very narrow footprint of

2 m. The SEVIRI pixels cover around 4 km x 5 km at mid-latitudes. Due to the high temporal and spatial resolution of the HSRL two points are important:

- 1) The georeferenced position of the Falcon is used to identify the geographic location of the clouds. The cloud top height is extracted from the HSRL profiles and is used for parallax correction and collocation (see Section 3.2).
- 2) The Rapid Scan Mode of SEVIRI is used by COCS.

Thus, the SEVIRI pixel closest to the Falcon track show a maximum temporal misregistration of 2.5 minutes. The HSRL cirrus ice optical thickness τ_{HSRL} for the SEVIRI pixels along the flight path is then calculated as the mean value of all HSRL measurements inside those pixels. Finally, 394 SEVIRI pixels can be used for the calculation of the detection efficiency eff_{det} and the false alarm rate far of COCS. The detection efficiency of COCS is depicted as a function of τ_{HSRL} in Fig. 4.7. At $\tau_{HSRL} = 0.2$ COCS detects 80 % of the cirrus clouds and eff_{det} increases for higher values of τ_{HSRL} . For $\tau_{HSRL} = 0.1$ already 50 % of the cirrus clouds are detected by both, the HSRL and COCS. The false alarm rate amounts to 2.6 %. Finally, τ_{COCS} is plotted against τ_{HSRL} in Fig. 4.6. The accordance for values of $\tau \leq 1.0$ is very good. Only for a few pixels with higher values measured by the HSRL some underestimation by COCS is shown. The slope of the regression line is calculated to be $r^2 = 0.71$ and is influenced by the outliers with $\tau_{HSRL} > 1$. In combination with the low false alarm rate, the high sensitivity of COCS makes this algorithm capable of detecting even thin cirrus clouds.

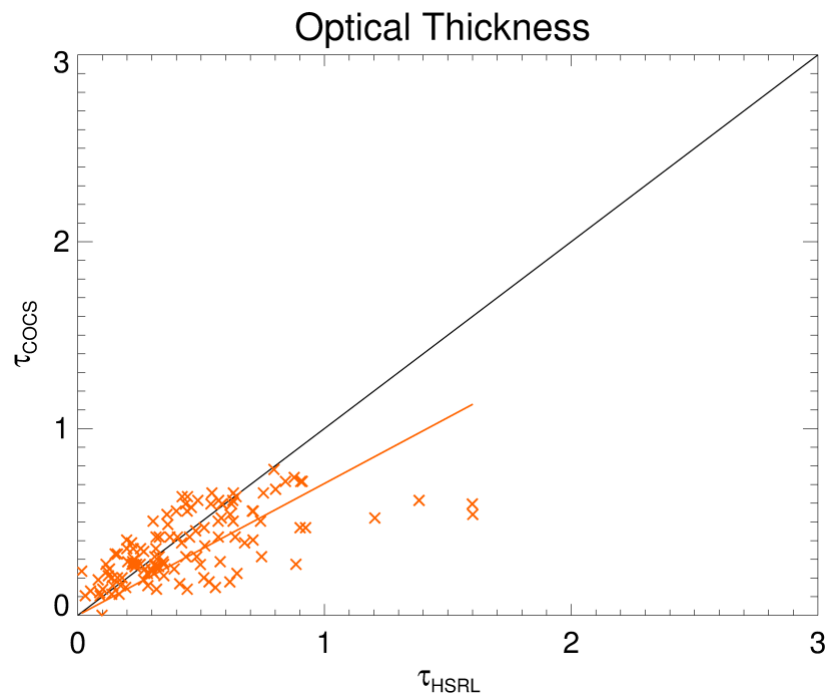


Figure 4.6: Intercomparison of cirrus ice optical thickness measured by HSRL and COCS during the FALCON flight, 18 October 2008. The correlation coefficient is calculated to be $r^2 = 0.71$.

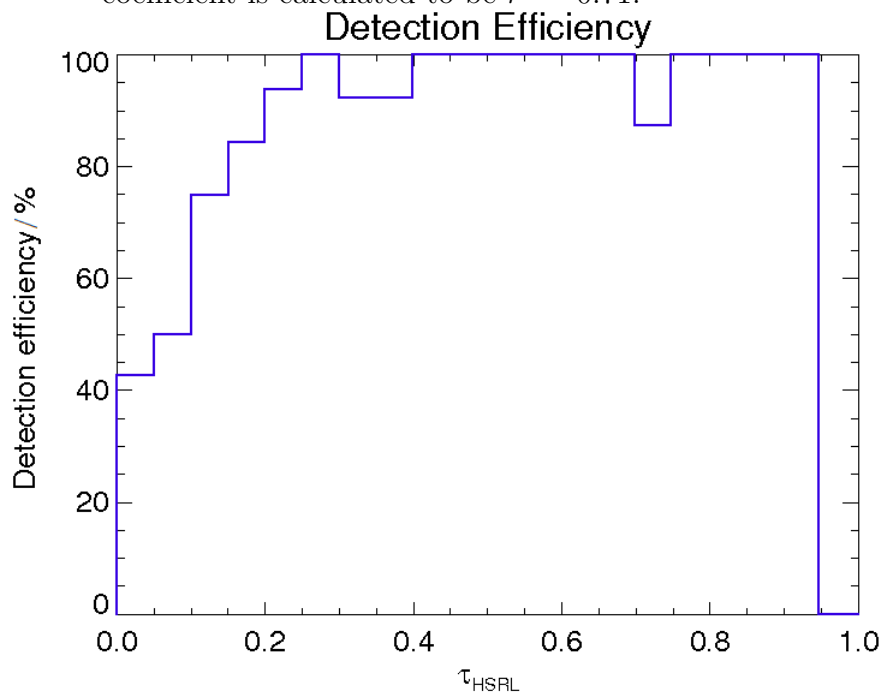


Figure 4.7: Detection efficiency of COCS compared to the values of cirrus optical thickness measured by HSRL during the FALCON flight, 18 October 2008.

4.2 Validation with passive remote sensing

After validating the results of COCS with active remote sensing data, the Meteosat Cirrus Detection Algorithm 2 (MeCiDA-2) and the Algorithm for the Physical Investigation of Clouds with SEVIRI (APICS) are applied to measurements of SEVIRI and compared to COCS.

4.2.1 Comparison with MeCiDA-2

The Meteosat Cirrus Detection Algorithm 2 (MeCiDA-2) [Krebs, 2006, Krebs et al., 2007, Ewald et al., 2012] used for the intercomparison with COCS, is a dedicated cirrus detection algorithm developed at DLR in the past years.

In general, MeCiDA-2 utilizes threshold and morphological tests on the thermal infrared

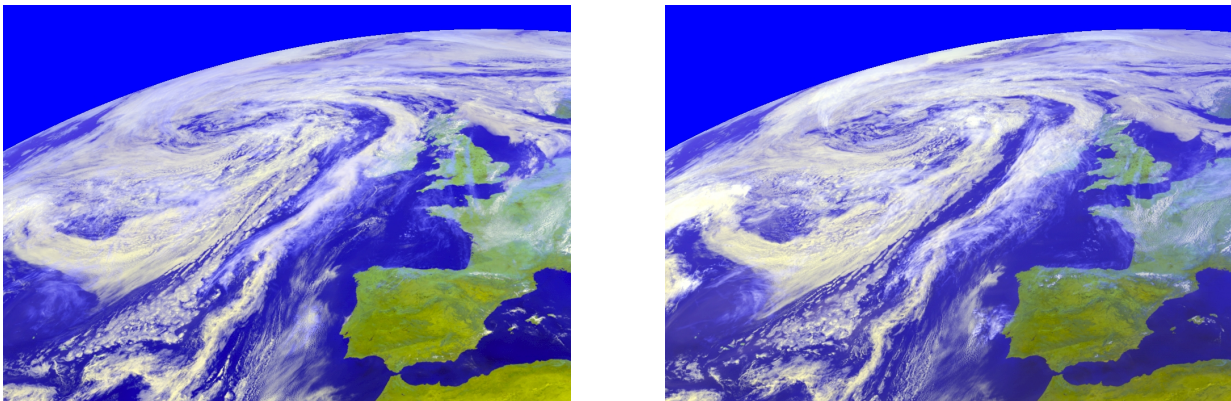


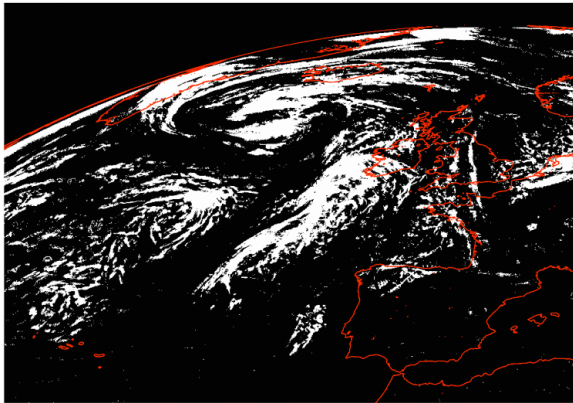
Figure 4.8: False color composites taken by SEVIRI on the 22 June 2010 at 12:00 UTC (left) and at 16:00 UTC (right). Cirrus clouds are depicted in white/blueish color, while water clouds are grey.

brightness temperatures and their differences of SEVIRI aboard MSG in order to mark pixels that are covered by cirrus clouds. On the one hand MeCiDA-2 uses well-known tools like the split-window test, where the brightness temperature difference of two channels is compared to a threshold. On the other hand MeCiDA-2 uses the morphological properties of cirrus clouds in the water vapour channels of SEVIRI. Here, cirrus clouds generate high-frequency disturbances due to their small scale variability, which can be extracted from the homogeneous water vapour background by a high pass filter. The utilisation of the thermal infrared channels enables MeCiDA-2 to detect cirrus clouds during day and night time, similarly to COCS.

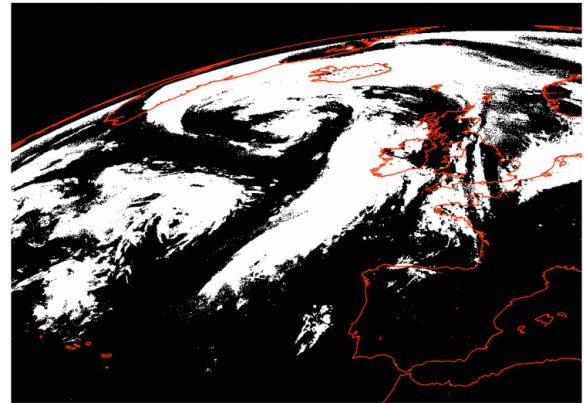
In Fig. 4.8, a typical scene over Western Europe and the North Atlantic is shown as a false color composite for two different time slots on 22 June 2010. The left picture was taken at 12:00 UTC, the right one at 16:00 UTC. Ice clouds are depicted in white/blueish colors, while water clouds are depicted in grey. In wide parts of the scene water clouds

are covered by high cirrus clouds, which can be hardly distinguished by eye, especially in the western part of the images, where a large low pressure system is dominating the weather. To the south some thin cirrus clouds are found west of Spain. France and England show some cirrus coverage as well. These scenes have been processed by both cirrus detecting algorithms, MeCiDA-2 and COCS, to show the difference in detection. Therefore, Fig. 4.9 depicts the results of MeCiDA-2 (left column) and COCS (right column) for 22 Juni 2010 at 12:00 and 16:00 UTC. MeCiDA-2 on the left detects high cirrus clouds

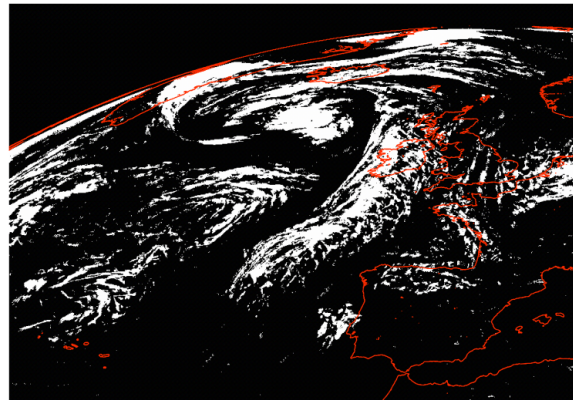
MeCiDA detection, 22/06/2010 at 1200 UTC



COCS detection, 22/06/2010 at 1200 UTC



MeCiDA detection, 22/06/2010 at 1600 UTC



COCS detection, 22/06/2010 at 1600 UTC

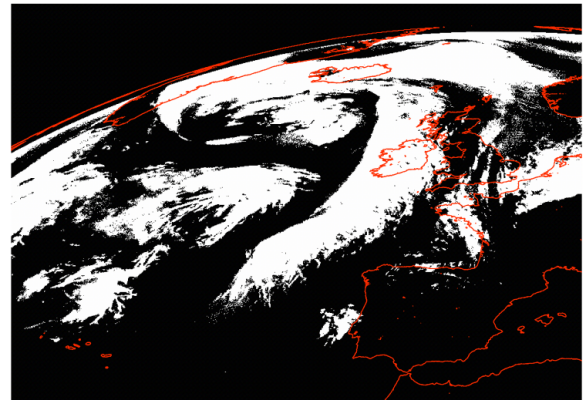


Figure 4.9: Results of MeCiDA-2 (left panels) and COCS (right panels) on the 22 June 2010 at 12:00 UTC (top) and at 16:00 UTC (bottom).

at both timeslots within the area of the low pressure system west of Ireland around the twisting center. North of England some cirrus stripes are detected at 12:00 and 16:00 UTC as well as over England. Over the North Sea and the Netherlands another region with cirrus coverage is detected by MeCiDA-2. South-west of the low pressure system, single cirrus clusters are retrieved, while the Southern part of the scene remains almost uncovered by cirrus clouds. In both scenes COCS detects significantly more cirrus clouds (right panels of Fig. 4.9). Especially cirrus clouds within the frontal systems of the low pressure system show a much higher coverage, which can be also seen west of the system,

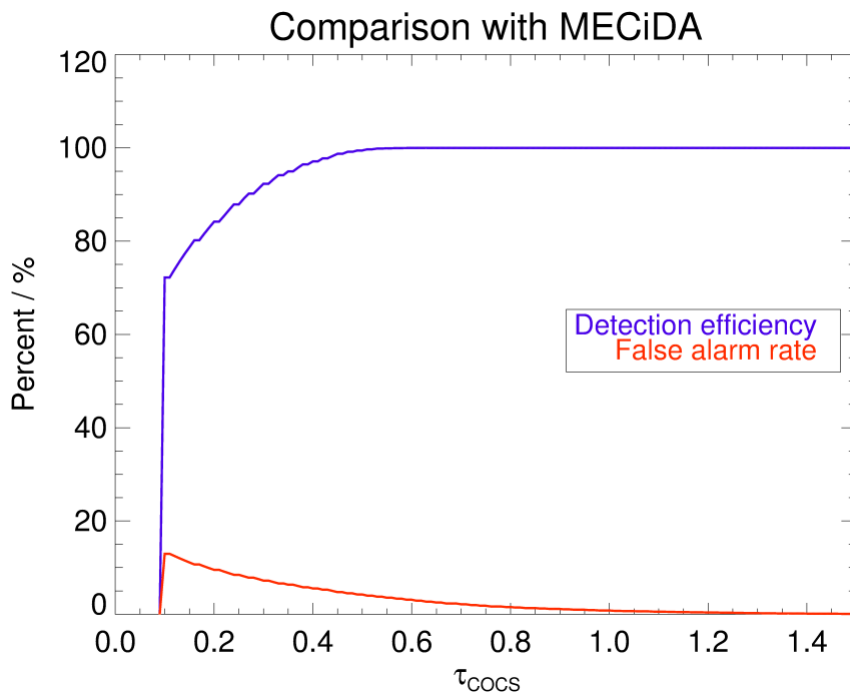


Figure 4.10: Detection efficiency (blue) and false alarm rate (red) of MeCiDA-2 as a function of cirrus optical thickness τ_{COCS} detected by COCS.

over England, and the Netherlands. A detailed comparison and validation of COCS and MeCiDA-2 in Ostler [2011] showed that MeCiDA-2 is less sensitive to thin cirrus clouds with $\tau \leq 0.4$, which are detected by COCS with high probability (see Fig. 4.4). The detection efficiency of MeCiDA-2 as a function of τ_{COCS} confirms these validation results (Fig. 4.10). For this purpose the region depicted in Fig. 4.8 (right) is chosen, 22 June 2010 at 16:00 UTC. While thick cirrus clouds with $\tau > 0.4$ are detected by MeCiDA-2 with a detection efficiency of 100 %, lower efficiencies ($det_{eff} = 73$ % at $\tau_{COCS} = 0.1$) are found for thin cirrus clouds increasing to higher optical thickness. The false alarm rate of MeCiDA-2 shows values of $far = 13$ % for cirrus clouds with an optical thickness of $\tau = 0.1$, which decreases for cirrus clouds with increasing ice optical thickness. Fig. 4.11 aims to illustrate the different sensitivities of both algorithms. Especially cirrus clouds with $\tau \geq 0.5$ are detected by both algorithms, while thin cirrus clouds with $\tau < 0.5$ are in some extent not detected by MeCiDA-2. These thin cirrus clouds on the one hand fill the gaps between parts of i.e. frontal cirrus clouds in both timeslots. On the other hand wide areas North of Scotland are covered with thin cirrus clouds only detected by COCS. This is confirmed by a closer look at the cirrus ice optical thickness retrieved by COCS (Fig. 4.12). While thick cirrus clouds are detected by both algorithms, thin cirrus clouds with low cirrus τ are only detected by COCS. Thick cirrus clouds are identified over the frontal systems of the low pressure system and south-west of it. Even the cloud cover-

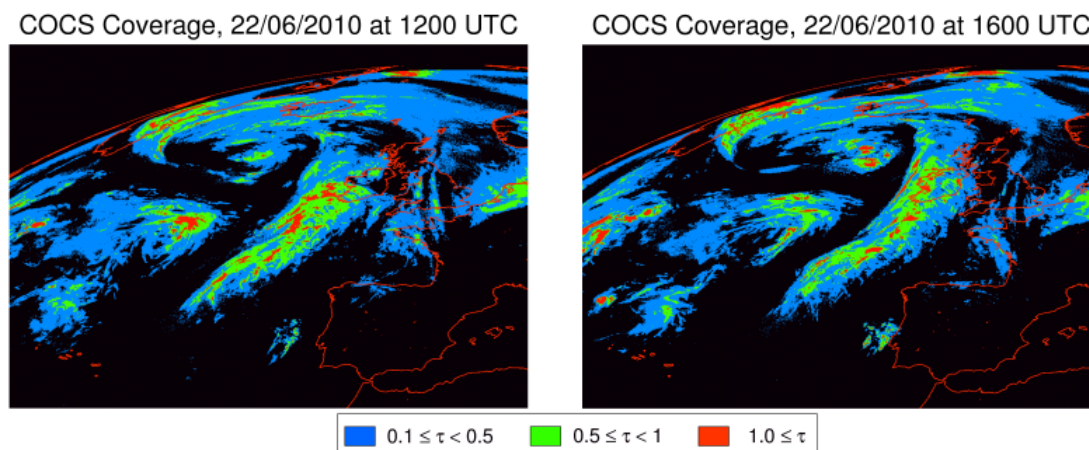


Figure 4.11: Cirrus coverage derived by COCS on the 22 June 2010 at 12:00 UTC (left) and at 16:00 UTC (right). The cirrus coverage is split into three classes of cirrus clouds depending on their cirrus optical thickness: blue for $0.1 \leq \tau < 0.5$, green for $0.5 \leq \tau < 1$, and $1.0 \leq \tau$.

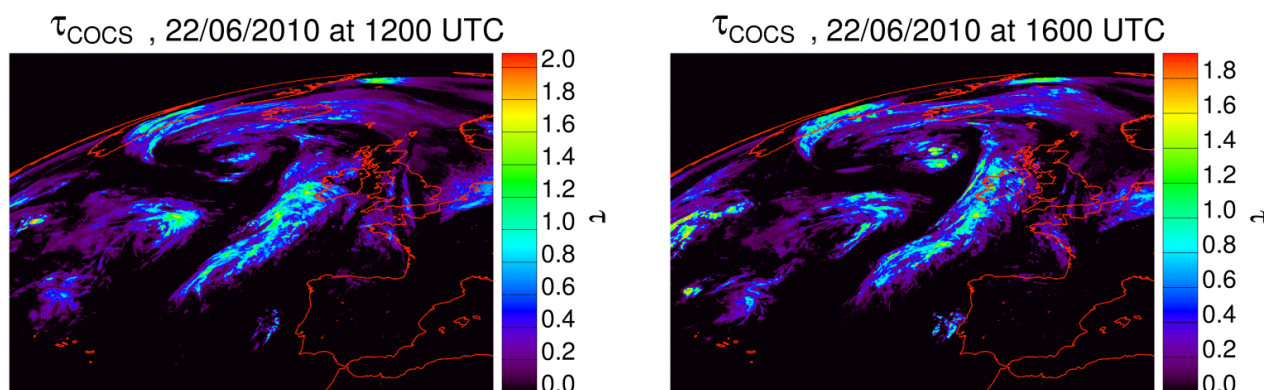


Figure 4.12: Cirrus ice optical thickness τ derived by COCS on the 22 June 2010 at 12:00 UTC (left) and at 16:00 UTC (right).

age over the Netherlands and the North Sea are found by both algorithms. Thin cirrus clouds are present in COCS in almost every cirrus covered region, but is most significant in the North-East of both scenes, where cirrus clouds with very low ice optical thickness is covering large areas North and North-East of England.

In Fig. 4.9 (right bottom) the development of the cirrus coverage is depicted at 16:00 UTC. Here, the westerly drift moves the areas covered with cirrus to the East, while the cirrus cloud over the North Sea and the Netherlands moves further to the South.

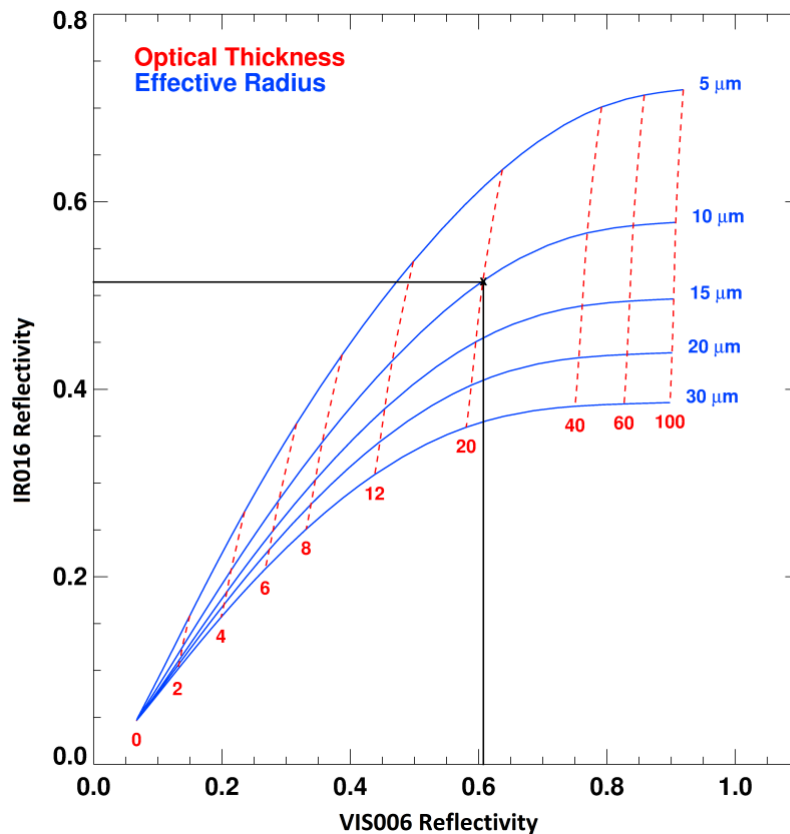


Figure 4.13: Theoretical relationship between the reflectivity function of the VIS006 and the IR016 SEVIRI channel for different values of cloud optical thickness and effective radius [adapted from L. Bugliaro].

4.2.2 Comparison with APICS

The Algorithm for the Physical Investigation of Clouds with SEVIRI (APICS) [Bugliaro et al., 2011] starts with the result of MeCiDA-2 to differentiate between cirrus-free pixels and those containing cirrus clouds. The retrieval of optical properties of ice clouds in APICS is based on a method first described by Nakajima and King [1990]. While the reflection of clouds in the visible spectrum (VIS) is mainly a function of cloud optical thickness, the reflection in the near infrared (NIR) spectrum highly depends on the particle size in the cloud. In Fig. 4.13 reflectivities of the IR016 channel (Reff016) as a function of the reflectivities of the VIS006 channel (Reff006) is plotted as a set of lines forming a net of optical thicknesses and effective radii calculated with the radiative transfer model libRadtran [Mayer and Kylling, 2005]. A couple of measured reflectivities (Reff006, Reff016) represent a point in this diagram an optical thickness and effective radius can be assigned to it. In this example, $\tau = 20$ and $r_{eff} = 10 \mu\text{m}$. In general, these reflectivities are pre-calculated for fixed atmospheric profiles and stored in so-called look-up tables as a function of solar and viewing geometry, surface albedo and optical thickness and effective

radius. While there is little dependency of the reflectivities in these two spectral intervals on cloud height and geometrical thickness, atmospheric gas and aerosol composition can affect the measurements as well. Another important aspect in the APICS retrieval is the parametrisation of the scattering properties of ice particles and their different shapes in a cirrus clouds, since the reflection of cirrus clouds is strongly influenced by them. In the present version, APICS is based on the ice model of Baum et al. [2005], which uses a mixture of different particle types depending on particle size for the parametrisation of optical properties.

For the comparison with COCS the 13 June 2008 was chosen (Fig. 4.14), where a cirrus outflow of a tropical cyclone is present south-east of the Horn of Africa covering a domain of 200×200 pixels. On the left τ_{APICS} shows values of ≤ 2.5 interrupted with areas of no cirrus clouds. On the right, τ_{COCS} is depicted. Two differences are to mention: On the one hand MeCiDA-2/APICS detects a much lower coverage than COCS, where no interruptions between the single ‘‘cirrus stripes’’ are present. On the other hand COCS retrieves lower τ compared to the results of APICS. A direct intercomparison is shown in Fig. 4.15,

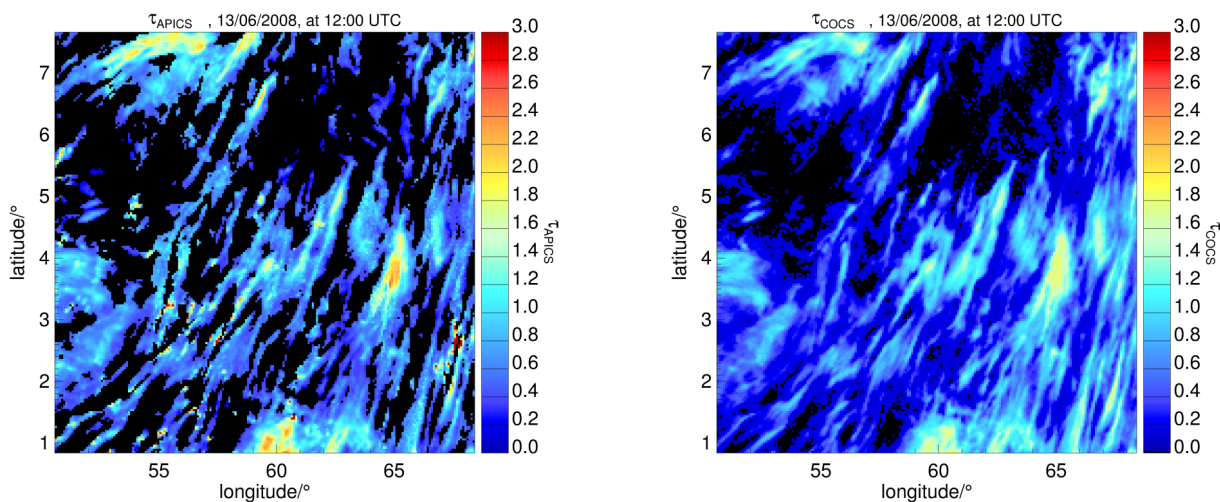


Figure 4.14: Cirrus optical thickness τ derived by APICS (left) and by COCS (right). τ_{APICS} and τ_{COCS} are derived from the brightness temperatures measured by SEVIRI on the 13 June 2008 at 12:00 UTC over the eastern limit of the SEVIRI disc, where a cirrus outflow of a tropical cyclone is present covering a domain of 200×200 pixel.

where three time slots 12:00 - 12:30 UTC are depicted in a two dimensional histogram. This plot confirms the results from Fig. 4.14 with some deviations especially at higher values of τ_{APICS} , where τ_{COCS} slightly underestimates the cirrus optical thickness. Especially at $\tau_{\text{APICS}} = 0$, COCS detects more thin cirrus clouds with $0.1 \leq \tau_{\text{COCS}} \leq 0.8$, where COCS is more sensitive than the combined method of MeCiDA-2 and APICS. The higher sensitivity to thin cirrus clouds of COCS can also be seen at very low ice optical thickness. COCS detects cirrus clouds with $\tau < 0.5$ more frequently than MeCiDA-2/APICS, which

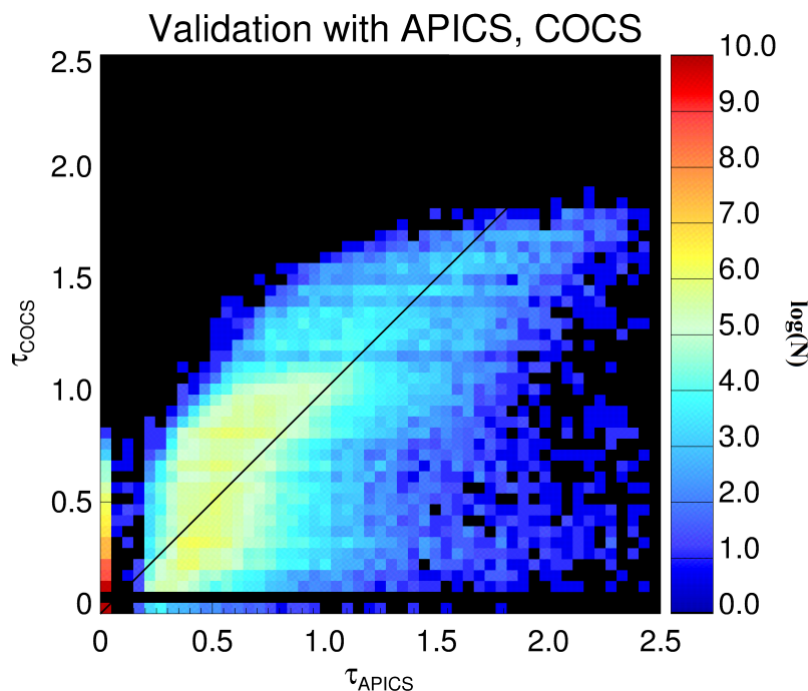


Figure 4.15: Scatter plot of the cirrus optical thickness τ of COCS and APICS on the 13 June 2008 for the three timeslots 12:00, 12:15, and 12:30 UTC covering the same area as in Fig. 4.14.

mainly detects cirrus with $\tau_{\text{APICS}} > 0.3$ in this case.

To summarize, differences appear due to the use of the less sensitive detection of cirrus clouds of MeCiDA-2, which uses threshold tests to determine whether an ice cloud is present or not. Further differences are caused by the general setup of COCS. COCS is trained with the data of CALIOP and therefore it is able to detect thin cirrus clouds, but only retrieves low cirrus ice optical thickness up to the limit of spaceborne lidar. This fact is shown in Fig. 4.16, where a strong convective cell has formed over Central Africa on the 13 June 2008 at 12:00 UTC. In the lower third some other small convective features are found as well. On the left of Fig. 4.16 the result for the cirrus optical thickness derived by APICS shows high values especially in the convective center of the cells reaching up to $\tau_{\text{APICS}} = 100$, while the optical thickness of the cirrus outflow and other cirrus clouds are detected with lower values. Especially for these convective formed cirrus clouds as well as for frontal cirrus clouds, COCS is likely to underestimate the ice optical thickness due to the saturation of the lidar backscatter signal of CALIOP penetrating clouds thicker than $\tau = 3 - 4$ (Section 3.1.1). Therefore, COCS gets saturated and retrieves a maximum $\tau_{\text{COCS}} = 2.5$. Only in cases of very strong convective formed cirrus clouds this value is exceeded and COCS reaches values of $\tau_{\text{COCS}} \approx 3.0$. In contrast, APICS is able to retrieve higher ice optical thickness, but in case of an underlying water cloud, APICS interprets

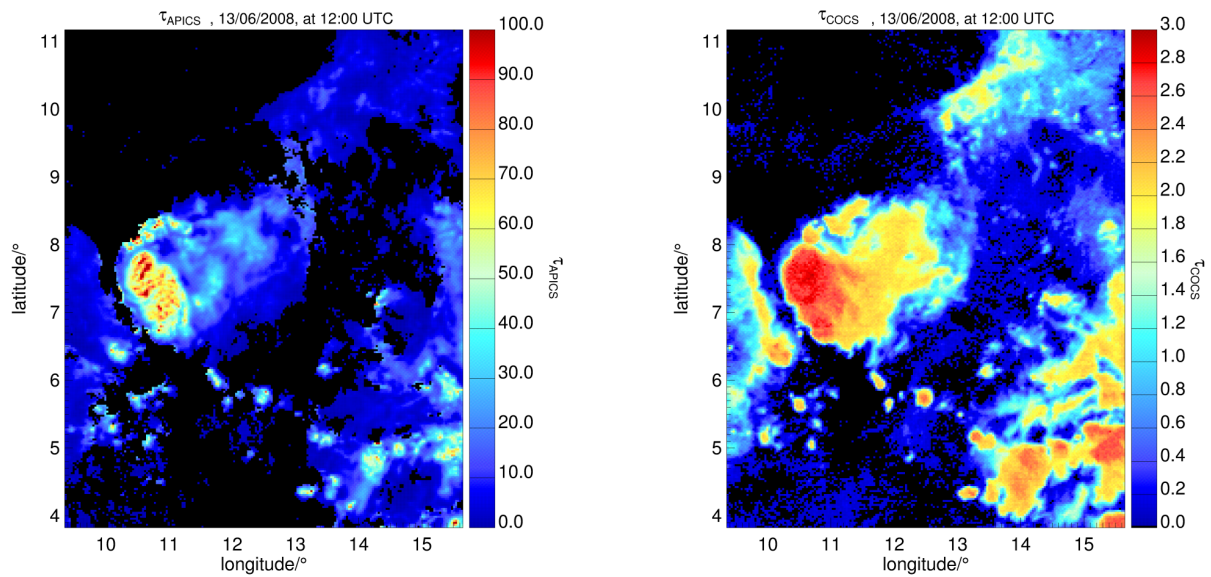


Figure 4.16: Cirrus optical thickness τ derived by APICS (left) and by COCS (right). τ_{APICS} and τ_{COCS} are derived from the brightness temperatures measured by SEVIRI on the 13 June 2008 at 12:00 UTC over Central Africa. In this scene a large convective cell has formed. Some small convective features are visible in the lower third of the scene. This domain covers 200 x 250 pixel. Please note the different scales.

the whole atmospheric column as an ice cloud and therefore overestimates the real ice optical thickness.

4.3 Systematic and statistical uncertainty

Before starting to analyse the different diurnal cycles of cirrus coverage and optical thickness retrieved by COCS, systematic and statistical uncertainties of the retrieved values are calculated, which are deemed here as bias and errors respectively. Earlier in this chapter, optical thickness and top altitude of the detected cirrus clouds were already validated with the airborne HSRL and the spaceborne CALIOP aboard CALIPSO. The results showed very low standard deviations. Additionally, low false alarm rates and high detection efficiencies were found. The cirrus coverage derived by COCS is based on the retrieved cirrus ice optical thickness. If COCS retrieves an optical thickness $\tau \geq 0.1$ a cirrus cloud is detected (Section 4.1.1). Thus, the cirrus coverage can be calculated by the ratio of pixels, where a cirrus cloud is detected, and the total amount of pixels (where cirrus clouds are detected and cirrus-free). Usually this ratio is given in percent.

The training of the COCS algorithm was performed on the temporal and spatial collocated datasets of SEVIRI and CALIOP measurements. Therefore, bias and error calculations for the retrieved cirrus coverage and ice optical thickness are based on the test dataset (Section 4.1.1), since CALIOP is the best performing instrument for the detection and retrieval of cirrus clouds and their properties.

Cirrus coverage

Concerning the retrieved cirrus coverage, a general bias results from the higher sensitivity of CALIOP with respect to very thin cirrus clouds such as subvisible cirrus. Due to its false alarm rate and detection efficiency, COCS has a lower detection limit of $\tau = 0.1$ (Section 4.1.1). Pixels with a retrieved cirrus optical thickness lower than $\tau = 0.1$ are considered as cirrus-free. CALIOP detects cirrus clouds already within the range of $\sim 0.01 < \tau < 0.1$. Therefore, this class of cirrus clouds can be deemed as the general bias, which is calculated as 1.81 % of the total cirrus coverage in the test dataset. In order to derive the bias and the standard deviation of cirrus coverage for the single values of τ , equidistant intervals with $\Delta\tau = 0.1$ are used up to $\tau = 1.0$, and for greater optical thickness intervals of $\Delta\tau = 0.3$ are chosen to have a constant number of ≈ 10000 observations in each interval. However, since CALIOP detects less cirrus clouds with $\tau \geq 2.0$ than cirrus clouds with lower optical thickness the intervals covering $\tau \geq 2.0$ contain only ≈ 1000 observations. The bias for each interval is calculated as the number of cirrus cloud pixels missed by COCS, but detected by CALIOP. This bias is depicted in Fig. 4.17 (left). Especially for thin cirrus clouds a bias is found with around 2 %, but decreases for growing ice optical thickness to almost zero.

In order to estimate the error of COCS against the measurements of CALIOP, the root mean square error (RMS) is calculated. The RMS works as an estimator to quantify the difference between the results derived by COCS and the results derived by CALIOP to

quantity being estimated. First, the ratio of misclassified clouds of COCS compared to CALIOP, $r_{i,\text{false}}$, is calculated as:

$$r_{i,\text{false}} = \frac{n_{\Delta\tau}^{\text{CALIOP}} - n_{\Delta\tau}^{\text{COCS}}}{n_{\text{total}}^{\text{CALIOP}}} , \quad (4.4)$$

where $n_{\Delta\tau}^{\text{COCS}}$ is the number of pixels where COCS detects a cirrus cloud with an ice optical thickness within the range of the ice optical thickness bin $\Delta\tau$. $n_{\Delta\tau}^{\text{CALIOP}}$ is number of observations by CALIOP with the derived τ_{CALIOP} with $\Delta\tau$. The amount of cirrus detection of CALIOP is given by $n_{\text{total}}^{\text{CALIOP}}$. The RMS, $\sigma_{\Delta\tau}^{\text{cov}}$, for the cirrus ice optical thickness bins is therefore calculated with the ratio of misclassified clouds of COCS compared to CALIOP, $r_{i,\text{false}}$:

$$\sigma_{\Delta\tau}^{\text{cov}} = \sqrt{\frac{1}{n_{\Delta\tau}^{\text{COCS}} - 1} \sum_{i=1}^{n_{\Delta\tau}^{\text{COCS}}} (r_{i,\text{false}})^2} , \quad (4.5)$$

The result of the RMS is shown as black error bars in Fig. 4.17 (left). The RMS shows values of around $\sigma_{\Delta\tau}^{\text{cov}} = 0.5 \%$ for low ice optical thickness and decreases for higher IOTs. The only outlier is found for $\tau \geq 2.2$, where $\sigma_{\Delta\tau}^{\text{cov}} = 0.5 \%$.

For large datasets the arithmetic RMS is often calculated considering a large amount of observations $Obs_{\Delta\tau}$ in the adequate ice optical thickness interval:

$$\sigma_{AM} = \frac{\tilde{\sigma}}{\sqrt{Obs_{\Delta\tau}}} , \quad (4.6)$$

Therefore, the arithmetic RMS has very low values within the order of $\tilde{\sigma}_{AM} \approx 10^{-5}$ in case of this work where a dataset consisting of five years is analysed, and is not part of the graphics shown in the following chapter.

Ice optical thickness

Similarly to the error and bias calculation for the cirrus coverage a bias is calculated for the same intervals defined above. The bias is calculated as:

$$\Delta\tau_{\text{bias}} = \frac{1}{n_{\Delta\tau}} \sum_{i=1}^{n_{\Delta\tau}} (\tau_{i,\text{COCS}} - \tau_{i,\text{CALIOP}}) , \quad (4.7)$$

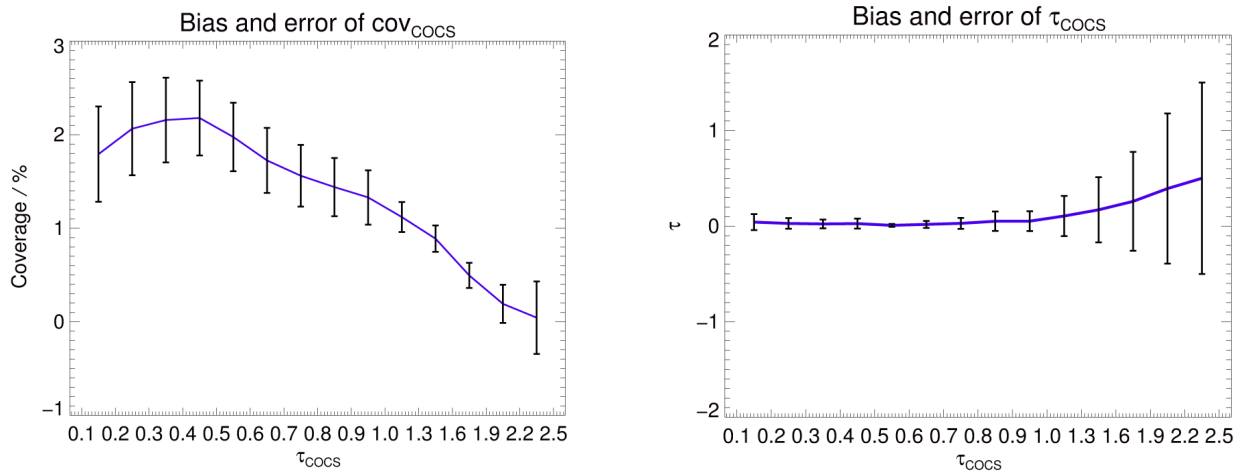


Figure 4.17: Bias of the retrieved cirrus coverage (left) and ice optical thickness (right) depicted as a blue line. Root mean square errors from CALIOP values depicted as black error bars for the single intervals of τ_{COCS} .

where $n_{\Delta\tau}$ is the number of detected cirrus clouds in the interval of cirrus ice optical thickness, $\tau_{i,COCS}$ the value of COCS, and $\tau_{i,CALIOP}$ the value of CALIOP. This calculated bias is depicted in Fig. 4.17 (right) again for the IOT intervals and has very low values up to an ice optical thickness $\tau_{COCS} = 1.0$. For higher IOTs the bias increases until it reaches a maximum of up to 0.5. The root mean square error for the retrieved compared to the CALIPSO measurements is corrected with the bias for the single optical thickness class, since every measurement is contaminated by this bias, Eq. 4.7. Therefore, the root mean square error of the retrieved cirrus optical thickness $\sigma_{\Delta\tau}^{\tau}$ can be calculated as:

$$\sigma_{\Delta\tau}^{\tau} = \sqrt{\frac{1}{n_{\Delta\tau} - 1} \sum_{i=1}^{n_{\Delta\tau}} (\tau_{i,COCS} - \tau_{i,CALIOP} - \Delta\tau_{\text{bias}})^2}. \quad (4.8)$$

This RMS is plotted in Fig. 4.17 (right) with low values up to a cirrus ice optical thickness of $\tau = 1.0$. This RMS increases for higher cirrus ice optical thicknesses to values of up to 0.9. Again, the arithmetic root mean square error for the ice optical thickness calculated from five years of data is very low and hence is not plotted in the diurnal analysis with values $\tilde{\sigma}_{AM} \approx 10^{-3} \%$.

Chapter 5

Cirrus diurnal cycles

Within the framework of this thesis five years of data were processed with the Cirrus Optical properties derived from CALIOP and SEVIRI during day and night (COCS) algorithm. The period covers the years 2006 to 2010 at the high temporal resolution of 15 minutes. Based on this dataset of cirrus ice optical thickness (τ_{COCS}) and top altitude (z_{COCS}) detailed analysis of the diurnal cycle of cirrus cloud coverage and cirrus ice optical thickness are realised and compared to forecasts of high cloud coverage calculated by the European Center for Medium-range Weather Forecasts (ECMWF) in this section. Finally, two regions, one of them strongly influenced by air traffic and one without the influence of air traffic are analysed and discussed.

5.1 Cirrus cloud coverage

In Sassen et al. [2008] analysis of total and seasonal cirrus cloud coverage were accomplished with combined data from CALIOP aboard CALIPSO (Section 2.3.2) and the Cloud Profiling Radar (CPR) aboard CloudSat. Relying on one year of data global and seasonal frequencies of cirrus clouds are reported (from 15 June 2006 to 15 June 2007). The global distribution of average frequency of occurrence of cirrus clouds identified by this CloudSat/CALIPSO algorithm is depicted in Fig. 5.1. The maximum cirrus coverage of up to 60 % is found in the tropical belt mainly as a result of anvils produced directly by deep convection in the Intertropical Convergence Zone (ITCZ) and monsoonal circulations. This high coverage is present over Equatorial Central South America, Western Africa, Indonesia, and the West-Central Pacific Oceanic warm pool. A still high, but lower coverage is seen at the Northern and Southern mid-latitude stormtracks with values around 35 %. Less coverage is found over land masses, the deserts and desert-like regions of Northern Africa, Western China, Central Australia, and the South-Western United States. Minima in cirrus coverage appear at high polar altitudes and the upper mid-latitudes bounding the ITCZ. For the period from 01 January 2010 to 31 December

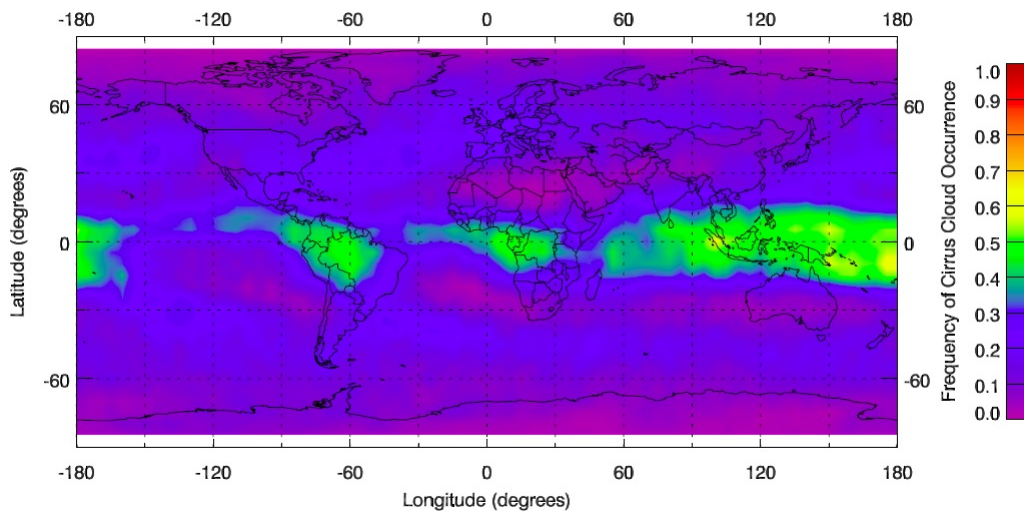


Figure 5.1: Global distribution of average frequency of occurrence of cirrus clouds identified by the CloudSat/CALIPSO algorithm within 5.0° latitude by 5.0° longitude grid boxes during daylight and nighttime measurements, [Sassen et al., 2008].

2010, the cirrus coverage derived by the COCS algorithm is depicted in Fig. 5.2 at a resolution of $0.5^\circ \times 0.5^\circ$. Again we find high cirrus coverage in the ITCZ over Central and Western Africa and the western part of South America with values of up to 60 %, while desert-like regions of Northern Africa, the Arabian Peninsula and Southern Africa show rather low values of only 0 to 20 %. In opposition to the values derived by Sassen et al. [2008] in Fig. 5.1 especially the Northern and Southern Atlantic regions are found to have higher values in this time period with values around 40 %. Please note, that both plots use different color tables. Supported by these first results, five different regions of interest within the area covered by SEVIRI, from 80° N to 80° S and from 80° W to 80° E, were chosen for further studies and analysis (Fig. 5.2):

- the North Atlantic Region (NAR), 45° N to 55° N and 45° W to 10° W, with a maximum satellite viewing zenith angle (VZA) of 74.5° ,
- the Mediterranean Region (MED), 30° N to 40° N and 0° to 35° E, with a maximum VZA of 58.3° ,
- the South African Region (SAC), 30° S to 20° S and 0° to 35° E, with a maximum VZA of 51.5° ,
- two South Atlantic Regions: SAR1, 55° S to 45° S and 45° W to 10° W, with a maximum VZA of 74.5° , and SAR2, 60° S to 45° S and 45° W to 45° E, with a maximum VZA of 77.8° .

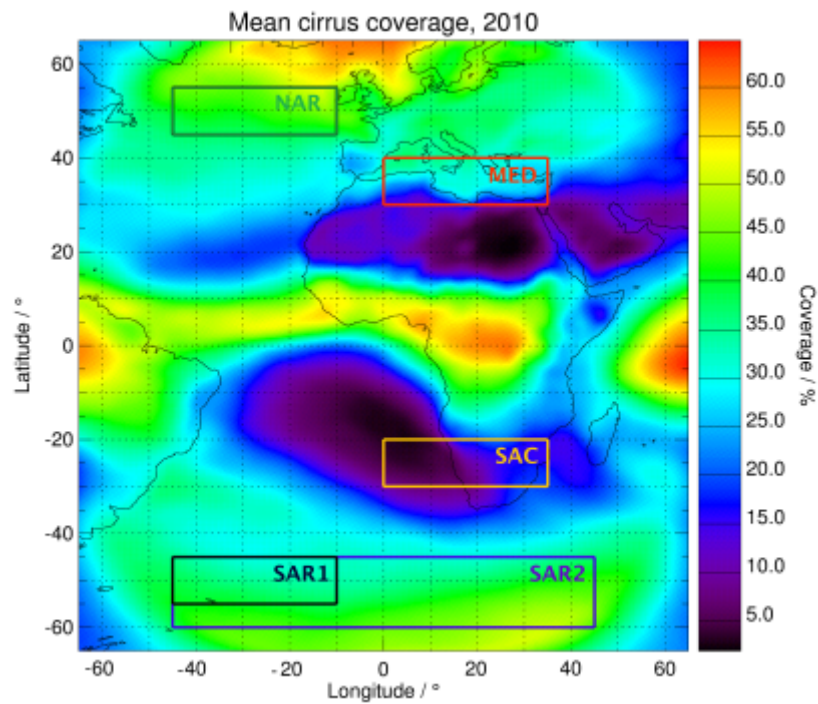


Figure 5.2: Mean cirrus coverage for the year 2010 at a resolution of $0.5^\circ \times 0.5^\circ$ with the selected regions for further analysis from north to south: NAR (green), MED (red), SAC (orange), SAR1 (black), and SAR2 (blue).

The NAR, SAR1, and SAR2 regions were chosen due to the homogeneous sea surface, where orographical and convective influence is mainly absent. Furthermore, the NAR is influenced by cirrus clouds formed by air traffic due to the North Atlantic air corridor, which is one of the most frequented oceanic air traffic routes in the world with flights from the United States of America to Europe and vice versa. In order to analyse the difference to an undisturbed atmosphere, the SAR1 region was defined, representing a similar area as the NAR just mirrored to the southern hemisphere. The SAR2 region covers 90° of longitude over the South Atlantic and represents an undisturbed atmosphere without air traffic and orographical or convective influence.

Additionally, two regions with stronger landmass and convective influence are chosen. The MED region covers wide parts of the Mediterranean Sea and the coasts of Northern Africa, and the SAC region, which is located over the Atlantic and South Africa. Please note, that both regions are chosen to cover the same longitude, but are not symmetric in terms of latitude, so that differences in ice optical properties and cirrus coverage are expected as seen in Fig. 5.1.

With the high temporal resolution and the independence from daylight COCS establishes the possibility to give insights into the diurnal variations of cirrus. For the analysis of cirrus cloud coverage and ice optical thickness in this chapter, all curves are corrected by

the general bias and the bias for the single intervals calculated in Section 4.3.

5.1.1 Total Cirrus Coverage

For a first overview the diurnal cycle of the total cirrus coverage in the five defined regions is depicted as a function of local time (LT), Figure 5.3. In the following the so-called total cirrus coverage designates the mean cirrus coverage for each region and is shown for the period from 2006 to 2010 at a temporal resolution of 15 minutes. The single pixels are averaged to a resolution of 0.25° in terms of latitude and longitude and then averaged to the coverage of the above defined regions.

The conversion from UTC to LT is done by assuming that the 0° -Meridian has the same time for UTC and LT. By accounting the 0.25° longitude resolution, the LT is then calculated can be calculated by adding 60 s for each 0.25° step in the eastward direction and subtracting 60 s in the westward direction.

The total cirrus coverage can be differentiated in two different classes due to the location of the averaged regions:

MED and SAC show a diurnal cycle dominated by a maximum cirrus coverage between 13:00 and 16:00 LT respectively, which indicates the presence of convection, and a minimum in the morning at around 07:00 LT. The coverage in SAC varies from the minimum with a value of 11 % with a rather sharp increase to a maximum of 16 % followed by a slow decrease during night. In the MED the morning minimum coverage reaches 22 % and peaks in the maximum at 26 %. At night a slower decline than in SAC is observed. On the other hand, the three maritime regions NAR, SAR1, and SAR2 show a different diurnal cycle. The cirrus coverage follows a semidiurnal curve with two maxima and two minima. In SAR2, the first minimum is detected at around 00:00 LT with a coverage of 39% followed by the first maximum at 05:00 LT with a value of 41 %. The second minimum is reached at 11:00 LT (49 %). The cirrus coverage increases to the second maximum (40 %) at 18:00 LT.

The smaller SAR1 region shows a slightly lower cirrus coverage than the SAR2 region. An offset in total cirrus coverage of around -1 % is present with respect to SAR2, while the diurnal cycle is similar to the curve of SAR2. The two minima are again reached at 00:00 and 11:00 LT, followed by two maxima at 05:00 and 18:00 LT.

In NAR the diurnal cycle is different from the regions in the South Atlantic. While the shape of the curve is equivalent to SAR1 and SAR2 from 00:00 to 10:00 LT, the diurnal cycle starts to differ afterwards. The first coverage maximum (40 %) is reached at 05:00 LT. The first minimum is reached 1.5 h earlier than in the South Atlantic at around 10:00 LT after a small decay to a coverage of 38 %. This minimum is followed by the second maximum (40 %), which is caught at around 15:00 LT (2 h earlier compared to SAR1 / SAR2). The second minimum (38 %) is found at 22:00 LT. Even though the global distri-

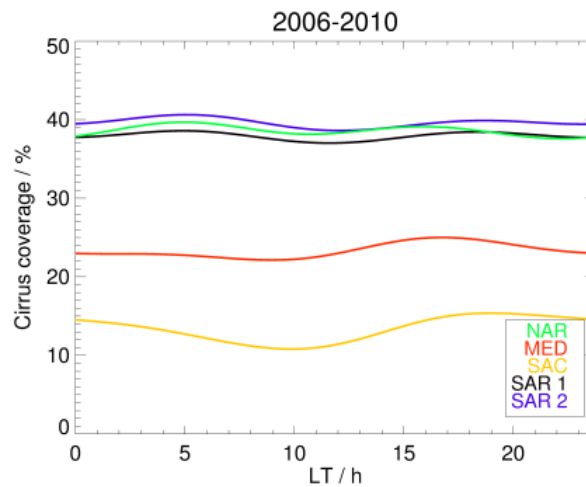


Figure 5.3: Total cirrus coverage in local time for the five years of processed COCS data for the five regions in Figure 5.2: NAR (green), MED (red), SAC (yellow), SAR1 (black), and SAR2 (blue).

bution of cirrus clouds (Fig. 5.1) shows only small differences between the selected regions (Fig. 5.2), significant differences and features in the diurnal cycle of the cirrus coverage are found. While the continental regions (MED, SAC) show strong convective influence in the diurnal cycle especially in the afternoon, the cirrus coverage in the maritime regions (NAR, SAR1, and SAR2) is found to follow a semidiurnal cycle.

Please note, that all curves here and in the following are only corrected by the bias. The statistical uncertainty is not depicted in the single plots, since its values are lower than the line width of the plot (Section 4.3) with values of less than 0.02 %.

5.1.2 Seasonal cirrus coverage

In order to retrieve the influence of a varying atmosphere in the seasonal variation of the cirrus coverage, the five regions of Fig. 5.2 are analysed according to the four seasons: Spring (March, April, and May), summer (June, July, and August), autumn (September, October, and November), and winter (December, January, and February). The season are shortened to MAM, JJA, SON, and DJF in the following. Additionally, the seasonal cirrus coverage is split into classes concerning the cirrus ice optical thickness of each detected cirrus cloud:

- thin cirrus: $0.1 \leq \tau < 0.5$,
- medium cirrus: $0.5 \leq \tau < 1.0$,
- thick cirrus: $\tau \geq 1.0$.

5.1.2.1 Seasonal cirrus coverage in MED

In Fig. 5.4a the total cirrus coverage varies strongly from around 7 % in JJA to 36 % in DJF. While three seasons (MAM, JJA, and SON) are dominated by convection and show a maximum in the afternoon (between 13:00 and 15:00 LT) and a minimum in the morning at around 05:00 LT, the winter season DJF is dominated by two maxima (the first one at 04:00 LT, the second one at 14:00 LT) and two minima (the first one at 07:00 LT, the second one at around 21:00 LT) and therefore shows a very different diurnal cycle. In these months with less or almost no convection we find cirrus clouds forming a wave-like diurnal cycle similar to the maritime regions (NAR, SAR1, and SAR2) during the whole year (Fig. 5.3).

Fig. 5.4b-e show the cirrus coverage split into different cirrus classes for the single seasons. During the MAM (Fig. 5.4b), a cirrus coverage slightly dominated by convection is found. This convection in the MED region is mostly taking place over landmasses in this region, namely North Africa and parts of Southern Europe. At around 15:30 LT the thick cirrus coverage reaches its maximum with a value of around 8 %, followed by the medium cirrus peak at around 16:00 LT with about 9 % of cirrus coverage. At 17:00 LT thin cirrus coverage peaks at values of 17 %. This shift in the maximum is probably caused by convective initiated cirrus coverage. So, if a convective cloud is growing in this region, COCS detects the anvil with its high ice optical thickness first, before the anvil spreads with time influenced by wind direction and speed, which raises the cirrus coverage but lowers the ice optical thickness. After sunset convection slows down or even stops, which results in a decrease of the coverage of all cirrus classes during night until the early morning at around 09:00 LT.

In JJA (Fig. 5.4c), a very low cirrus coverage is detected in the MED region with a slight convective dominated diurnal cycle in all three cirrus classes.

In SON (Fig. 5.4d) another convective dominated diurnal cycle of the cirrus coverage is found, where thick cirrus clouds reach their maximum coverage at 16:00 LT. Medium cirrus clouds peak later at 16:30 LT and finally the thin cirrus follows at around 17:00 LT. The values of the single cirrus classes are almost similar to the MAM. Thin cirrus have a maximum value of 18 %, 8 % for medium cirrus, and 5 % for thick cirrus.

In contrast to the results for MAM, JJA, and SON, the seasonal diurnal cycle in DJF shows different features and generally the highest seasonal cirrus coverage (Fig. 5.4e). Thin cirrus cloud coverage is present in the MED at a value of 21 – 22 %, medium cirrus covers the MED at a value of 9 – 10 %, and thick cirrus is detected with a coverage of around 7 – 8 %. The diurnal cycle is not only dominated by convection. It shows features similar to the total cirrus coverage in the NAR, SAR1, and SAR2 in Fig. 5.3. Thin cirrus clouds show two maxima (first at 05:00 LT, second at 19:00 LT) and two minima (first at 00:00 LT, second at 12:00 LT). The diurnal cycle of medium cirrus coverage shows

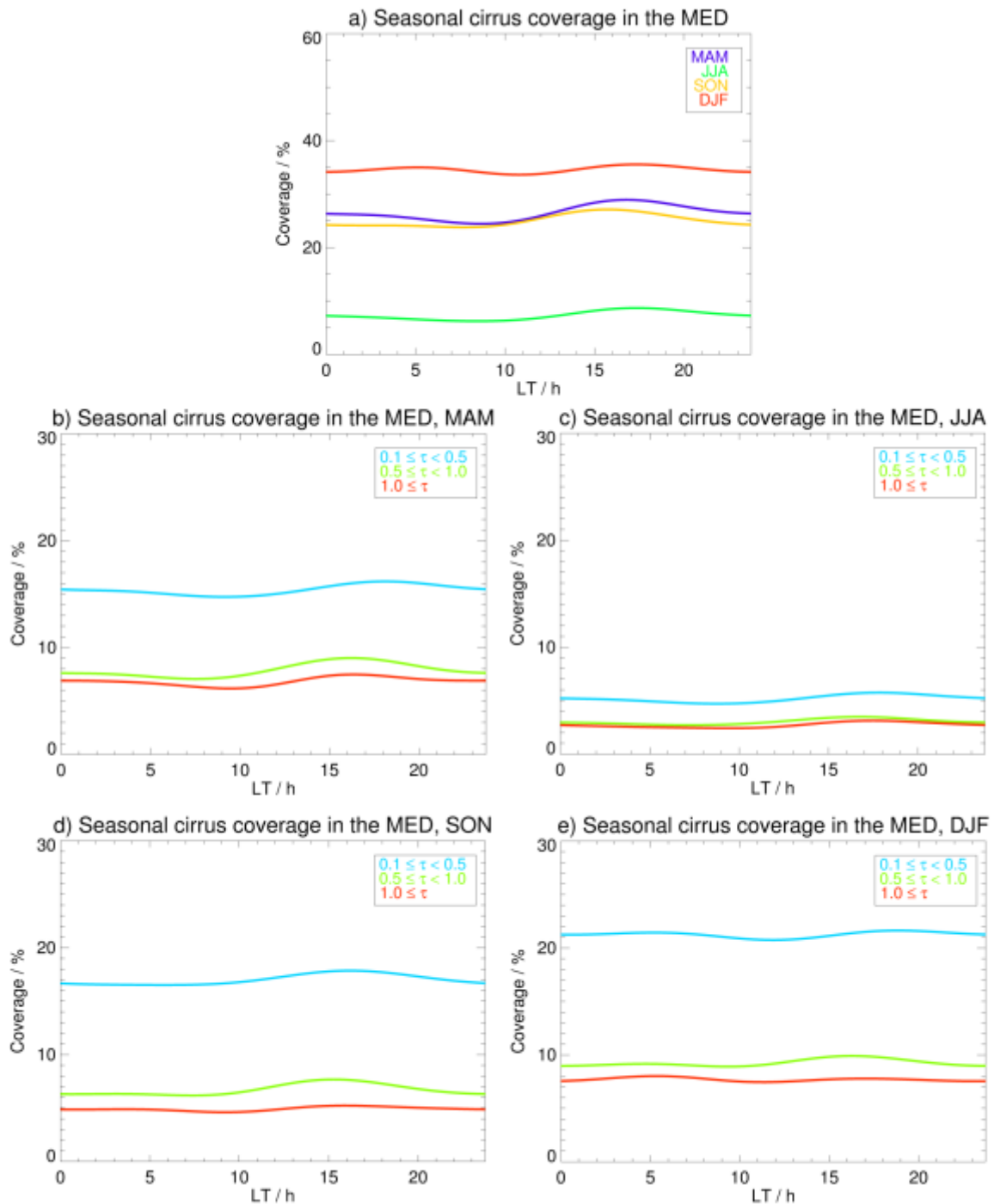


Figure 5.4: a: Seasonal total cirrus cloud coverage in the MED region, color coded: MAM (blue), JJA (green), SON (yellow), and DJF (red). b-e: Seasonal cirrus coverage split in different classes of ice optical thickness for MAM (b), JJA (c), SON (d), DJF (e).

only one significant maximum at 16:00 LT, while thick cirrus coverage peaks at 05:00 LT. Since medium and thick cirrus coverage have only small variations during the day, the diurnal cycle of the total cirrus coverage in the DJF season in Fig. 5.4a is dominated by the presence of thin cirrus clouds, which results in the wavelike shape of the cirrus coverage with two maxima and two minima.

5.1.2.2 Seasonal cirrus coverage in SAC

Another region dominated by convection is the SAC region in Fig. 5.2. The seasonal variations of the diurnal cycle are depicted in Fig. 5.5a, where especially in the afternoon (between 17:00 and 19:00 LT) the cirrus coverage reaches its maximum during the seasons MAM, SON, and DJF. During these seasons, the diurnal cycle shows minima between 09:00 and 11:00 LT. The highest variation in cirrus coverage is seen in the southern hemispheric summer (DJF) with a difference of 8 % between minimum (15 %) and maximum (23 %). During spring (SON) and autumn (MAM) the coverage is lower than during DJF, with a maximum coverage of up to 16 % and a minimum of 12 % respectively and a lower variation of the coverage of around 4 %. In the southern hemispheric winter (JJA) no clear diurnal cycle in cirrus coverage is detectable when the convective influence in cirrus formation and decay is negligible.

In the southern hemispheric spring (SON) (Fig. 5.5d) when the total cirrus coverage is rather low, the convective influence on the diurnal cycle of thick cirrus clouds is present with one minimum (3 %) at 10:00 LT and one maximum (7 %) in the afternoon at 18:00 LT. The coverage of medium cirrus shows only a slight increase from the minimum (4 %) in the morning at 10:00 LT to its maximum (5 %) at 16:00 LT. Thin cirrus coverage is depicted with higher values for its minimum (8 %) at 10:00 LT and its maximum (10 %) in the night at 02:00 LT.

In summer (DJF), the diurnal cycle in the SAC region is dominated by the coverage of thick cirrus (Fig. 5.5e). With a minimum (5 %) at 10:00 LT and a maximum (13 %) at 18:00 LT the diurnal cycle shows a sharp increase between the minimum and the maximum and a shallow decrease during evening and night. Connected to this strong convective growth of thick cirrus clouds and their decay during night, medium thick cirrus clouds have their maximum (7 %) at 23:00 LT in the evening, while the minimum (5 %) is reached at 09:00 LT. The coverage of thin cirrus clouds show an inverse diurnal cycle. The maximum of thin cirrus coverage (12 %) is detected at 02:00 LT and its minimum (10 %) is present at 17:00 LT.

In autumn (MAM) the convective influence is again present in the diurnal cycle, Fig. 5.5b. Thick cirrus coverage peaks in one maximum (5 – 6 %) at 18:00 LT and one minimum (4 %) at 10:00 LT. Medium cirrus coverage shows a similar behaviour with a slightly lower variation. The maximum (5 %) is reached at 17:00 LT, the minimum (4 %) is found at 09:00 LT. Thin cirrus clouds have their maximum coverage (10 %) in the late afternoon at 18:00 LT and their minimum (8 %) at 10:00 LT.

During the southern hemispheric winter (JJA) (Fig. 5.5c) no diurnal cycle is present. While thin cirrus clouds cover SAC with 4 – 5 %, medium and thick cirrus clouds result in a coverage of 2 – 4 %.

Even though the cirrus coverage in the SAC region is lower than in the MED area, the

strong convective influence in cirrus coverage over land masses is comparable. Due to convection thick cirrus clouds e.g. anvils of cumulonimbus clouds form fast during daytime and then spread over wide areas. This spreading leads to thinner cirrus clouds until the decay during evening and night.

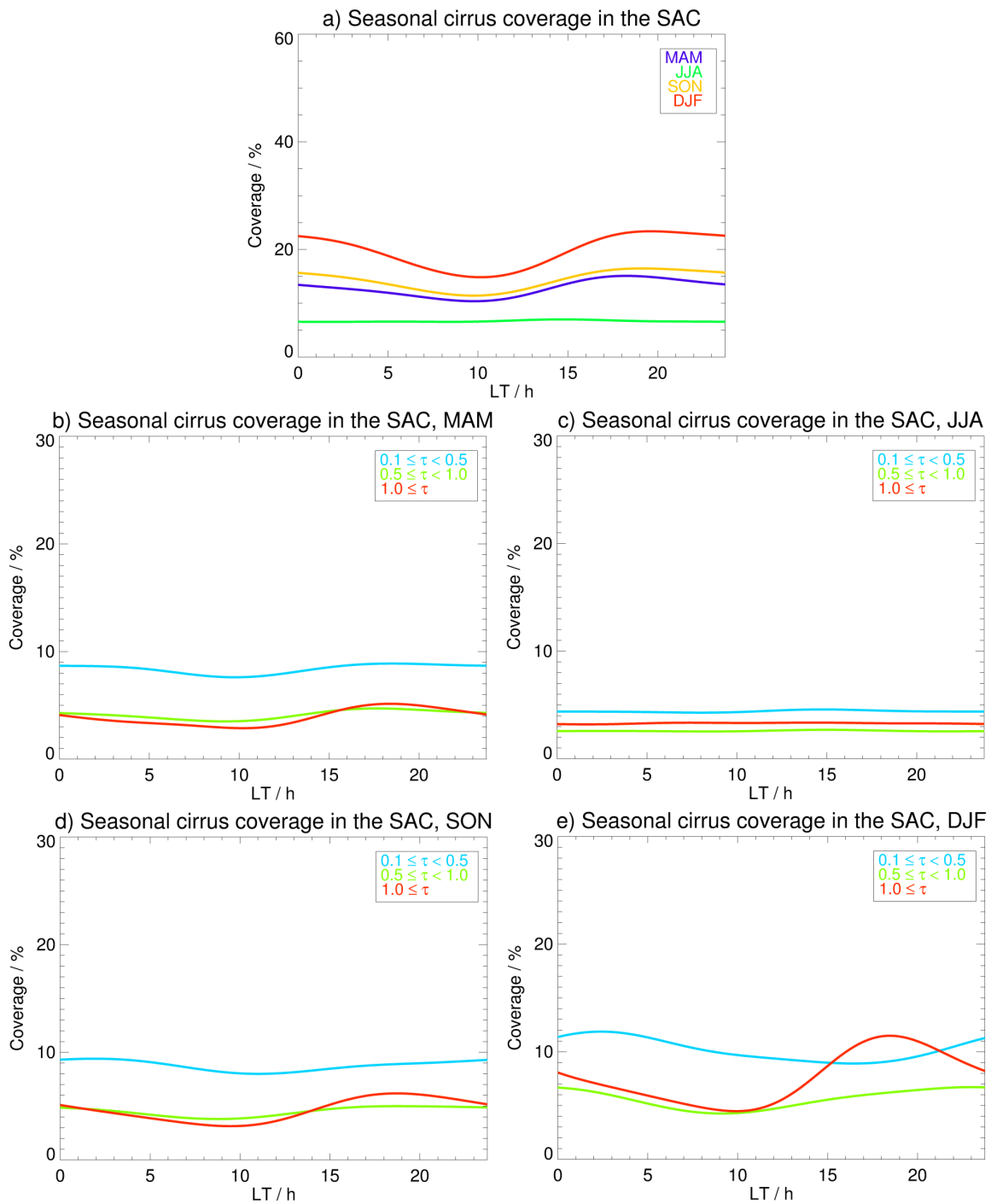


Figure 5.5: a: Seasonal total cirrus cloud coverage in the SAC region, color coded: MAM (blue), JJA (green), SON (yellow), and DJF (red). b-e: Seasonal cirrus coverage split in different classes of ice optical thickness for MAM (b), JJA (c), SON (d), DJF (e).

5.1.2.3 Seasonal cirrus coverage in SAR2

In MED and SAC evidence of convective influence on cirrus cloud coverage over land and ocean was presented. In the other regions with no land masses, a pure and undisturbed diurnal cycle of cirrus cloud coverage can be found without orographic influence on the formation and decay of cirrus clouds. Therefore the seasonal diurnal cycles of the SAR2 region is plotted in Fig. 5.6a.

All seasons show curves with two maxima and two minima. The maxima are detected in the morning between 05:00 and 07:00 LT and between 17:00 and 19:00 LT. Cirrus coverage in the SAR2 is largest in the southern hemispheric winter (JJA) with up to 47 % followed by spring (SON) with 45 % and autumn (MAM) with up to 38 %. The minimum coverage is reached in summer (DJF), when cirrus clouds cover only 33 % of this region. Compared to regions like MED and SAC, which show strong positive changes in the diurnal cycles caused by convection in the afternoon especially in summer, the SAR2 provides high seasonal changes of total cirrus coverage, but only small diurnal variations of 2 – 4% with similar curve shapes. In Fig. 5.6b-e the diurnal cycle of the three cirrus classes is depicted showing the semidiurnal structures for the four seasons (MAM, JJA, SON, and DJF), Fig. 5.6a.

During MAM (Fig. 5.6b) thin cirrus coverage shows high coverage with two maxima (24 %) at 06:00 and 18:00 LT and two minima (23 %) at 00:00 and 14:00 LT. Medium thick cirrus coverage is found to have two maxima (12 %) at 06:00 and 18:00 LT and two minima (11 %) at 00:00 and 11:00 LT. Thick cirrus coverage has only small values in MAM (~ 5 %), when no clear diurnal cycle is present.

The highest total cirrus cloud coverage is found in winter (JJA), Fig. 5.6c. Thin cirrus have a high fraction of the total coverage showing a diurnal cycle with two maxima (26 %) at 07:00 and 18:00 LT and two minima (25 %) at 02:00 and 13:00 LT. Medium cirrus coverage is also found with a slight diurnal cycle showing two maxima (17 %) at 06:00 and 17:00 LT and two minima (15 %) at 00:00 and 10:00 LT. In opposition, thick cirrus coverage shows a diurnal cycle with only one maximum (9 %) at 05:00 LT and one minimum (8 %) at 14:00 LT.

During southern hemispheric spring (SON), Fig. 5.6d, thin cirrus coverage varies again with two maxima (29 %) at 07:00 and 21:00 LT and two minima at 01:00 LT (28 %) and at 14:00 LT (27 %). Medium cirrus coverage again peaks at 05:00 and 17:00 LT with a value of 15 %. The two minima (14 %) are found at 00:00 and 11:00 LT. No clear diurnal cycle in the thick cirrus coverage is present with a coverage of 5 – 6 %.

The lowest cirrus cloud coverage in the SAR is detected in summer (DJF), Fig. 5.6e. Thin cirrus are found with a relatively strong diurnal cycle. Two maxima (24 %) at 06:00 and 20:00 LT are followed by two minima (22 – 23 %) at 00:00 and 14:00 LT. The same shape is found for the medium cirrus coverage, where two maxima (10 %) at 04:00 and 17:00 LT

are aligned with two minima (8 %) at 08:00 and 23:00 LT. Thick cirrus coverage shows only small variations with values of around 3 – 4 %.

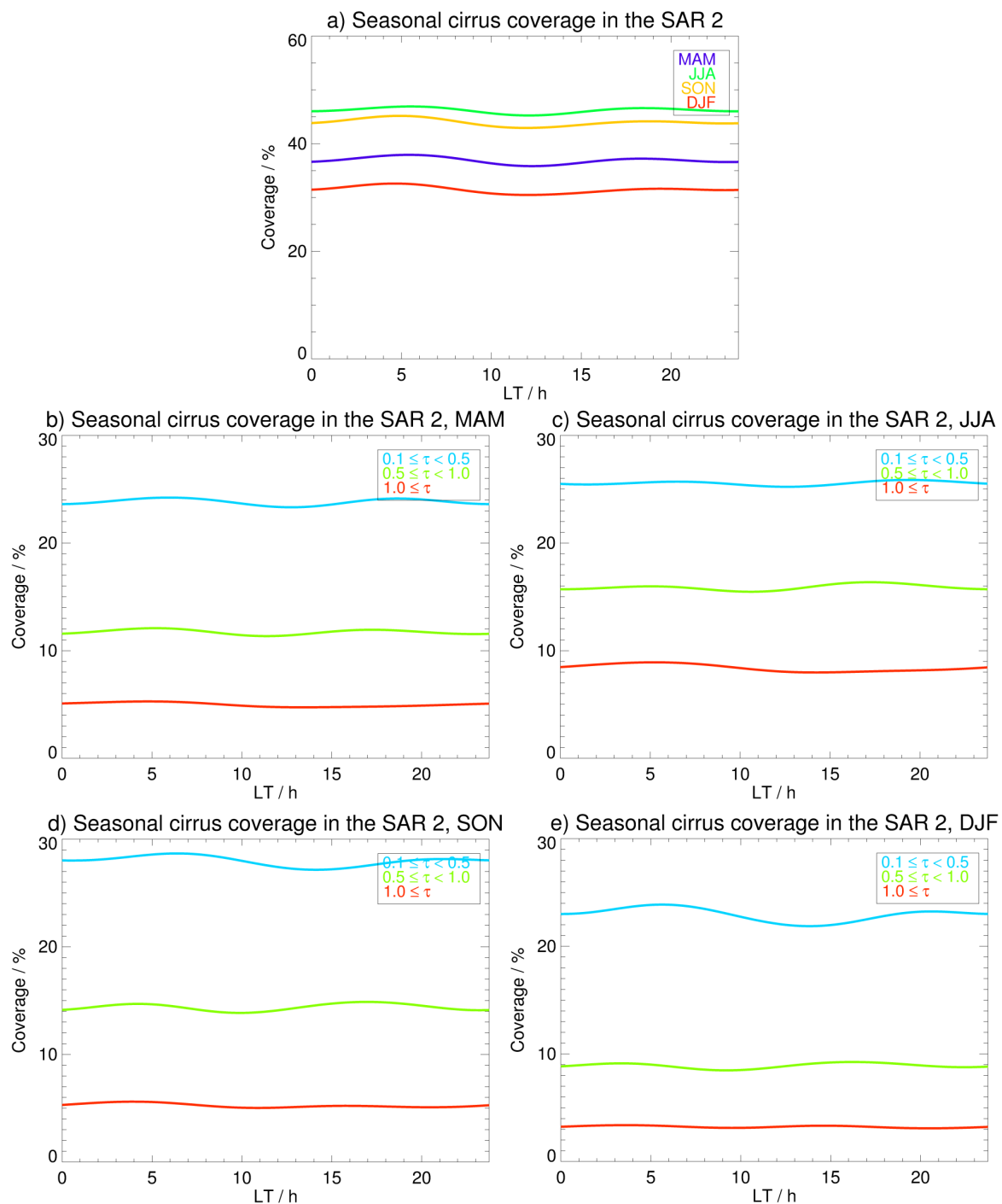


Figure 5.6: a: Seasonal total cirrus cloud coverage in the SAR2 region, color coded: MAM (blue), JJA (green), SON (yellow), and DJF (red). b-e: Seasonal cirrus coverage split in different classes of ice optical thickness for MAM (b), JJA (c), SON (d), DJF (e)

5.1.2.4 Seasonal cirrus coverage in SAR1

Since SAR2 covers a very large area with over 90° of longitude, another region in the South Atlantic was chosen to be directly comparable to the smaller area in the North Atlantic (NAR). Therefore, the coordinates of the NAR were just mirrored to the South Atlantic, resulting in the SAR1 region. The seasonal diurnal cycle of cirrus coverage in the SAR1 (Fig. 5.7a) is in very good agreement with the shapes of the seasonal curves in the SAR2 (Fig. 5.6a)

Again, the semidiurnal cycle with two maxima and two minima is found for all seasons. The minima and maxima are reached at the same times for each season as in SAR2. The southern hemispheric winter (JJA) shows the highest cirrus coverage with values up to 45 %. In SON and MAM the value of cirrus cloud coverage is lower. The coverage reaches up to 39 % in SON and 38 % in MAM. The lowest cirrus coverage is detected in southern hemispheric summer (DJF) with maximum values of 33 %. A direct comparison with the seasonal cirrus coverage in Fig. 5.6 shows, that the coverage in both South Atlantic regions (SAR1 and SAR2) is almost similar for MAM and DJF, but shows differences of up to 5 % for the JJA and SON, while the shape of the curve remains unchanged.

The seasonal diurnal cycle of the three different cirrus classes is once again depicted in Figure 5.7b-e. In the southern hemispheric autumn (MAM), Fig. 5.7b, thin cirrus coverage is present with 22 – 23 %. The shape of the curve shows two maxima at 08:00 and 23:00 LT and two minima at 00:00 and 14:00 LT. Medium cirrus clouds cover the SAR1 with two maxima (12 %) at 05:00 and 17:00 LT and two minima (10 %) at 00:00 and 10:00 LT. For thick cirrus slight but still detectable differences in coverage during the day are found. One maximum (7 %) is detected at around 05:00 LT, followed by a minimum (6 %) at 12:00 LT.

During the winter months (JJA) an almost homogeneous thin cirrus coverage is found in Fig. 5.7c, which varies between 22 – 24 %. Medium cirrus coverage shows two maxima (14 %) at 06:00 and 17:00 LT and two minima (12 %) at 00:00 and 10:00 LT. Thick cirrus clouds have their highest coverage (12 %) at 06:00 LT and their minimum (10 %) at around 14:00 LT.

The SON season (Fig. 5.7d) again provides the semidiurnal cycle of cirrus clouds for all three classes. Thin cirrus coverage shows two maxima (24 %) at 07:00 and 20:00 LT and two minima (22 %) at 00:00 and 14:00 LT. A similar shaped curve is detected for medium cirrus. Two minima (12 %) at 00:00 and 10:00 LT are followed by two maxima (13 %) at 04:00 and 17:00 LT. With only low changes in coverage, thick cirrus forms two maxima (7 %) as well as two minima (6 %). The first maximum here is found at 04:00 LT, followed by the first minimum at 10:00 LT, the second maximum at 16:00 LT, and another minimum at 23:00 LT.

As mentioned, the lowest seasonal cirrus coverage is found in summer (DJF), Fig. 5.7e,

with another semidiurnal cycle. Thin cirrus undergoes changes with two maxima (22 %) at 06:00 and 21:00 LT and two minima (20%) at 00:00 and 14:00 LT. Medium cirrus show maxima (10%) at 04:00 and 16:00 LT, and two minima (9 %) at 00:00 and 08:00 LT. Only small variations are finally found for thick cirrus clouds forming a coverage of 5 – 6 %. Overall the SAR1 shows lower seasonal values for cirrus coverage compared to the SAR2. The splitting in the single cirrus classes shows, that especially thin and medium cirrus clouds contribute highly to these difference, while thick cirrus clouds both regions with similar amounts.

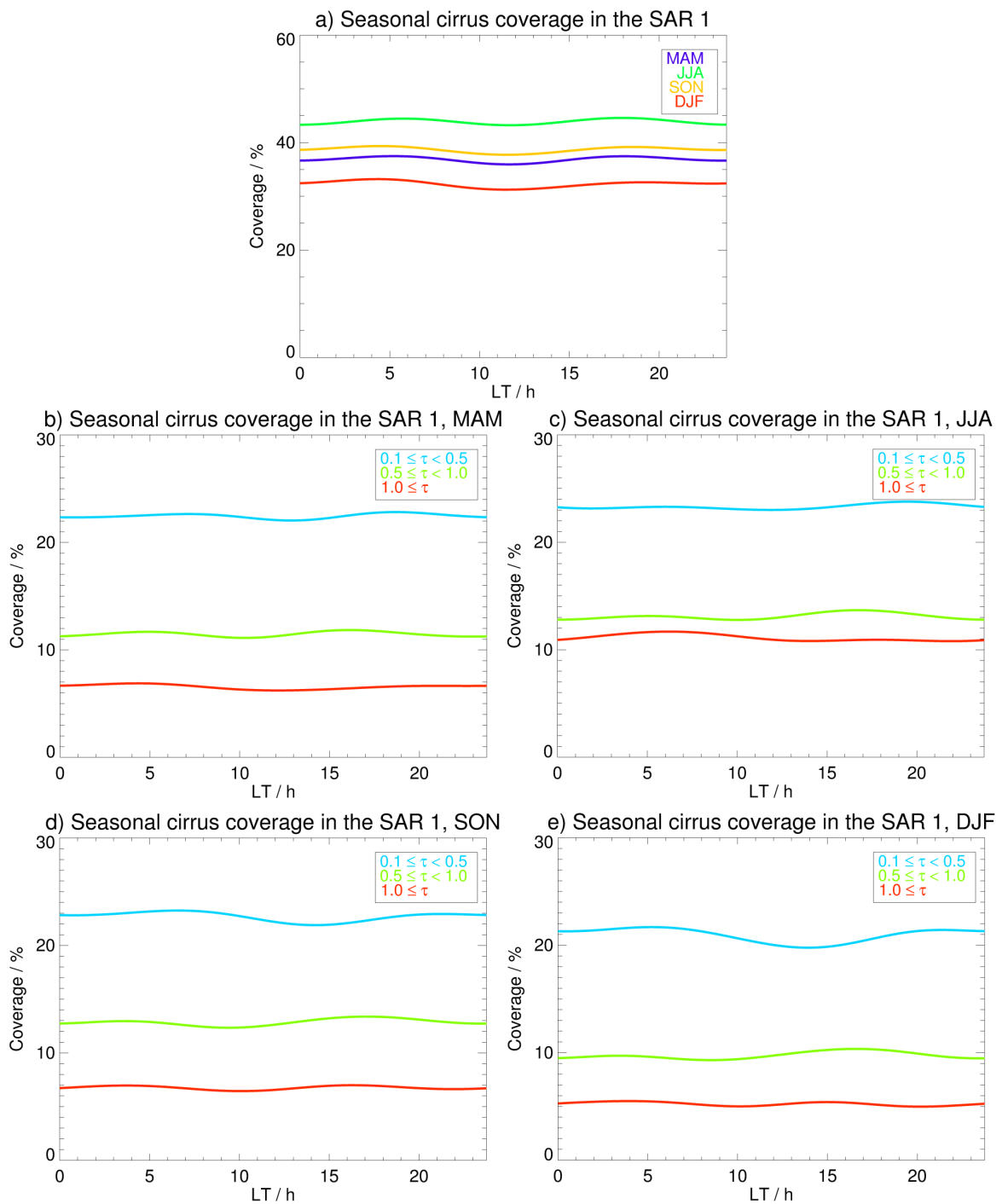


Figure 5.7: a: Seasonal total cirrus cloud coverage in the SAR1 region, color coded: MAM (blue), JJA (green), SON (yellow), and DJF (red). b-e: Seasonal cirrus coverage split in different classes of ice optical thickness for MAM (b), JJA (c), SON (d), DJF (e)

5.1.2.5 Seasonal cirrus coverage in NAR

The NAR has differences and similarities compared to the SAR1 and SAR2 region. On the one hand, neither convective nor orographical influence is present similar to the South Atlantic, on the other hand, the North Atlantic air corridor is located in exactly this region. During the early morning in this region at around 06 UTC, flights leave the American continent heading towards Europe. In the afternoon a second “wave” of airplanes passes the North Atlantic on their way from Europe to the USA [Graf et al., 2009].

As expected cirrus formation in the NAR (Fig. 5.8a) undergoes similar seasonal dependencies compared to the South Atlantic regions. We find the highest cirrus coverage in winter (DJF), while the lowest values are reached in the summer season (JJA).

In DJF, the first maximum is found at 07:00 LT with a coverage of 50 % followed by the first minimum (48 %) at 11:00 LT. After a slight increase a second maximum is reached at 16:00 LT (50 %) in combination with a second minimum (again 48 %) at 22:00 LT.

During spring (MAM) and autumn (SON) very similar ranges of cirrus coverage of around 37 % to 40 % are found, following similar diurnal cycles. The minima are reached at 10:00 and 22:00 LT, while the maxima are located at 06:00 and 17:00 LT. During MAM the second peak of the curve appears to have a greater amplitude. The lowest cirrus coverage in the NAR is detected in the northern hemispheric summer (JJA), where minima and maxima in the diurnal cycle are shifted to earlier times. The first and second maximum are found at 05:00 and 16:00 LT respectively. Both minima are reached at around 10:00 and 20:00 LT.

During spring (MAM), Fig. 5.8b, thin cirrus clouds show a semidiurnal cycle in their coverage with maxima of 27 % at 06:00 and 19:00 LT and minima of 25 % at 00:00 and 12:00 LT. Medium cirrus clouds are also present with a semidiurnal cycle with two maxima and minima. In the medium cirrus coverage, the first maximum (11 %) is found at 05:00 LT and the second one (12 %) at 16:00 LT. The two minima (9 %) are located at 09:00 and 22:00 LT. Thick cirrus clouds form a low coverage in the NAR with a coverage of around 4 – 5 %.

In summer (JJA), Fig. 5.8c, thin cirrus cloud cover the region with a maximum of 25% at around 05:00 LT and a minimum (23 %) at 14:00 LT. Medium cirrus show a maximum (9 %) at 04:00 LT and a stronger peak (10 %) at 16:00 LT. The two minima (6 %) are reached at 09:00 and 22:00 LT. Thick cirrus coverage undergoes no clear diurnal cycle with values of 3 – 4 %.

In SON, Fig. 5.8d, thin cirrus reaches two maxima (25 %) at 06:00 and 17:00 LT and two minima (23 – 24 %) at 00:00 and 12:00 LT. Medium cirrus coverage has two maxima (11 %), a first one at 05:00 LT and a second one at 15:00 LT. The maxima are followed by two minima (9 %) at 09:00 and 22:00 LT. The thick cirrus spectrum covers the NAR with a low variance in the diurnal cycle with values of 5 – 6 %.

In DJF, Fig. 5.8e, thin cirrus clouds show no clear diurnal cycle with values of around 26 %. For medium cirrus cloud coverage a semidiurnal cycle with two maxima (16 %) at 06:00 and 16:00 LT is detected again. These are followed by two minima (15 %) at 10:00 and 22:00 LT. Thick cirrus cloud coverage shows a different diurnal cycle, where a maximum (11 %) is present at 05:00 LT in combination with a minimum (9 %) at 14:00 LT.

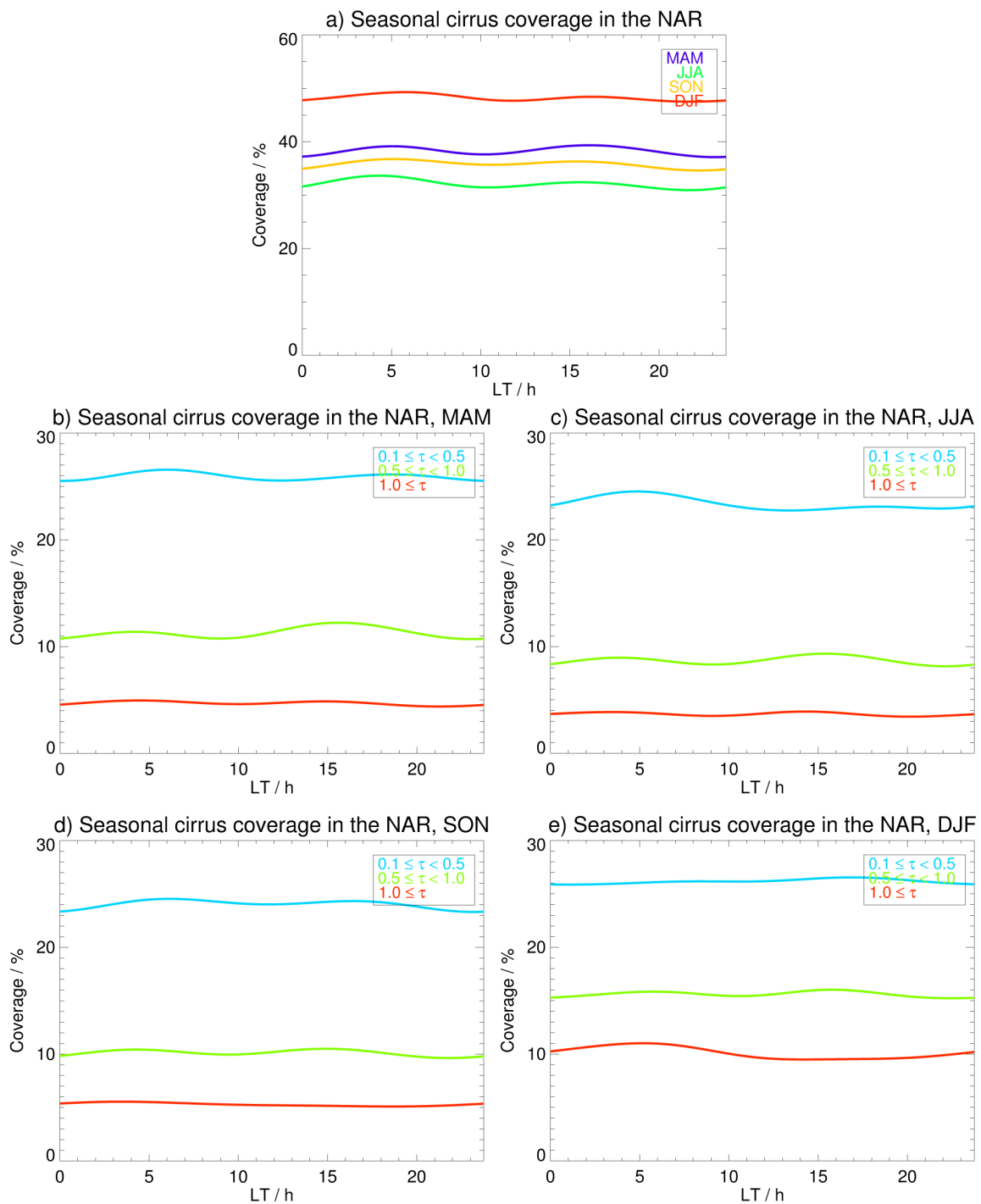


Figure 5.8: a: Seasonal total cirrus cloud coverage in the NAR region, color coded: MAM (blue), JJA (green), SON (yellow), and DJF (red). b-e: Seasonal cirrus coverage split in different classes of ice optical thickness for MAM (b), JJA (c), SON (d), DJF (e)

5.2 Cirrus Optical thickness

In the validation with the spaceborne lidar CALIPSO (Section 4.1.1) and the airborne HSRL (Section 4.1.2) low errors and standard deviations were found. The mean cirrus ice optical thickness (IOT) of the cirrus cloud is now calculated for the same period of COCS data from January 2006 to December 2010 similar to the coverage in Section 5.1. Here, this mean IOT is defined as the averaged value of the IOT of all cirrus covered and cirrus-free pixels in the specific regions. In order to retrieve this mean optical thickness the same spatial resolution of $0.25^\circ \times 0.25^\circ$ as for the coverage calculations is chosen in combination with the high temporal resolution of 15 minutes to depict diurnal cycle.

5.2.1 Convective regions

COCS detects a diurnal cycle dominated by convection for the two regions, MED and SAC. For the SAC region the mean ice optical thickness of cirrus clouds is found to reach its maximum at around 15:00 LT with $\tau_{max} = 0.13$ (Fig. 5.9, yellow). Its minimum is located at 07:00 LT with $\tau_{min} = 0.06$. Between minimum and maximum a very steep increase of the mean ice optical thickness is observed. After the maximum in the afternoon is reached τ decreases during evening and night until its minimum.

The MED region shows a different diurnal cycle (Fig. 5.9, red) with a maximum of $\tau_{max} = 0.14$. These high values are found at 16:00 LT until the evening. Afterwards the ice optical thickness decreases slowly until its minimum at 10:00 LT with $\tau_{min} = 0.12$. During the morning τ raises again.

So, differences between both regions occur in the comparison of the mean ice optical thickness. In the MED region the maximum of the mean ice optical thickness is reached earlier than in the SAC region. The MED region also shows a generally lower mean ice optical thickness for the whole diurnal cycle. In the SAC region a steeper increase of τ after the minimum is observed compared to the MED, while the decrease during night is shallower than in the MED region.

5.2.2 Non-convective regions

As seen in Section 5.2.1, such as MED and SAC, are to some extent dominated by local features forming cirrus clouds, especially convective systems with large anvil cirrus clouds reaching their maximum ice optical thickness in the afternoon formed by cirrus clouds with high ice optical thickness.

In contrast to this diurnal cycle, this section shows, that the semidiurnal cycle in the cirrus coverage of the three regions NAR (Fig. 5.10, green), SAR1 (Fig. 5.10, black), and SAR2 (Fig. 5.10, blue) is also found in the values of mean cirrus ice optical thickness. In Fig. 5.10 the mean ice optical thickness is plotted for these three regions. In the Southern

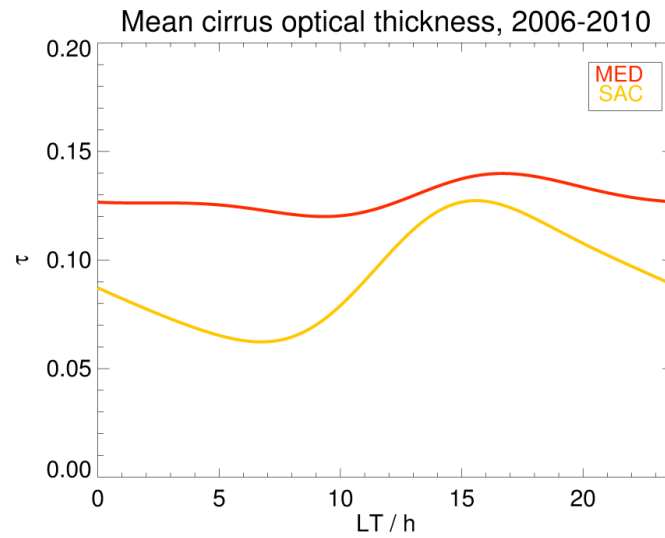


Figure 5.9: Mean ice optical thickness at a 15 min temporal resolution in the convective dominated regions MED (red) and SAC (yellow).

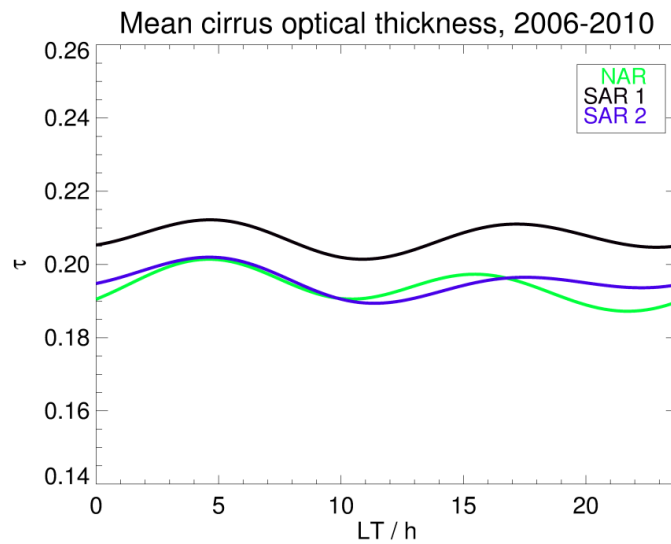


Figure 5.10: Mean ice optical thickness at a 15 min temporal resolution in areas with homogeneous surface. Following regions are plotted here: NAR (green), SAR1 (black), and SAR2 (blue).

Atlantic regions (SAR1 and SAR2) the diurnal cycles of the ice optical thickness follows a similar shape as the coverage in Fig. 5.7 and 5.6.

In SAR1 region we find the first maximum at 04:00 LT ($\tau_{max_1} = 0.215$) and the second at 17:00 LT ($\tau_{max_2} = 0.215$), which are followed by two minima at 11:00 LT ($\tau_{min_1} = 0.20$) and 23:00 LT ($\tau_{min_2} = 0.205$).

In the larger South Atlantic region, SAR2, the shape of the diurnal cycle differs only slightly from the smaller SAR1 region with an offset of $\Delta\tau = 0.01$. Almost no variations in the location of maxima and minima are observed.

In NAR, the COCS algorithm again detects a diurnal cycle with two maxima and two minima. Two maxima are found at 05:00 LT and at 15:00 LT, both with values of $\tau_{max} = 0.20$. A first minimum is located at 10:00 LT with $\tau_{min_1} = 0.19$, while a second minimum is found at 21:00 LT with $\tau_{min_2} = 0.185$. Compared to the South Atlantic regions, similar local times are found for the first part of the diurnal cycle, while the second part differs. In fact, the temporal interval between the first maximum and minimum is reduced to five hours similarly to the distance between the first minimum and the second maximum, while the second minimum follows the second maximum after six hours. The second maximum of the NAR curve occurs at 15:00 LT (two hours earlier than in the South Atlantic regions). The second minimum here is detected at around 21:00 LT again with a time shift of around two hours. The difference between SAR1 and NAR is explained later by the large coverage of very thin cirrus clouds in the NAR compared to SAR1 (Section 5.4).

5.3 Intercomparison with ECMWF

In order to exemplify the capability of the presented diurnal cycles of cirrus clouds to validate climate models the mean cirrus coverage derived by COCS retrieved for 2010 is now compared to the latest operational forecast model of the European Center for Medium range Weather Forecast (ECMWF), the Integrated Forecast System (IFS cycle 36r1, 36r2, and 36r4). In general, the ECMWF forecasts cover the time period from July 1985 to the present. In September 2006 a new feature, ice supersaturation in the upper troposphere, was included in the IFS [Tompkins et al., 2007]. This new feature produced some changes in the statistics of upper tropospheric humidity and cloud coverage. In particular, there is an increase in upper-tropospheric humidity and a decrease in high-level cloud coverage and cloud ice amounts.

The ECMWF provides global weather forecasts twice daily (00:00 and 12:00 UTC) with output time steps of three hours for the first three days. The model uses a resolution of about 25 km at the equator and a vertical resolution of about 15 hPa.

Lamquin et al. [2009] stated, that ECMWF uses an assimilation scheme that does not

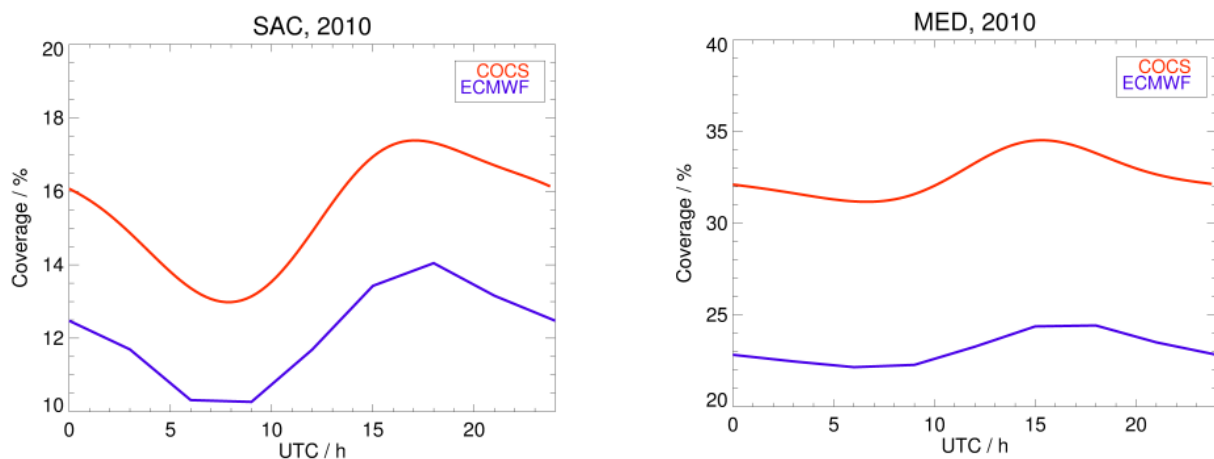


Figure 5.11: Cirrus coverage retrieved by COCS (red) and high cloud coverage of ECMWF IFS (blue) for the two convective dominated regions SAC (left) and MED (right).

account for ice supersaturation in the upper troposphere. Hence, data assimilation leads to analyses that underestimate the true occurrence and range of ice supersaturation. Since the analyses serve as initial conditions for the forecast runs, the forecast model needs some time for spinup of the supersaturation field. Studies of upper tropospheric humidity should not use forecast humidity data from the spinup phase since they are unreliable. This initial study of the global supersaturation spinup behaviour shows that at least twelve hours are necessary before the model forecasts humidity correctly and thus cloud data in the upper troposphere. Therefore, the IFS high cloud coverage forecasts of the ECMWF operational data archive for the year 2010 are used with a spinup time of

48 hours for the forecasts.

Of course the temporal resolution of three hours cannot show all details of the diurnal cycle retrieved by COCS with 15 min resolution, but it gives a first hint on whether the cloud coverage calculated by the ECMWF shows similar structures. Please note that ECMWF IFS and COCS data are now analysed as a function of UTC and no longer as a function of LT.

Again the regions dominated by convection, SAC and MED, are depicted first (Fig. 5.11). On the left, the plot shows the two curves of the cirrus coverage retrieved by COCS for SAC (red), and the high cloud coverage retrieved from ECMWF IFS forecasts (blue) for the same region. COCS calculates a slightly higher cirrus coverage ($\sim 3\%$), but both curves show a similar diurnal cycle with the convective maximum in the late afternoon between around 17:00 to 18:00 UTC and the minimum in the morning (at around 08:00 UTC). On the right, the MED region shows higher differences in the detected coverage. COCS detects around 9% more cirrus clouds. Nevertheless, both algorithms represent a similar diurnal cycle with less variations than in the SAC region, and again a maximum dominated by convection between 15:00 and 17:00 UTC is found, while the minimum is also found in the morning at around 08:00 UTC.

In the two Southern Atlantic regions, SAR1 and SAR2, the cirrus coverage is present

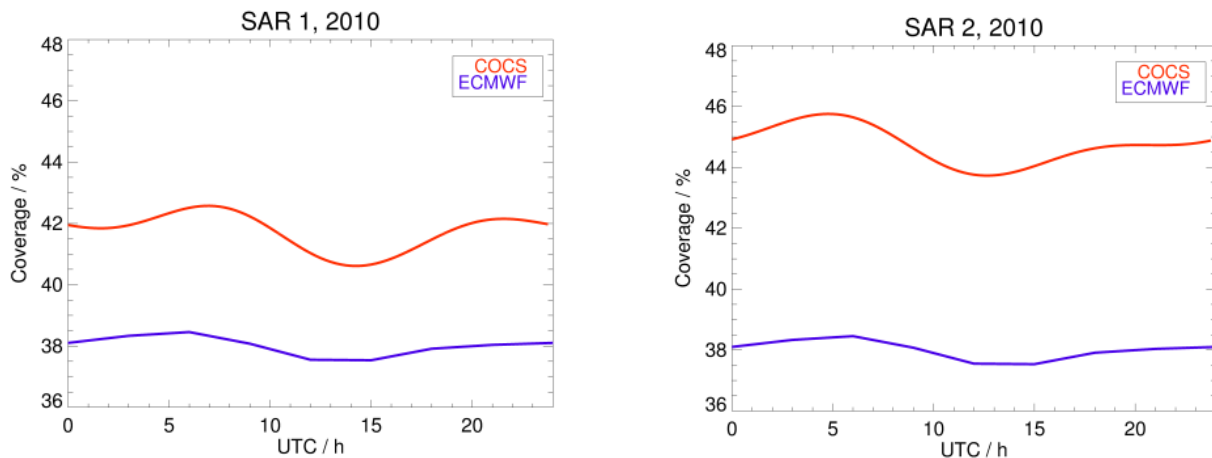


Figure 5.12: Cirrus coverage retrieved by COCS (red) and high cloud coverage of ECMWF IFS (blue) for the two South Atlantic regions SAR 1 (left) and SAR 2 (right).

with no or very low influence of convection and without the influence of air traffic as it is the case in NAR. The cirrus coverage of both regions is depicted in Fig. 5.12. On the left, the smaller region SAR1 show the double-wave frequency in the cirrus coverage detected by COCS with two minima (at 02:00 and 14:00 UTC) and two maxima (at 07:00 and 21:00 UTC). The ECMWF shows slightly less cirrus coverage ($\sim 3 - 5\%$) and follows the diurnal cycle detected by COCS in case of the first maximum in the morning and the second minimum in the afternoon, but it misses the second maximum in the late evening

and the first minimum shortly after midnight.

A larger difference in cirrus coverage is found for the bigger South Atlantic region, SAR2, on the right of Fig. 5.12. COCS detects an around 7 % higher cirrus coverage, but the diurnal cycle is present in the ECMWF forecast as well as in COCS, but shows less variations in the time after the minimum at 12:00 UTC. ECMWF and COCS detect a maximum cirrus coverage at around 05:00 to 06:00 UTC.

Fig. 5.13 depicts cirrus coverage from the ECMWF forecasts and COCS for NAR. While

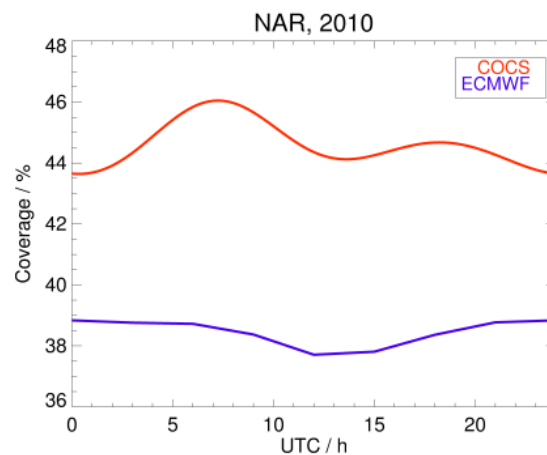


Figure 5.13: Cirrus coverage retrieved by COCS (red) and high cloud coverage of ECMWF IFS (blue) for the North Atlantic region NAR.

the value of cirrus coverage generally shows an offset of 4–5 % at around midnight, COCS detects significantly more cirrus coverage with a strong diurnal cycle. Two maxima at 07:00 and 19:00 UTC are present with coverage up to 46 % and 45 % respectively. The minima in cirrus coverage are located at 00:00 (43.5 %) and 13:00 UTC (44 %). The ECMWF forecast shows one maximum at midnight with 39 % high cloud coverage and one minimum at 12:00 UTC with 38 %.

In summary, the natural cirrus coverage forecasted by the ECMWF and its diurnal cycle is well represented in the cirrus coverage retrieved by COCS. In general COCS overestimates the cirrus coverage or the IFS underestimates the high cloud coverage. Only NAR, which is strongly influenced by air traffic due to the North Atlantic air corridor, shows a strongly modified diurnal cycle.

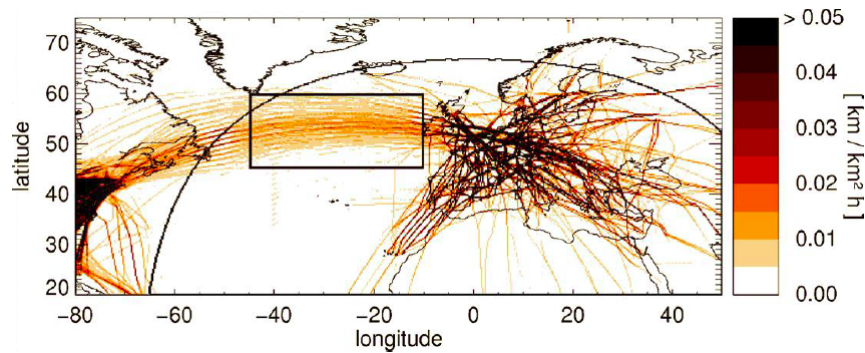


Figure 5.14: Mean air traffic density in Europe and the North Atlantic for the NAR region is marked by the solid black box. The black thick curve represents the 75° satellite zenith angle of MSG-8/9 [Graf et al., 2009].

5.4 Differences between North and South Atlantic Region

In this chapter some first hints on the influence of air traffic on the diurnal cycle of cirrus cloud coverage and cirrus optical properties were already found. The two regions, SAR 1 and NAR, are now compared to each other in order to give a better overview on the differences in regions. During the ESA-DUE Project CONTRAILS, the European Air Traffic Control (EUROCONTROL) provided a dataset of air traffic density (ATD) for six weeks in 2004 with a temporal resolution of 15 minutes and a spatial resolution of $0.25^\circ \times 0.25^\circ$, depicted in Fig. 5.14. Based on this dataset a representative diurnal cycle of ATD in the NAR was found in Graf et al. [2009], where a peak in ATD is present for the eastbound transatlantic flights at 04:00 UTC and another one at 13:00 UTC representing the westbound traffic. In this section some influence of air traffic on natural cirrus development and coverage is shown leading to changes in formation and decay of cirrus clouds, and therefore resulting in a modified diurnal cycle of cirrus ice optical thickness. Until now the aim of this thesis was to find the natural diurnal cycles in coverage and ice optical thickness of cirrus clouds, but since COCS is able to detect thin cirrus clouds, such as contrail cirrus clouds produced by air traffic.

As seen in Sections 5.1.2.4 and 5.1.2.5 both regions show diurnal cycles of cirrus coverage with two minima and two maxima. In the following the differences between the NAR and SAR1 are discussed and plotted together with the ATD for the year 2004. In Fig. 5.15 two different curves are depicted. The first, coloured in black, is the difference of the total cirrus coverage, $\Delta_{\text{cov}} = \text{cov}(\text{NAR}) - \text{cov}(\text{SAR1})$, which varies highly and is positive, indicating the higher cirrus coverage in the NAR. At 05:00 LT this difference reaches a first maximum with values of $\Delta_{\text{cov}} = 1.0\%$ and second maximum at 14:00 LT with $\Delta_{\text{cov}} = 1.5\%$. Between both maxima only a small decay of cirrus clouds is detected,

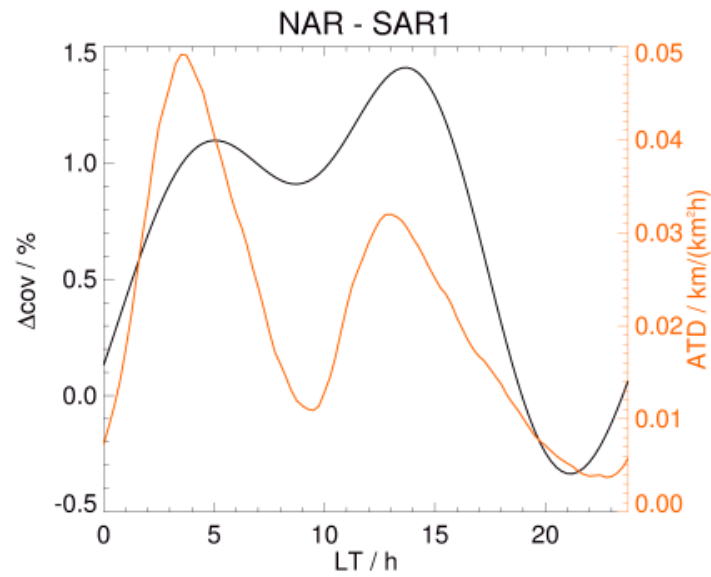


Figure 5.15: Difference of total cirrus cloud coverage in NAR and SAR1 at 15 min temporal resolution (black). Air traffic density plotted for the time period in 2006 (red).

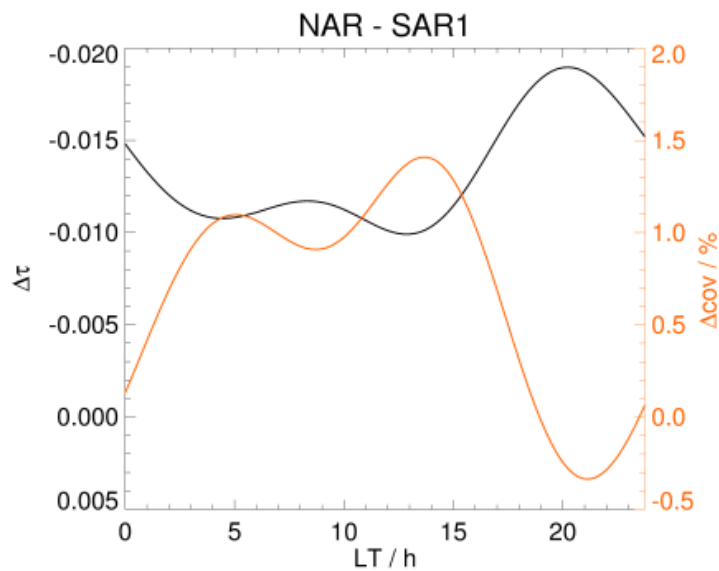


Figure 5.16: Difference of total ice optical thickness in NAR and SAR1 at 15 min temporal resolution (black). Difference of total cirrus cloud coverage in NAR and SAR1 at 15 min temporal resolution (red).

while a minimum is found at around 21:00 LT with a difference of only $\Delta_{\text{cov}} = -0.4\%$. Compared to the ATD, it appears that both peaks in the coverage difference follow the maxima in the ATD, which are located at 03:30 LT and around 13:00 LT. Between the first maximum in ATD and the first maximum in cirrus coverage a time shift of 1 to 1.5 hours is present. The second maximum in coverage follows the second peak in ATD with a shift of more than one hour. After this second peak, Δ_{cov} decreases to its minimum while the air traffic reaches its minimum between 22:00 and 23:00 LT. Differing from this minimum the coverage difference starts to increase already after 21:00 LT.

In Fig. 5.16 the difference in the cirrus mean ice optical thickness, $\Delta\tau = \tau(\text{NAR}) - \tau(\text{SAR})$ is plotted in black together with the difference in cirrus cloud coverage Δ_{cov} in red. The cirrus optical thickness shows a different behaviour compared to the cirrus coverage here. The shape of the curve shows some congruent features to the cirrus coverage. A maximum difference of $\Delta\tau = -0.02$ is identified at 20:00 LT. Afterwards $\Delta\tau$ undergoes a decay until the early morning. A minimum difference of $\Delta\tau = -0.01$ is reached at 13:00 LT.

In summary two big differences between cirrus coverage and optical thickness have been found: While cirrus cloud coverage is significantly increased in NAR following the maximum density of air traffic, the ice mean ice optical thickness is slightly reduced. The first maximum in cirrus coverage leads to a lower difference, the second peak to an increase in the cirrus optical difference. During night, when the cirrus coverage difference reaches its minimum, $\Delta\tau$ has its maximum at 20:00 LT. While a generally higher coverage is found in the NAR, the mean ice optical thickness is lower compared to the SAR 1.

Thus the modification of cirrus cloud coverage and ice optical thickness might be due to air traffic and the produced contrail cirrus. Those contrail cirrus clouds are known to have low ice optical thickness, [Vazquez-Navarro et al., 2010, Meyer et al., 2002, Minnis et al., 2004]. When the maximum in cirrus coverage is reached during daytime, the differences in τ show only low values suggesting that especially thin cirrus clouds are formed, which in opposition might have an influence on the formation of “thicker” natural cirrus clouds. The maximum difference in ice optical thickness is reached, when both regions show an almost similar cirrus cloud coverage at night.

In order to finally summarize the difference in cirrus cloud coverage in both regions, especially thin cirrus clouds with an ice optical thickness of $0.1 \leq \tau < 0.5$ is of specific interest. As expected, the highest differences in the cirrus coverage are found for the class of thin cirrus clouds as mentioned above. Variations of up to 3% are found following the same diurnal cycle as the difference in total cirrus coverage (Fig. 5.15). Cirrus clouds with medium ice optical thickness show lower differences in coverage. While the coverage here shows a negative difference of down to -0.7% , a significant diurnal cycle is detected again with two maxima and two minima. Especially thick cirrus cloud coverage shows negative difference of up to -1.7% . The diurnal cycles of these three cirrus classes show some evidence on the influence of air traffic and especially thin cirrus clouds are obviously

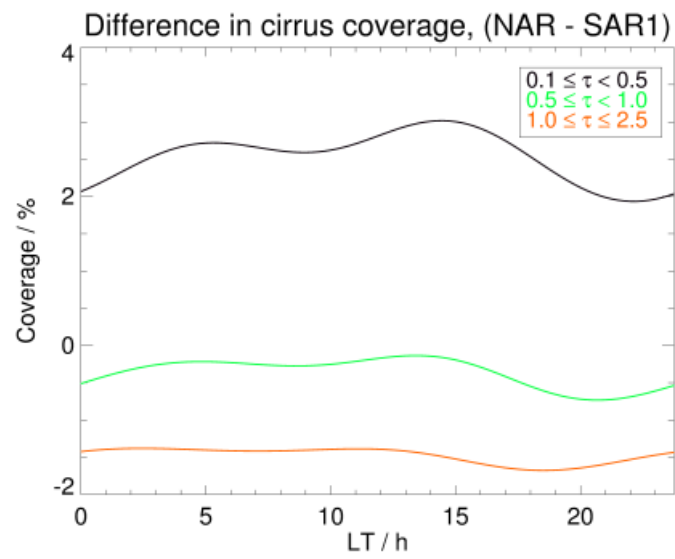


Figure 5.17: Differences in cirrus coverage for the three different classes of cirrus clouds. Low (black), medium (green), and thick cirrus clouds (orange), defined in Section 5.1.1.

increased.

Chapter 6

Discussion

6.1 Method

COCS is a new algorithm to retrieve the ice optical thickness and top altitude of cirrus clouds exploiting the high sensitivity and accuracy of active remote sensing and the high temporal resolution and spatial coverage of geostationary passive remote sensing. Based on a backpropagation neural network, COCS is trained by coincident measurements of cirrus ice optical thickness and top altitude of CALIOP/CALIPSO and thermal infrared brightness temperatures of SEVIRI/MSG.

As introduced in Section 2.2.3, passive spaceborne remote sensors measuring atmospheric radiation at different visible and/or infrared wavelengths have been used ever since to detect clouds in general and to retrieve their properties. In order to retrieve the properties of detected cirrus clouds either parametrizations derived from in situ measurements or physical methods using optimization techniques and look-up tables are generally used. In many cases the retrieval of microphysical cirrus cloud properties utilizes the method developed by Nakajima and King [1990], which is based on the visible and near-infrared radiation spectrum. Therefore a nighttime retrieval of microphysical properties of i.e. cirrus clouds is not possible.

In opposition the COCS algorithm is able to retrieve cirrus ice optical thickness and top altitude during day and night by utilizing exclusively the thermal infrared channels of the geostationary SEVIRI instrument.

Due to its repeat cycle of 16 days and its narrow, CALIOP's temporal and spatial coverage is not sufficient to analyse diurnal cycles of cirrus clouds and their properties. COCS is applied on the measurements of SEVIRI with a temporal resolution of 15 min covering about one third of the Earth's atmosphere.

Since the training dataset of COCS is based on CALIOP, some specific properties of CALIOP have to be mentioned. In general CALIOP derives properties of aerosol layers and cirrus clouds with high accuracy and sensitivity (Section 2.3). However, the algo-

rithms to retrieve optical thickness of aerosols and clouds applied on the measurements of CALIOP are based on several assumption (e.g. lidar ratio), since it is no High Spectral Resolution Lidar (HSRL) causing uncertainties in the CALIOP data processing. Furthermore, the lidar signal gets totally attenuated in case of clouds with $\tau > 3 - 5$ [Winker et al., 2010], which limits CALIOP measurements to thin cloud layers. Therefore the retrieval of optical thickness by COCS is limited to values of up to $\tau = 2.5$, which is only exceeded by the algorithm in case of very strong convective systems forming cirrus anvils with high optical thickness.

The validation of COCS was proceeded with active and passive remote sensors (Section 4). On the one hand COCS was validated with the independent test dataset of CALIOP and the limited amount of measurements with an airborne HSRL. On the other hand COCS was compared to algorithms based on measurements of SEVIRI. Both showed high accuracy of the derived cirrus cloud properties in combination with high detection efficiencies. Nevertheless a lower detection limit of $\tau \geq 0.1$ had to be chosen in order to prevent high false alarm rates.

As suggested by this lower detection limit, COCS utilizes SEVIRI to detect thin cirrus cloud down to $\tau = 0.1$. Compared to other algorithms such as MeCiDA-2, COCS detects significantly more cirrus clouds, which is briefly shown in Section 4.2.1 and [Ostler, 2011].

6.2 Results

It is crucial for climate models to have accurate and detailed knowledge of the diurnal cycle of both, cirrus optical thickness and coverage, in order to calculate their radiative effect and their climate impact, since cirrus clouds evoke a cooling effect during daytime and a warming effect during night.

By applying the COCS algorithm to measurements of SEVIRI five years of data were processed at the high temporal resolution of SEVIRI. During the analysis of this dataset five different regions were chosen, two regions dominated by convective cirrus cloud formation and three non-convective regions.

6.2.1 Convective regions

Over the Mediterranean (MED) and South African (SAC) region a diurnal cycle in cirrus coverage peaking in the early afternoon is found. While the SAC (up to 16 %) has a generally lower cirrus coverage than the MED (up to 26 %), the diurnal cycle in the SAC shows a slightly stronger variability (Section 5.1.1). Sassen et al. [2008] showed, that for both regions, a combined algorithm using the CPR aboard CloudSat and CALIOP

aboard CALIPSO detects similar cirrus coverages.

By looking at the diurnal cycle of mean cirrus ice optical thickness, the differences between both regions get obvious (Section 5.2.1). A strong diurnal cycle is present in the SAC, where optically thick cirrus clouds are formed during the day with a maximum ice optical thickness in the afternoon similar to the coverage. In the MED only a slight increase in ice optical thickness is found.

Especially in the SAC convective cirrus cloud formation dominates the diurnal cycle of cirrus coverage and ice optical thickness. Initiated in the morning, strong convective cells grow during daytime in this regions forming optically thick anvils. In the afternoon and evening these anvils spread over wide areas resulting in high cirrus cloud coverage, while their mean ice optical thickness decreases especially during night (Section 2.1). The mean cirrus ice optical thickness in the MED shows significantly lower daily variability indicating that less convective influence is present.

For further investigations, the diurnal cycle of cirrus coverage was split into different classes and seasons. These analysis have shown, that on the one hand the MED is covered by a high percentage of thin cirrus clouds up to 22 % during the single seasons. In the SAC thin cirrus cloud coverage results in values of only up to 12 %. On the other hand, thick cirrus clouds in the SAC are found to have a higher variability in their diurnal cycle compared to the MED. Especially in the southern hemispheric summer, when the coverage of thick cirrus clouds increases rapidly during daytime, medium and thin cirrus clouds show an inverse diurnal cycle.

In Section 5.3 the cirrus cloud coverage derived by COCS is compared to the results of the operational forecast system IFS of the ECMWF for the year 2010. Even though the temporal resolution of three hours provided by the IFS is lower than the temporal resolution of COCS, the diurnal cycle is very good comparable. While the IFS and COCS retrieve an almost similar coverage in the SAC (only slightly more cirrus clouds (+3 %) are detected by COCS), the differences in MED are greater with almost +9 % higher coverage derived by COCS.

In order to summarize, the diurnal cycle of cirrus clouds in typical convective regions such as the SAC is dominated by convective cirrus clouds resulting in high ice optical thickness and very strong variability due to their formation and decay. Indeed a similar diurnal cycle of cirrus cloud coverage was found in the MED, but considering the diurnal cycles of mean ice optical thickness and seasonal coverage, the MED has a stronger influence of thin cirrus clouds compared to the SAC.

In a study utilizing the measurements of the Visible Infrared Spin Scan Radiometer (VISSR) Atmospheric Sounder (VAS) flown on the Geostationary Orbiting Environmental Satellites (GOES) covering the Northern and Southern American Continents, Wylie [2002] defined different regions covering different atmospheric regions to retrieve the diurnal cycle of cirrus cloud coverage and compared it to ISCCP data. This study found a

similar diurnal cycle over the Gulf Coast of the United States with a maximum at around 14:00 LT comparable to MED and SAC in this work. A similar diurnal cycle was also found over Central Brazil and the Southern Rocky Mountains. Of course these regions are not completely comparable to MED and SAC, but the results give confidence on the results of this work. Furthermore, Stubenrauch et al. [2006] analysed cloud properties and their seasonal and diurnal variability from the Television Infrared Observation Satellite-N (TIROS-N) Observational Vertical Sounder (TOVS) observations aboard the NOAA polar orbiting satellites. By utilizing different multispectral tests on the retrieved high cloud coverage is inter alia derived for different latitude bands at six different observation times per day. For atmospheric regions over northern hemispheric midlatitude land in example, a diurnal cycle of cirrus cloud amount during January was found to vary between 8 % and 12 %, while cirrus coverage during July varies between 12 % and 18 %. In Section 5.1.2.1 the diurnal cycle of cirrus coverage derived by COCS in the summer season JJA shows lower values (around 5 % to 10 %) with a similar amplitude. In opposition the total cirrus coverage derived by COCS during the northern hemispheric winter is almost four times higher than the values derived by TOVS. One reason for this deviation is caused by the high coverage of thin cirrus clouds (up to 25 %) detected by COCS. Secondly, one single month is not representative for the seasonal averaged diurnal coverage presented in this work. Overall the convective dominated diurnal cycle of cirrus coverage is also present in the TOVS results.

For southern hemispheric midlatitude bands, the diurnal cycle of cirrus cloud amounts derived by TOVS is very similar to the seasonal cirrus coverage presented in Section 5.1.2.2. While the southern hemispheric summer is dominated by a maximum in the afternoon, the southern hemispheric winter shows no significant diurnal cycle in both cases. While the COCS retrieves a cirrus coverage of around 7 % in JJA, TOVS detects a cirrus amount of 12 – 14 %. Bergman and Salby [1996] analysed seven years of ISCCP data from 1984 to 1990 and found the strongest diurnal cycles in high cloud coverage over land in the Tropics similar to Wylie [2002]. Soden [2000] also found a very comparable diurnal cycle in the upper troposphere in the Tropics. However, the retrieval of the ice optical thickness of cirrus clouds such as convective initiated cirrus clouds with COCS is limited due to the restrictions described above. With a maximum cirrus ice optical thickness of $\tau = 2.5$ COCS underestimates the ice optical thickness of anvils above cumulonimbus clouds as well as frontal cirrus clouds. In example, Fierli et al. [2008] found a cirrus optical thickness over Brazil of up to $\tau = 100$ in a strong convective system with a light-weight microlidar and water vapour measurements on-board a stratospheric balloon during the HIBISCUS 2004 campaign, while Meyer [2004] analyzed a single convective initiated cirrus clouds and found an ice optical thickness of up to $\tau = 3.0$ by utilizing the visible and near-infrared channels of MODIS. Sassen and Comstock [2001] combined groundbased lidar and mid-infrared radiometer measurements, which were collected between 1992 and 1999

from visually identified cirrus clouds and used to retrieve their optical depth. Different categories of cirrus clouds were investigated. For example, mid-latitude anvils of strong convective clouds were retrieved with $\tau = 0.946 \pm 0.68$. Due to this large range of retrieved optical thickness in situations with strong convection and/or thick cirrus clouds it is obvious, that the retrieval ice optical thickness in regions such as SAC is difficult. Furthermore, the mean cirrus optical thickness used in this work is the averaged value for the whole region also accounting for cirrus-free pixels.

In case of the MED the mean cirrus ice optical thickness with values of around $\tau = 0.14$ is quite in the range of the results of Giannakaki et al. [2007], where a mean optical thickness of $\tau = 0.31 \pm 0.24$ was measured by a ground based lidar in Thessaloniki, Greece. Here, also thick cirrus clouds formed by cumulonimbus clouds and frontal systems are likely to be underestimated by COCS.

6.2.2 Non-convective regions

In contrast, three maritime regions, the North Atlantic (NAR) and the South Atlantic regions (SAR1 and SAR2) were chosen to retrieve information on diurnal cycles of cirrus clouds in regions with no landmasses, where convection is less present. Cirrus clouds are found to cover these regions with significantly higher percentage and a semidiurnal cycle compared to MED and SAC. While SAR1 shows a cirrus coverage of up to 39 %, the SAR2 follows the same diurnal cycle with a slight offset of 1 % with two maxima (05:00 and 18:00 LT) and two minima (00:00 and 11:00 LT). In the NAR a coverage of up to 40 % is found, but there the diurnal cycle differs and is shifted with two maxima at 05:00 and 15:00 LT and two minima at 10:00 and 22:00 LT.

Wylie [2002] found a similar diurnal cycle in cirrus cloud coverage over the Western Tropical Atlantic with two maxima and two minima by using the VAS aboard the GOES satellites with a coverage between 13 % and 21 % for two months in summer 1988. Graf et al. [2009] found cirrus clouds to cover the NAR with about 38 – 40 % with a similar semidiurnal cycle for the years 2004 to 2008 by applying MeCiDA-2 on the infrared brightness temperatures of SEVIRI.

The mean cirrus ice optical thickness derived for the SAR1 and SAR2 derived in this work shows similar diurnal cycles, while for the SAR1 values of $\tau = 0.21$ are derived compared to $\tau = 0.20$ for SAR2 in the larger SAR2.

As it is the case for convective regions only a few climatological studies on the mean ice optical thickness have been performed in the past. In Sassen and Comstock [2001], mid-latitude cirrus clouds were found to have an optical thickness of $\tau = 0.751 \pm 0.91$ from the groundbased lidar and mid-infrared radiometer measurements, but again the values derived in the framework of this thesis also account for non cirrus covered pixels.

In contrast to the differences in the diurnal cycle of cirrus coverage in the NAR compared to the South Atlantic regions, the mean ice optical thickness show a similar diurnal cycle with τ around 0.20. Based on first indications of the influence on cirrus cloud coverage in the NAR found by Graf et al. [2009], these differing diurnal cycles were further analysed in Section 5.4. In this work the diurnal cycle of air traffic density were compared to the diurnal cycle of cirrus cloud coverage and ice optical thickness. It was found, that the diurnal cycle of cirrus coverage in the NAR is on the one hand modified compared to the SAR1. On the other hand the mean cirrus ice optical thickness was found to be decreased by less than $\Delta\tau = -0.02$ compared to SAR1.

According to the results of the COCS algorithm, the differences between the NAR and the SAR1 is caused by an increased coverage by thin cirrus clouds (up to 3 %) and their influence on the formation of thick cirrus clouds (which are decreased by almost 1.5 %) in the NAR. This result agrees with the calculated ice optical thickness of contrails and contrail cirrus clouds in former studies. In Meyer et al. [2002] a mean optical thickness of linear contrails formed from the exhaust of aeroplanes in an ice supersaturated atmosphere was estimated to be 0.11 over Western Europe, while Minnis et al. [2004] derived a mean ice optical thickness of 0.2 over the USA. With growing age, these linear contrails loose their shape and their ice optical thickness increases, [Atlas et al., 2006]. In Vazquez-Navarro [2009] an automatic contrail tracking algorithm was developed to track contrails even when the linear shape is lost. The mean ice optical thickness of four month of data was calculated to have values between 0.57 and 1.18, which also accounts for the contrails that merge into pre-existing cirrus clouds with a higher optical thickness and generally detects optically thick contrails due sensitivity limitations.

The wide range of estimated optical thickness of contrails and contrail cirrus shows the difficulties of extracting the influence of aviation on the natural formation and decay of cirrus clouds, but the results presented in this work give some indications additional to Graf et al. [2009].

While the comparison of IFS and COCS for the convective regions showed good agreement in the diurnal variability of cirrus clouds, the maritime regions SAR1, SAR2, and NAR show significant differences (Section 5.3) in 2010. In all three regions higher cirrus coverage is detected by COCS. In the SAR1 the IFS calculations are exceeded by around 4 %, in the SAR2 and the NAR by up to 7 %. Beside the different values of cirrus coverage, the diurnal cycle detected by COCS is not present in the IFS forecasts. Additionally the amplitude in the maritime regions derived by COCS is greater than in the IFS. This might be caused by different reasons. One reason is the temporal resolution of the IFS, which cannot resolve all features of the diurnal cycle found by COCS. A second reason for the lower amplitude and the missing semidiurnal cycle of the cirrus coverage as detected by COCS is the missing influence of air traffic on cirrus formation and decay in the NAR. However, these reasons cannot explain the differing results in the South Atlantic regions,

where no influence of air traffic on the natural formation and decay of cirrus clouds is present. Thus, the model physics applied in the IFS are not able to forecast the observed diurnal cycle.

Earlier studies of tropical oceanic areas have indicated that diurnal cycles of cirrus clouds are driven more by radiative cooling of the cloud tops [Gray and Jacobson, 1977, Duvel, 1989, Chen and Houze, 1997] than the surface solar insolation, which drives the land diurnal cycles. Nevertheless, further analysis are needed to identify and to understand the physics behind these processes.

Chapter 7

Conclusions and outlook

In order to detect thin cirrus clouds at high temporal resolution, the Cirrus Optical properties derived from CALIOP and SEVIRI during day and night time (COCS) algorithm was developed as a new approach in geostationary passive remote sensing with a back-propagation neural network exploiting the capabilities of polar-orbiting active remote sensing. COCS utilizes the thermal brightness temperatures and brightness temperature differences measured by the Spinning Enhanced Visible and Infrared Imager (SEVIRI) aboard Meteosat Second Generation (MSG).

For the training of the neural network ice optical thickness and top altitude of cirrus clouds derived from the Cloud-Aerosol Lidar with Orthogonal Polarization (CALIOP) 05 km Cloud Layer product were used together with auxiliary datasets. As an essential task of the development of this new algorithm, a detailed validation with an independent dataset of CALIOP, an airborne High Spectral Resolution Lidar (HSRL) instrument, and two further algorithms, the Meteosat Cirrus Detection Algorithm (MeCiDA-2) and the Algorithm for the Physical Investigation of Clouds with SEVIRI (APICS) using the SEVIRI instrument was accomplished. The validation of COCS has proven that it is well suited to detect thin cirrus clouds and to derive their ice optical thickness and top altitude at a temporal resolution of 15 min during day and night time with high accuracy and sensitivity as well as high detection efficiencies (98 % at $\tau = 0.1$) and low false alarm rates (~ 5 % at $\tau = 0.1$). The standard deviations were calculated to be $\sigma_\tau = 0.25$ for cirrus ice optical thickness and $\sigma_z = 750$ m for cirrus top altitude. Another advantage is the low runtime of around 500 s for one full MSG disc with 3712 x 3712 pixels on a common office computer, which made the computation of five years of cirrus ice optical thickness and top altitude possible. For the first time, a dataset derived by a passive geostationary satellite containing ice optical thickness and top altitude of optically thin cirrus clouds ($\tau \geq 0.1$) with a very high temporal resolution with good spatial resolution, high sensitivity, and high accuracy could be produced. However, the retrieval of ice optical thickness is limited to $\tau = 2.5$, since the backscatter signal of the spaceborne lidar CALIOP used for the

training dataset gets attenuated and is therefore unable to penetrate thicker clouds.

For the years 2006 to 2010 COCS was applied on SEVIRI measurements. This dataset is analysed in order to investigate the diurnal cycles in cirrus coverage and ice optical thickness. For this purpose, five different regions were defined. Two regions over land surface dominated by convective atmospheric features, and three regions over the North and South Atlantic Ocean aiming to represent the diurnal cycle of cirrus clouds with the lower influence of solar insolation.

In the continental regions, the Mediterranean (MED) and the South African (SAC) region, cirrus cloud coverage and ice optical thickness are dominated by maxima in the afternoon, while the minimum is located in the early morning. In the MED the coverage varies from 23 % to 25 %. The cirrus coverage over the SAC region shows lower coverage with values from 11 % to 16 %. A similar diurnal cycle is found for the cirrus ice optical thickness in the SAC region, where a maximum of $\tau = 0.12$. The diurnal cycle of cirrus coverage in the MED is stronger influenced by thin cirrus clouds ($0.1 \leq \tau < 0.5$) and therefore the diurnal cycle of mean cirrus ice optical thickness shows a lower amplitude compared to the SAC with a maximum of $\tau = 0.14$.

As opposed to the two convective dominated regions, the diurnal cycle of cirrus cloud coverage and cirrus optical thickness over the three maritime regions shows different diurnal cycles. Two equally sized regions were defined over the North and South Atlantic, NAR and SAR1 respectively. Finally the SAR2 region over the South Atlantic was defined to cover 90° of latitude. In the SAR2 region a double-wave diurnal cycle in the total cirrus coverage is found with two maxima and two minima. At around 05:00 and 18:00 LT the maximum coverage reaches values of up to 40 %, while the two minima at 00:00 and 11:00 LT show values of 38 %. The diurnal cycle of ice optical thickness is slightly shifted in time, but has a similar shape with small variations between $\tau_{min} = 0.19$ to $\tau_{max} = 0.20$. The cirrus coverage in the SAR1 region shows a similar curve of cirrus coverage and ice optical thickness. An offset in the coverage of -1 % is detected in the cirrus coverage compared to the SAR2 with an ice optical thickness between $\tau_{min} = 0.20$ and $\tau_{max} = 0.21$ in the SAR1.

Over the NAR region the cirrus coverage also follows a curve with two maxima at 05:00 and 15:00 LT, and two minima at 10:30 and 22:00 LT. The coverage varies from its minima of 38 % to its maxima of 40 %. The ice optical thickness follows a different diurnal cycle than in the SAR1 and SAR2 regions. Two minima are found around 10:00 and 21:00 LT with an ice optical thickness of 0.19, which are followed by two maxima at 05:00 and 16:00 LT with values of up to 0.20.

Since COCS is a passive remote sensing algorithm developed by utilizing active remote sensing, it is likely to detect more cirrus clouds than algorithms based on purely passive remote sensing sensors (Section 2.2.3 and 6.2).

The results (e.g. cirrus coverage) of COCS retrieved for the year 2010 were compared

to the forecasts of high cloud coverage of the Integrated Forecast System (IFS) of the European Centre for Medium Weather Forecast (ECMWF) to confirm the retrieved coverage and its variations. Tompkins et al. [2007] introduced a new parametrization for ice supersaturation to the IFS, which is demonstrated to increase upper-tropospheric humidity, decrease high-level cloud cover and cloud ice amounts. The comparison of two of the defined regions, MED and SAC, were found to show good agreement in the diurnal cycle even though the temporal resolution of the used forecasts is limited to three hours. For the South Atlantic regions and the SAC, the forecasts of high cloud coverage by the IFS is found to differ by only 4 – 7 % from the cirrus cloud coverage detected by COCS. Only the MED region shows higher discrepancies of up to 9 %. While the ECMWF forecasts are able to retrieve the convective influenced diurnal cycle in MED and SAC, especially the second part of the diurnal cycle in the non-convective maritime regions differs strongly from the results of the COCS algorithm as well as the amplitude.

In the North Atlantic region the IFS calculates high cloud coverage of up to 39 %, while COCS detects cirrus clouds at a value of up to 46 %. Also strong differences in the diurnal cycle with varying maxima and minima were found. Thus, the specific characteristic of the NAR had to be taken into account:

During the ESA-DUE Project CONTRAILS, the European Air Traffic Control (EUROCONTROL) provided a dataset of Air Traffic Density (ATD) for six weeks in 2004 with a temporal resolution of 15 min and a spatial resolution of $0.25^\circ \times 0.25^\circ$. Based on this dataset a representative diurnal cycle of ATD in NAR, where a peak in ATD is present for the eastbound transatlantic flights at 04:00 UTC and another one at 13:00 UTC representing the westbound traffic, Graf et al. [2009] found first evidence of the influence of air traffic, when the air traffic density in NAR is shown to result in changes in the diurnal cycle of the cirrus coverage.

With the high accuracy and sensitivity of COCS, the two equally sized regions, NAR and SAR1, are compared in order to retrieve informations about the footprint of aviation in the diurnal cycle of cirrus coverage and cirrus optical thickness. NAR is shown to have differences in the cirrus coverage of up to 1.5 % compared to SAR1, which is present in two maxima following the air traffic density along the North Atlantic airline. Nevertheless, the diurnal cycle of ice optical thickness shows only low differences.

With COCS it is possible to separate single classes of cirrus ice optical thickness and to calculate the diurnal cycle of e.g. thin, medium, and thick cirrus clouds. Especially thin cirrus clouds ($0.1 \leq \tau < 0.5$) have a 3% higher coverage in the NAR than in the SAR1, while the occurrence of thick cirrus ($1.0 \leq \tau \leq 2.5$) clouds is reduced by almost 2%. Furthermore, the cirrus coverage differences for thin and medium ($0.5 \leq \tau < 1.0$) cirrus clouds show a strong diurnal cycle, which appears to be highly connected to the diurnal cycle of air traffic density in NAR.

Outlook

This new approach on retrieving cirrus coverage on the one and properties of the detected cirrus clouds on the other hand has shown that it is able to detect especially thin cirrus clouds. Hence the quality of retrieved ice optical thickness is limited for example in convective situation, where cirrus anvils are produced with high vertical extension and high ice optical thickness. Therefore a combination of both, the COCS algorithm and APICS are highly desirable in order to detect thin cirrus clouds, but also to retrieve correct optical properties even of those thick cirrus systems and water clouds at least during daytime. With the increased detection efficiency compared to MeCiDA-2 (Section 4.2.1) APICS would be able to retrieve the optical thickness and effective radius of thin cirrus clouds on the one hand. On the other hand convection is mostly initiated during daytime, which would enable the combination of APICS and COCS to retrieve temporally resolved insights on the formation and the decay of convective cirrus clouds. The data processed by COCS are also useful to track single cirrus clouds in order investigate their life cycle and changing microphysical properties.

For further studies of contrails and contrail cirrus clouds, their formation, evolution, and decay, the processing of rapid scan data of SEVIRI with a temporal resolution of five minutes was already started. Based on the contrails and contrail cirrus identified by the Automatic Contrail Tracking Algorithm (ACTA) [Vazquez-Navarro et al., 2010], this dataset of cirrus optical thickness will be used to retrieve information on the life cycle of contrails and their optical properties and therefore help to estimate the influence of aviation on climate.

The validation with the airborne HSRL and APICS has shown good agreement, even though the backpropagation neural network of the COCS algorithm was trained with the CALIOP Cloud Layer products version 2. Lately, a new five-dimensional (5D) PDF-based cloud and aerosol discrimination (CAD) algorithm has been developed for use in the version 3 CALIPSO lidar data release, [Liu et al., 2010], which showed several improvements. Therefore an update of the training dataset is planned for future works with COCS.

Additionally an adaptation of the retrieval principle of COCS to other spaceborne radiometers, such as the Advanced Baseline Imager (ABI) onboard the future NOAA/NASA satellite GOES-R (scheduled for launch in 2015), are possible as well as a synergetic use of the three instruments, the Multi-Spectral Imager, the Atmospheric Lidar (ATLID), and the Cloud Profiling Radar (CPR) aboard ESA's EarthCARE satellite (scheduled for launch in 2015).

Appendix

Acronyms

ABI	Advanced Baseline Imager
ACTA	Automatic Contrail Tracking Algorithm
APICS	Algorithm for the Physical Investigation of Clouds with SEVIRI
ATD	Air Traffic Density
ATLID	Atmospheric Lidar
BT	Brightness Temperature
BTD	Brightness Temperature Difference
CALIOP	Cloud-Aerosol Lidar with Orthogonal Polarization
CALIPSO	Cloud-Aerosol Lidar and Infrared Pathfinder Satellite Observations
CC-VEX	CALIPSO-Cloudsat Validation Experiment
CMA	Cloud Model Algorithm
COCS	Cirrus Optical properties derived from CALIOP and SEVIRI during day and night time
CPL	Cloud Physics Lidar
CPR	Cloud Profiling Radar
CREW3	2011 EUMETSAT Cloud Retrieval Evaluation Workshop 3
DJF	December, January, February
DLR	German Aerospace Centre (Deutsches Zentrum für Luft- und Raumfahrt)
DWD	German Weather Service (Deutscher Wetterdienst)
ECMWF	European Centre for Medium-Weather Forecasts
ESA	European Space Agency
EUMETSAT	European Organisation for the Exploitation of Meteorological Satellites
EUROCONTROL	European Air Traffic Control
GMAO	Global Modelling and Assimilation Office
GOES	Geostationary Orbiting Environmental Satellites

HERA	Hybrid Extinction Retrieval Algorithm
HIRS	High Resolution Infrared Radiation Sounder
HRV	High Resolution Visible
HSRL	High Spectral Resolution Lidar
IDL	Interactive Data Language
IFS	Integrated Forecast System
IIR	Imaging Infrared Radiometer
IOT	ice Optical Thickness
IPCC	Intergovernmental Panel on Climate Change
IR	Infrared
ISCCP	International Satellite Cloud Climatology Project
ITCZ	Innertropical Convergence Zone
JJA	June, July, August
LASER	Light Amplification by Stimulated Emission of Radiation
LIDAR	Light Detection and Ranging
LITE	Lidar In-space Technology Experiment
LR	Low Resolution
LT	Local Time
MAM	March, April, May
MBV	Measured Backscatter Variation
MECiDA-2	Meteosat Cirrus Detection Algorithm 2
MED	Mediterranean region
MODIS	Moderate-Resolution Imaging Spectroradiometer
MSE	Mean Square Error
MSG	Meteosat Second Generation
NASA	National Aeronautic and Space Administration
NAR	North Atlantic Region
Nd:YAG	Neodymium doped Yttrium Aluminium Garnet
NIR	Near-Infrared
NOAA	National Oceanic and Atmospheric Administration
PAZI	Particles and Cirrus Clouds
RADAR	Radio Detection and Ranging
RF	Radiative Forcing
RSS	Rapid Scan Service
SAC	South African Region
SAR1	South Atlantic Region, small
SAR2	South Atlantic Region, large
SCA	Scene Classification Algorithm
SEVIRI	Spinning Enhanced Visible and Infrared Imager

SIBYL	Selective Iterated Boundary Locator
SON	September, October, November
STD	Standard Deviation
TIROS-N	Television Infrared Observation Satellite-N
TOA	Top of Atmosphere
TOVS	TIROS-N Observational Vertical Sounder
UTC	Universal Time Coordinated
VFM	Vertical Feature Mask
VAS	VISSR Atmospheric Sounder
VIS	Visible
VISSR	Visible Infrared Spin Scan Radiometer
WFC	Wide Field Camera
WMO	World Meteorological Organisation
WV	Water Vapour

Symbols

a	Absorptivity	
A	Area	m^2
A_0	Collecting area of the lidar telescope	m^2
A_p	projected cross-section area	m^2
B	Blackbody radiance	$J s^{-1} m^{-2}$
C	Lidar calibration factor	
E	Energy	J
F	Irradiance	$J s^{-1} m^{-2}$
f	Frequency	s^{-1}
g	Scale parameter	
G_A	Amplifier gain	
k	wave number	
K	Instrument constant	
L	Radiance	$W m^{-2} sr^{-1}$
m	Refractivity	
n	Refractive index	
P	Received lidar signal	
\check{P}	Phase function	
Q_a	Absorption efficiency	
Q_s	Scattering efficiency	
r	Radius	m
r_{eff}	Effective radius	m
R	Distance/range	m
R'	Attenuated scattering ratio	
ΔR	Range resolution	m
R_S	Radius of the Sun	m
s	Distance	
S	Lidar ratio	
t	Time	s
t_s	Transmission	
T	Temperature	K
V	Volume	m^3
W	Weighting function	
z	Altitude/vertical distance	m

Greek Symbols

α	Extinction coefficient	m^{-1}
α_a	Absorption coefficient	$m^{-1}sr^{-1}$
α_m	Molecular extinction coefficient	m^{-1}
α_p	Particulate extinction coefficient	m^{-1}
α_s	Scattering coefficient	$m^{-1}sr^{-1}$
β	Backscatter coefficient	$m^{-1}sr^{-1}$
β'	Attenuated backscatter coefficient	$m^{-1}sr^{-1}$
β_m	Molecular backscatter coefficient	$m^{-1}sr^{-1}$
β_p	Particulate backscatter coefficient	$m^{-1}sr^{-1}$
ϵ	Emissivity	
η	learning rate	
$\gamma_{feature}$	Integrated attenuated backscatter	$m^{-1}sr^{-1}$
γ'	Integrated attenuated backscatter	$m^{-1}sr^{-1}$
λ	Wavelength	m
ν	Wave number	m^{-1}
ω_0	single-scattering-albedo	
ω_i	synaptic weight	
Φ	Radiation power	$J s^{-1}$
ρ	Volume density	$\frac{kg}{m^{-3}}$
σ_s	Scattering cross section	$m^2 sr^{-1}$
τ	Optical thickness	

Constants

Velocity of light	$c = 299,792,458$	$\frac{m}{s}$
Planck constant	$h = 6.62606957 \cdot 10^{-34}$	Js
Boltzmann constant	$k_B = 1.381 \cdot 10^{-23}$	$\frac{J}{K}$
Stefan-Boltzmann constant	$\sigma = 5.678 \cdot 10^{-8}$	$\frac{W}{m^2 K^4}$

Bibliography

- T. P. Ackerman, K.-N. Liou, F. P. J. Valero, and L. Pfister. Heating Rates in Tropical Anvils. *J. Atmos. Sci.*, 45(10):1606–1623, May 1988. ISSN 0022-4928. doi: 10.1175/1520-0469(1988)045<1606:HRITA>2.0.CO;2. URL [http://journals.ametsoc.org/doi/abs/10.1175/1520-0469\(1988\)045<1606:HRITA>2.0.CO;2](http://journals.ametsoc.org/doi/abs/10.1175/1520-0469(1988)045<1606:HRITA>2.0.CO;2).
- A. Ansmann, F. Wagner, D. Althausen, D. Müller, A. Herber, and U. Wandinger. European pollution outbreaks during ACE 2: Lofted aerosol plumes observed with Raman lidar at the Portuguese coast. *J. Geophys. Res.*, 106(D18):20725–20733, 2001. ISSN 0148-0227. doi: 10.1029/2000JD000091. URL <http://www.agu.org/pubs/crossref/2001/2000JD000091.shtml>.
- H. Appleman. The formation of exhaust contrails by jet aircraft. *B. Am. Meteorol. Soc.*, 34:14–20, 1953.
- A. Arking and J. D. Childs. Retrieval of Cloud Cover Parameters from Multispectral Satellite Images. *J. Clim. Appl. Meteorol.*, 24(4):322–333, Apr. 1985. ISSN 0733-3021. doi: 10.1175/1520-0450(1985)024<0322:ROCCPF>2.0.CO;2. URL [http://journals.ametsoc.org/doi/abs/10.1175/1520-0450\(1985\)024<0322:ROCCPF>2.0.CO;2](http://journals.ametsoc.org/doi/abs/10.1175/1520-0450(1985)024<0322:ROCCPF>2.0.CO;2).
- S. Arrhenius. On the Influence of Carbonic Acid in the Air upon the Temperature of the Ground. *Philosophical Magazine and Journal of Science*, 41(5):237–276, 1896.
- D. Atlas, Z. Wang, and D. P. Duda. Contrails to cirrus: morphology, microphysics, and radiative properties. *J. Appl. Meteorol.*, 45:5–19, 2006.
- Atmospheric Science Data Center. CALIPSO Quality Statements: Lidar Level 2 Cloud and Aerosol Profile Products Version Releases: 2.01, 2.02, 2011. URL http://eosweb.larc.nasa.gov/PRODOCS/calipso/Quality_Summaries/CALIOP_L2ProfileProducts_2.01.html.
- B. A. Baum, R. F. Arduini, B. A. Wielicki, P. Minnis, and S.-C. Tsay. Multilevel cloud retrieval using multispectral HIRS and AVHRR data: Nighttime oceanic analysis. *J. Geophys. Res.*, 99(D3):5499–5514, 1994. ISSN 0148-0227. doi: 10.1029/93JD02856. URL <http://www.agu.org/pubs/crossref/1994/93JD02856.shtml>.

- B. A. Baum, R. A. Frey, G. G. Mace, M. K. Harkey, and P. Yang. Nighttime Multilayered Cloud Detection Using MODIS and ARM Data. *J. Appl. Meteorol.*, 42(7):905–919, July 2003. ISSN 0894-8763. doi: 10.1175/1520-0450(2003)042<0905:NMCDUM>2.0.CO;2. URL [http://journals.ametsoc.org/doi/abs/10.1175/1520-0450\(2003\)042<0905:NMCDUM>2.0.CO;2](http://journals.ametsoc.org/doi/abs/10.1175/1520-0450(2003)042<0905:NMCDUM>2.0.CO;2).
- B. A. Baum, A. J. Heymsfield, P. Yang, and S. T. Bedka. Bulk Scattering Properties for the Remote Sensing of Ice Clouds. Part I: Microphysical Data and Models. *J. Appl. Meteorol.*, 44(12):1885–1895, Dec. 2005. ISSN 0894-8763. doi: 10.1175/JAM2308.1. URL <http://journals.ametsoc.org/doi/pdf/10.1175/JAM2308.1>. [1http://journals.ametsoc.org/doi/abs/10.1175/JAM2308.1](http://journals.ametsoc.org/doi/abs/10.1175/JAM2308.1).
- J. W. Bergman and M. L. Salby. Diurnal Variations of Cloud Cover and Their Relationship to Climatological Conditions. *J. Climate*, 9(11):2802–2820, Nov. 1996. ISSN 0894-8755. doi: 10.1175/1520-0442(1996)009<2802:DVOCCA>2.0.CO;2. URL <http://journals.ametsoc.org/doi/abs/10.1175/1520-0442%281996%29009%3C2802%3ADVVOCCA%3E2.0.CO%3B2>.
- L. Boltzmann. Ableitung des Stefanschen Gesetzes, betreffend die Abhaengigkeit der Waermestrahlung von der Temperatur aus der electromagnetischen Lichttheorie. *Annalen der Physik und Chemie*, 22:291–294, 1884.
- L. Bugliaro, T. Zinner, C. Keil, B. Mayer, R. Hollmann, M. Reuter, and W. Thomas. Validation of cloud property retrievals with simulated satellite radiances: a case study for SEVIRI. *Atmos. Chem. Phys.*, 11(12):5603–5624, June 2011. ISSN 1680-7324. doi: 10.5194/acp-11-5603-2011. URL <http://www.atmos-chem-phys.net/11/5603/2011/>.
- S. Chandrasekhar. *Radiative transfer*. Oxford University Press, UK, 1950. ISBN 978-0486605906.
- S. S. Chen and R. A. Houze. Diurnal variation and life-cycle of deep convective systems over the tropical pacific warm pool. *Q. J. Roy. Meteor. Soc.*, 123(538):357–388, Jan. 1997. ISSN 00359009. doi: 10.1002/qj.49712353806. URL <http://doi.wiley.com/10.1002/qj.49712353806>.
- P. De Mott. Laboratory studies of cirrus cloud processes. In D. Lynch, editor, *Cirrus*, pages 102–135. Oxford Univ. Press, New York, 2002.
- D. R. Dowling and L. F. Radke. A Summary of the Physical Properties of Cirrus Clouds. *J. Appl. Meteorol.*, 29(9):970–978, Sept. 1990. ISSN 0894-8763. doi: 10.1175/1520-0450(1990)029<0970:ASOTPP>2.0.CO;2. URL [http://journals.ametsoc.org/doi/abs/10.1175/1520-0450\(1990\)029<0970:ASOTPP>2.0.CO;2](http://journals.ametsoc.org/doi/abs/10.1175/1520-0450(1990)029<0970:ASOTPP>2.0.CO;2).

- J. P. Duvel. Convection over tropical Africa and the Atlantic Ocean during northern summer. Part I: interannual and diurnal variations. *Mon. Weather Rev.*, 117(12):2782–2799, 1989.
- M. Endemann. ADM-Aeolus: the first spaceborne wind lidar. Technical report, European Space Agency, ESTEC, P.O. Box 229, 2200 AG Noordwijk, The Netherlands, 2006. URL <http://link.aip.org/link/PSISDG/v6409/i1/p64090G/s1&Agg=doi>.
- M. Esselborn. *Lidar-Messung der Extinktion des atmosphärischen Aerosols am Beispiel der Feldstudie SAMUM-1*. Dissertation, Ludwig-Maximilians-Universität München, 2008. URL <http://edoc.ub.uni-muenchen.de/8737>.
- EUMETSAT. A Planned Change to the MSG Level 1.5 Image Product Radiance Definition. Technical Report January, Darmstadt, Germany, 2007.
- EUMETSAT. MSG Level 1 . 5 Image Data Format Description. Technical report, EUMETSAT, Eumetsat, Eumetsat-Allee 1, Darmstadt, Germany, 2010.
- F. Ewald, L. Bugliaro, H. Mannstein, and B. Mayer. Improved cirrus detection for SEVIRI and validation with MODIS. *Atmos. Chem. Phys.*, to be subm, 2012.
- F. G. Fernald, B. M. Herman, and J. A. Reagan. Determination of aerosol height distribution with lidar. *J. Appl. Meteorol.*, 11:482–489, 1972.
- F. Fierli, G. Di Donfrancesco, F. Cairo, V. Marécal, M. Zampieri, E. Orlandi, and G. Durry. Variability of cirrus clouds in a convective outflow during the Hibiscus campaign. *Atmos. Chem. Phys.*, 8(16):4547–4558, Aug. 2008. ISSN 1680-7324. doi: 10.5194/acp-8-4547-2008. URL <http://www.atmos-chem-phys.net/8/4547/2008/>.
- J. S. Foot. Some observations of the optical properties of clouds. II: Cirrus. *Quart. J. Roy. Meteor. Soc.*, 114(479):145–164, Jan. 1988. ISSN 00359009. doi: 10.1002/qj.49711447908. URL <http://doi.wiley.com/10.1002/qj.49711447908>.
- P. Forster, V. Ramaswamy, P. Artaxo, T. Berntsen, and R. Betts. Changes in Atmospheric Constituents and in Radiative Forcing. In *Climate Change 2007: The Physical Science Basis*. Cambridge University Press, Cambridge, UK, 2007.
- P. Geerts. Parallax correction in satellite images, 1999. URL <http://www-das.uwo.edu/~geerts/cwx/notes/chap02/parallax.html>.
- E. Giannakaki, D. S. Balis, V. Amiridis, and S. Kazadzis. Optical and geometrical characteristics of cirrus clouds over a mid-latitude lidar station. *Atmos. Chem. Phys.*, 7(4):9283–9317, July 2007. ISSN 1680-7375. doi: 10.5194/acpd-7-9283-2007. URL <http://www.atmos-chem-phys-discuss.net/7/9283/2007/>.

- K. Graf, H. Mannstein, B. Mayer, and U. Schumann. Some evidence of aviation fingerprint in diurnal cycle of cirrus over the North Atlantic. In *International Conference on Transport, Atmosphere and Climate (TAC-2)*, Aachen, Germany, 2009.
- W. M. Gray and R. W. Jacobson. Diurnal Variation of Deep Cumulus Convection. *Mon. Weather Rev.*, 105(9):1171–1188, Sept. 1977. ISSN 0027-0644. doi: 10.1175/1520-0493(1977)105<1171:DVODCC>2.0.CO;2. URL [http://journals.ametsoc.org/doi/abs/10.1175/1520-0493\(1977\)105<1171:DVODCC>2.0.CO;2](http://journals.ametsoc.org/doi/abs/10.1175/1520-0493(1977)105<1171:DVODCC>2.0.CO;2).
- J. Hallett, W. P. Arnott, and M. P. Balley. Ice crystals in cirrus. In D. Lynch, editor, *Cirrus*, pages 41–77. Oxford Univ. Press, New York, 2002.
- Q. Han, W. B. Rossow, and A. A. Lacis. Near-Global Survey of Effective Droplet Radii in Liquid Water Clouds Using ISCCP Data. *J. Climate*, 7(4):465–497, Apr. 1994. ISSN 0894-8755. doi: 10.1175/1520-0442(1994)007<0465:NGSOED>2.0.CO;2. URL [http://journals.ametsoc.org/doi/abs/10.1175/1520-0442\(1994\)007<0465:NGSOED>2.0.CO;2](http://journals.ametsoc.org/doi/abs/10.1175/1520-0442(1994)007<0465:NGSOED>2.0.CO;2).
- Q. Han, R. Welch, J. Chou, W. Rossow, and A. White. Validation of Satellite Retrievals of Cloud Microphysics and Liquid Water Path Using Observations from FIRE. *J. Atmos. Sci.*, 52(23):4183–4195, Dec. 1995. ISSN 0022-4928. doi: 10.1175/1520-0469(1995)052<4183:VOSROC>2.0.CO;2. URL [http://journals.ametsoc.org/doi/abs/10.1175/1520-0469\(1995\)052<4183:VOSROC>2.0.CO;2](http://journals.ametsoc.org/doi/abs/10.1175/1520-0469(1995)052<4183:VOSROC>2.0.CO;2).
- D. O. Hebb. *The organization of behavior*. Wiley and Sons, 1949. ISBN 0805843000.
- A. J. Heymsfield and G. M. McFarquhar. Mid-latitude and tropical cirrus: Microphysical properties. In D. Lynch, editor, *Cirrus*, pages 78–101. Oxford Univ. Press, New York, 2002.
- D. L. Hlavka, J. E. Yorks, S. A. Young, M. A. Vaughan, R. E. Kuehn, M. J. McGill, and S. D. Rodier. Airborne validation of cirrus cloud properties derived from CALIPSO lidar measurements: Optical properties. *J. Geophys. Res.*, 2012. ISSN 0148-0227. doi: 10.1029/2011JD017053. URL <http://www.agu.org/pubs/crossref/pip/2011JD017053.shtml>.
- Y. Hu, D. Winker, M. Vaughan, B. Lin, A. Omar, C. Trepte, D. Flittner, P. Yang, S. L. Nasiri, B. Baum, R. Holz, W. Sun, Z. Liu, Z. Wang, S. Young, K. Stamnes, J. Huang, and R. Kuehn. CALIPSO/CALIOP Cloud Phase Discrimination Algorithm. *J. Atmos. Ocean. Tech.*, 26(11):2293–2309, Nov. 2009. ISSN 0739-0572. doi: 10.1175/2009JTECHA1280.1. URL <http://journals.ametsoc.org/doi/abs/10.1175/2009JTECHA1280.1>.

- T. Inoue. On the temperature and effective emissivity determination of semi-transparent cirrus clouds by bi-spectral measurements in the 10 μm window region. *J. Meteorol. Soc. Jpn.*, 63(1):88–99, 1985.
- IPCC. Climate Change 2007 - Synthesis Report. Intergovernmental Panel on Climate Change. Technical report, World Meteorological Organization (WMO), 7bis avenue de la Paix, P.O. Box No. 2300, CH- 1211 Geneva 2, Switzerland, 2007.
- A. Kaiser-Weiss. Group for High Resolution Sea Surface Temperature, 2011. URL <https://www.ghrsst.org/data/ghrsst-data-tools/navo-ghrsst-pp-land-sea-mask/>.
- J. R. Key, P. Yang, B. A. Baum, and S. L. Nasiri. Parameterization of shortwave ice cloud optical properties for various particle habits. *J. Geophys. Res.*, 107(D13), 2002. ISSN 0148-0227. doi: 10.1029/2001JD000742. URL <http://www.agu.org/pubs/crossref/2002/2001JD000742.shtml>.
- V. I. Khvorostyanov and K. Sassen. Microphysical processes in cirrus and their impact on radiation. In D. Lynch, editor, *Cirrus*, pages 397–432. Oxford Univ. Press, New York, 2002.
- S. Q. Kidder and T. H. von der Haar. *Satellite meteorology, An introduction*. Academic Press Limited, 24-28 Oval Road, London, U.K., 1995. ISBN 978-0124064300.
- W. Krebs. Analyse des Einflusses des Flugverkehrs auf die natürliche Zirkusbewölkung über Europa, Nordafrik und dem Nordatlantik. *Ludwig-Maximilians Universität München*, 2006.
- W. Krebs, H. Mannstein, L. Bugliaro, and B. Mayer. Technical note: a new day- and night-time Meteosat Second Generation Cirrus Detection Algorithm MeCiDA. *Atmos. Chem. Phys.*, 7(4):10933–10969, July 2007. ISSN 1680-7375. doi: 10.5194/acpd-7-10933-2007. URL <http://www.atmos-chem-phys-discuss.net/7/10933/2007/>.
- N. Lamquin, K. Gierens, C. J. Stubenrauch, and R. Chatterjee. Evaluation of upper tropospheric humidity forecasts from ECMWF using AIRS and CALIPSO data. *Atmos. Chem. Phys.*, 9(5):1779–1793, Mar. 2009. ISSN 1680-7324. doi: 10.5194/acp-9-1779-2009. URL <http://www.atmos-chem-phys.net/9/1779/2009/>.
- K. Lashley. In search of the engram. *Sym. Soc. Exp. Biol.*, 4:454–482, 1950.
- K.-N. Liou. Remote Sensing of the Thickness and Composition of Cirrus Clouds from Satellites. *J. Appl. Meteorol.*, 16(1):91–99, Jan. 1977. ISSN 0021-8952. doi: 10.1175/1520-0450(1977)016<0091:RSOTTA>2.0.CO;2. URL <http://journals.ametsoc.org/doi/abs/10.1175/1520-0450%281977%29016%3C0091%3ARSOTTA%3E2.0.CO%3B2>.

- K. N. Liou. *An introduction to atmospheric radiation*. International geophysics series, 2, vol. 84 edition, 2002. ISBN 978-0124514515.
- K. N. Liou, S. C. Ou, Y. Takano, F. P. J. Valero, and T. P. Ackerman. Remote Sounding of the Tropical Cirrus Cloud Temperature and Optical Depth Using 6.5 and 10.5 μm Radiometers during STEP. *J. Appl. Meteorol.*, 29(8):716–726, Aug. 1990. ISSN 0894-8763. doi: 10.1175/1520-0450(1990)029<0716:RSOTTC>2.0.CO;2. URL [http://journals.ametsoc.org/doi/abs/10.1175/1520-0450\(1990\)029<0716:RSOTTC>2.0.CO;2](http://journals.ametsoc.org/doi/abs/10.1175/1520-0450(1990)029<0716:RSOTTC>2.0.CO;2).
- Z. Liu, N. Sugimoto, and T. Murayama. Extinction-To-Backscatter Ratio of Asian Dust Observed With High-Spectral-Resolution Lidar and Raman Lidar. *Appl. Opt.*, 41(15):2760, 2002. ISSN 0003-6935. doi: 10.1364/AO.41.002760. URL <http://www.opticsinfobase.org/ao/abstract.cfm?uri=ao-41-15-2760>.
- Z. Liu, A. Omar, Y. Hu, M. Vaughan, and D. Winker. CALIOP Algorithm Theoretical Basis Document, Part 3: Scene Classification Algorithms. Technical Report Algorithm Theoretical Basis Document No. PC-SCI-202 Part 3, NASA Langley Research Center, Hampton, Virginia, USA, 2005.
- Z. Liu, R. Kuehn, M. Vaughan, D. Winker, A. Omar, K. Powell, C. Trepte, Y. Hu, and C. Hostetler. The CALIPSO cloud and aerosol discrimination: Version 3 algorithm and test results. In *25th International Lidar Radar Conference*, St. Petersburg, Russia, 2010.
- D. Lynch, K. Sassen, D. Starr, and G. Stephens. *Cirrus: History and definitions*. Oxford Univ. Press, New York, 2002.
- G. G. Mace, M. Deng, B. Soden, and E. Zipser. Association of Tropical Cirrus in the 1015-km Layer with Deep Convective Sources: An Observational Study Combining Millimeter Radar Data and Satellite-Derived Trajectories. *J. Atmos. Sci.*, 63(2):480–503, Feb. 2006. ISSN 0022-4928. doi: 10.1175/JAS3627.1. URL <http://journals.ametsoc.org/doi/abs/10.1175/JAS3627.1>.
- S. J. Masonis, T. L. Anderson, D. S. Covert, V. Kapustin, A. D. Clarks, S. Howell, and K. Moore. A study of extinction-to-backscatter ratio of marine aerosol during the Shoreline Environmental Aerosol Study. *J. Atmos. Ocean. Tech.*, 20(10):1388–1402, 2002.
- B. Mayer and A. Kylling. Technical note: The libRadtran software package for radiative transfer calculations - description and examples of use. *Atmos. Chem. Phys.*, 5(7):1855–1877, July 2005. ISSN 1680-7324. doi: 10.5194/acp-5-1855-2005. URL <http://www.atmos-chem-phys.net/5/1855/2005/>.

- W. S. McCulloch and W. Pitts. A logical calculus of the ideas immanent in nervous activity. *B. Math. Biophys.*, 5:115–133, 1943.
- R. Meerkötter, U. Schumann, D. R. Doelling, P. Minnis, T. Nakajima, and Y. Tsushima. Radiative forcing by contrails. *Ann. Geophys.*, 17(8):1080–1094, 1999. ISSN 1432-0576. doi: 10.1007/s00585-999-1080-7. URL <http://www.ann-geophys.net/17/1080/1999/>.
- W. P. Menzel, W. L. Smith, and T. R. Stewart. Improved Cloud Motion Wind Vector and Altitude Assignment Using VAS. *J. Clim. Appl. Meteorol.*, 22(3):377–384, Mar. 1983. ISSN 0733-3021. doi: 10.1175/1520-0450(1983)022<0377:ICMWVA>2.0.CO;2. URL [http://journals.ametsoc.org/doi/abs/10.1175/1520-0450\(1983\)022<0377:ICMWVA>2.0.CO;2](http://journals.ametsoc.org/doi/abs/10.1175/1520-0450(1983)022<0377:ICMWVA>2.0.CO;2).
- K. Meyer. Optical thickness of tropical cirrus clouds derived from the MODIS 0.66 and 1.375- μm channels. *IEEE T. Geosci. Remote.*, 42(4):833–841, Apr. 2004. ISSN 0196-2892. doi: 10.1109/TGRS.2003.818939. URL <http://ieeexplore.ieee.org/lpdocs/epic03/wrapper.htm?arnumber=1288377>.
- R. Meyer, H. Mannstein, R. Meerkötter, and P. Wendling. Regional radiative forcing by line-shaped contrails derived from satellite data. *J. Geophys. Res.*, 107(D10):15 pp., 2002. ISSN 0148-0227. doi: 10.1029/2001JD000426. URL <http://www.agu.org/pubs/crossref/2002/2001JD000426.shtml>.
- P. Minnis, J. K. Ayers, R. Palikonda, and D. Phan. Contrails, Cirrus Trends, and Climate. *J. Climate*, 17(8):1671–1685, Apr. 2004. ISSN 0894-8755. doi: 10.1175/1520-0442(2004)017<1671:CCTAC>2.0.CO;2. URL <http://journals.ametsoc.org/doi/abs/10.1175/1520-0442%282004%29017%3C1671%3ACCTAC%3E2.0.CO%3B2>.
- G. Mioche, D. Josset, J.-F. Gayet, J. Pelon, A. Garnier, A. Minikin, and A. Schwarzenboeck. Validation of the CALIPSO-CALIOP extinction coefficients from in situ observations in midlatitude cirrus clouds during the CIRCLE-2 experiment. *J. Geophys. Res.*, 115, June 2010. ISSN 0148-0227. doi: 10.1029/2009JD012376. URL <http://www.agu.org/pubs/crossref/2010/2009JD012376.shtml>.
- T. Nakajima and M. D. King. Determination of the Optical Thickness and Effective Particle Radius of Clouds from Reflected Solar Radiation Measurements. Part I: Theory. *J. Atmos. Sci.*, 47(15):1878–1893, Aug. 1990. ISSN 0022-4928. doi: 10.1175/1520-0469(1990)047<1878:DOTOTA>2.0.CO;2. URL <http://journals.ametsoc.org/doi/abs/10.1175/1520-0469%281990%29047%3C1878%3ADOTOTA%3E2.0.CO%3B2>.
- A. Ostler. Validierung von optischen Wolkeneigenschaften aus MSG-Daten. Master’s thesis, Ludwig-Maximilians-Universität München, 2011.

- S. P. Palm. Validation of ECMWF global forecast model parameters using GLAS atmospheric channel measurements. *Geophys. Res. Lett.*, 32(22):5, 2005. ISSN 0094-8276. doi: 10.1029/2005GL023535. URL <http://www.agu.org/pubs/crossref/2005/2005GL023535.shtml>.
- G. Petty. *A first course in atmospheric radiation*. Sundog publishing, Madison, Wisconsin, 2nd editio edition, 2006.
- P. Pili. Calibration of SEVIRI. In *2000 EUMETSAT Meteorological Satellite Data Users' Conference*, pages 33–39, Bologna, Italy, 2000. EUMETSAT EUM P29.
- R. G. Pinnick, S. G. Jennings, P. Chýlek, C. Ham, and W. T. Grandy. Backscatter and Extinction in Water Clouds. *J. Geophys. Res.*, 88(C11):6787–6796, 1983. ISSN 0148-0227. doi: 10.1029/JC088iC11p06787. URL <http://www.agu.org/pubs/crossref/1983/JC088iC11p06787.shtml>.
- W. Pitts and W. S. McCulloch. How we know universals the perception of auditory and visual forms. *B. Math. Biophys.*, 9(3):127–147, Sept. 1947. ISSN 0007-4985. doi: 10.1007/BF02478291. URL <http://www.springerlink.com/index/10.1007/BF02478291>.
- M. Planck. Über das Gesetz der Energieverteilung im Normalspektrum. *Annalen der Physik*, 4(553), 1901.
- C. M. R. Platt. Lidar and Radiometric Observations of Cirrus Clouds. *J. Atmos. Sci.*, 30(6):1191–1204, Sept. 1973. ISSN 0022-4928. doi: 10.1175/1520-0469(1973)030<1191:LAROOO>2.0.CO;2. URL <http://journals.ametsoc.org/doi/abs/10.1175/1520-0469%281973%29030%3C1191%3ALAROOO%3E2.0.CO%3B2>.
- C. M. R. Platt, D. M. Winker, M. A. Vaughan, and S. D. Miller. Backscatter-to-Extinction Ratios in the Top Layers of Tropical Mesoscale Convective Systems and in Isolated Cirrus from LITE Observations. *J. Appl. Meteorol.*, 38(9):1330–1345, 1999.
- M. Radová and J. Seidl. PARALLAX APPLICATIONS WHEN COMPARING RADAR AND. In *2008 EUMETSAT Meteorological Satellite Conference*, Darmstadt, Germany, 2008.
- L. Rayleigh. On the scattering of light by small particles. *Philos. Mag.*, 41:447–454, 1871.
- R. R. Rogers, C. A. Hostetler, J. W. Hair, R. A. Ferrare, Z. Liu, M. D. Obland, D. B. Harper, A. L. Cook, K. A. Powell, M. A. Vaughan, and D. M. Winker. Assessment of the CALIPSO Lidar 532 nm attenuated backscatter calibration using the NASA LaRC airborne High Spectral Resolution Lidar. *Atmos. Chem. Phys.*, 11(3):1295–1311, Feb. 2011. ISSN 1680-7324. doi: 10.5194/acp-11-1295-2011. URL <http://www.atmos-chem-phys.net/11/1295/2011/>.

- W. B. Rossow and R. Schiffer. Advances in understanding clouds from ISCCP. *B. Am. Meteorol. Soc.*, 80:2261–2287, 1999.
- K. Sassen and B. S. Cho. Subvisual-Thin Cirrus Lidar Dataset for Satellite Verification and Climatological Research. *J. Appl. Meteorol.*, 31(11):1275–1285, Nov. 1992. ISSN 0894-8763. doi: 10.1175/1520-0450(1992)031<1275:STCLDF>2.0.CO;2. URL [http://journals.ametsoc.org/doi/abs/10.1175/1520-0450\(1992\)031<1275:STCLDF>2.0.CO;2](http://journals.ametsoc.org/doi/abs/10.1175/1520-0450(1992)031<1275:STCLDF>2.0.CO;2).
- K. Sassen and J. M. Comstock. A midlatitude cirrus cloud climatology from the facility for atmospheric remote sensing. Part III: Radiative properties. *J. Atmos. Sci.*, 58(15): 2113–2127, 2001. doi: 10.1175/1520-0469(2001)058.
- K. Sassen and G. G. Mace. Ground based remote sensing of cirrus clouds. In D. Lynch, editor, *Cirrus*, pages 168–195. Oxford Univ. Press, New York, 2002.
- K. Sassen, Z. Wang, and D. Liu. Global distribution of cirrus clouds from CloudSat/Cloud-Aerosol Lidar and Infrared Pathfinder Satellite Observations (CALIPSO) measurements. *J. Geophys. Res.*, 113:1–12, Oct. 2008. ISSN 0148-0227. doi: 10.1029/2008JD009972. URL <http://www.agu.org/pubs/crossref/2008/2008JD009972.shtml>.
- J. Schmetz, P. Pili, S. Tjemkes, D. Just, J. Kerkmann, S. Rota, and A. Ratier. An introduction to Meteosat Second Generation (MSG). *B. Am. Meteorol. Soc.*, 83(7): 977–992, 2002. ISSN 00030007. doi: 10.1175/BAMS-83-7-Schmetz-1. URL <http://journals.ametsoc.org/doi/abs/10.1175/BAMS-83-7-Schmetz-1>.
- E. Schmidt. Die Entstehung von Eisnebel aus den Auspuffgasen von Flugmotoren. *Schriften der Deutschen Akademie der Luftfahrtforschung*, 44:1–15, 1941.
- U. Schumann. Contrail cirrus. In D. Lynch, editor, *Cirrus*, pages 231–255. Oxford Univ. Press, New York, 2002.
- U. Schumann. Formation, properties and climatic effects of contrails. *Comptes Rendus Physique*, 6(4-5):549–565, May 2005. ISSN 16310705. doi: 10.1016/j.crhy.2005.05.002. URL <http://linkinghub.elsevier.com/retrieve/pii/S1631070505000563>.
- B. J. Soden. The diurnal cycle of convection, clouds, and water vapor in the tropical upper troposphere. *Geophys. Res. Lett.*, 27(15):2173, 2000. ISSN 0094-8276. doi: 10.1029/2000GL011436. URL <http://www.agu.org/pubs/crossref/2000/2000GL011436.shtml>.

- J. Stefan. Über die Beziehung zwischen der Wärmestrahlung und der Temperatur. *Sitzungsberichte der mathematisch-naturwissenschaftlichen Classe der kaiserlichen Akademie der Wissenschaften*, 79:391–428, 1879.
- C. J. Stubenrauch, A. Chédin, G. Rädel, N. A. Scott, and S. Serrar. Cloud Properties and Their Seasonal and Diurnal Variability from TOVS Path-B. *J. Climate*, 19(21):5531–5553, Nov. 2006. ISSN 0894-8755. doi: 10.1175/JCLI3929.1. URL <http://journals.ametsoc.org/doi/abs/10.1175/JCLI3929.1>.
- G. Szejwach. Determination of Semi-Transparent Cirrus Cloud Temperature from Infrared Radiances: Application to METEOSAT. *J. Appl. Meteorol.*, 21(3):384–393, Mar. 1982. ISSN 0021-8952. doi: 10.1175/1520-0450(1982)021<0384:DOSTCC>2.0.CO;2. URL [http://journals.ametsoc.org/doi/abs/10.1175/1520-0450\(1982\)021<0384:DOSTCC>2.0.CO;2](http://journals.ametsoc.org/doi/abs/10.1175/1520-0450(1982)021<0384:DOSTCC>2.0.CO;2).
- S. A. Tjemkes. On the conversion from radiances to equivalent brightness temperature. Technical Report October, EUMETSAT, P.O. Box 100555, Darmstadt, Germany, 2005. URL http://www.eumetsat.int/groups/ops/documents/document/pdf_msg_seviri_rad2bright.pdf.
- S. A. Tjemkes and J. Schmetz. Radiative Transfer Simulations for the Thermal Channels of METEOSAT Second. Technical report, EUMETSAT, Am Kavaleriesand 31, Darmstadt, Germany, 1998. URL <http://web.usal.es/~manuel. Quiros/thermalchannelmetsg.pdf>.
- A. M. Tompkins, K. Gierens, and G. Rädel. Ice supersaturation in the ECMWF Integrated Forecast System. *Q. J. Roy. Meteor. Soc.*, 133:53–63, 2007.
- M. Vaughan, D. Winker, and K. Powell. CALIOP Algorithm Theoretical Basis Document, Part 2: Feature Detection and Layer Properties Algorithms. Technical Report Algorithm Theoretical Basis Document No. PC-SCI-202 Part 2, NASA Langley Research Center, Hampton, Virginia, USA, Sept. 2005.
- M. Vaughan, R. E. Kuehn, S. Young, M. J. McGill, Z. Liu, and Y. Hu. Validating Cirrus Clouds Optical Properties retrieved by CALIPSO. In *24th International Lidar Radar Conference*, pages 1090–1093, Boulder, Colorado, USA, 2008.
- M. A. Vaughan, S. Young, D. M. Winker, K. Powell, A. Omar, Z. Liu, Y. Hu, and C. Hostetler. Fully automated analysis of space-based lidar data: an overview of the CALIPSO retrieval algorithms and data products. *Proc. of SPIE*, 5575:16–30, 2004. ISSN 0277786X. doi: 10.1117/12.572024. URL <http://link.aip.org/link/?PSI/5575/16/1&Agg=doi>.

- M. Vazquez-Navarro. *Life cycle of contrails from a time series of geostationary satellite images*. PhD thesis, 2009.
- M. Vazquez-Navarro, H. Mannstein, and B. Mayer. An automatic contrail tracking algorithm. *Atmos. Meas. Tech.*, 3(4):1089–1101, Aug. 2010. ISSN 1867-8548. doi: 10.5194/amt-3-1089-2010. URL <http://www.atmos-meas-tech.net/3/1089/2010/>.
- M. Vazquez-Navarro, B. Mayer, and H. Mannstein. A fast method for the retrieval of integrated longwave and shortwave top-of-atmosphere irradiances from MSG/SEVIRI (RRUMS). *Atmos. Meas. Tech.*, to be subm, 2012.
- K. J. Voss, E. J. Welton, P. K. Quinn, J. Johnson, A. M. Thompson, and H. R. Gordon. Lidar measurements during Aerosols99. *J. Geophys. Res.*, 106(D18):20821–20831, 2001. URL http://saga.pmel.noaa.gov/publications/pdfs/2001/voss_etal_2001b.pdf.
- J. M. Wallace and P. V. Hobbs. *Atmospheric Science: an introductory survey*. Academic Press, 1977.
- C. Wang, P. Yang, B. a. Baum, S. Platnick, A. K. Heidinger, Y. Hu, and R. E. Holz. Retrieval of Ice Cloud Optical Thickness and Effective Particle Size Using a Fast Infrared Radiative Transfer Model. *J. Appl. Meteorol.*, 50(11):2283–2297, Nov. 2011. ISSN 1558-8424. doi: 10.1175/JAMC-D-11-067.1. URL <http://journals.ametsoc.org/doi/abs/10.1175/JAMC-D-11-067.1>.
- C. Weitkamp. *Lidar, Range-Resolved Optical Remote Sensing of the Atmosphere*. Springer, New York, 2005. ISBN 0-387-40075-3.
- P. J. Werbos. *Beyond Regression: New Tools for Prediction and Analysis in the Behavioral Sciences*. PhD thesis, Harvard University, 1974.
- B. A. Wielicki and L. Parker. On the determination of cloud cover from satellite sensors: The effect of sensor spatial resolution. *J. Geophys. Res.*, 97(D12):799–823, 1992.
- D. Winker and M. Vaughan. Vertical distribution of clouds over Hampton, Virginia observed by lidar under the ECLIPS and FIRE ETO programs. *Atmos. Res.*, 34(1-4):117–133, June 1994. ISSN 01698095. doi: 10.1016/0169-8095(94)90084-1. URL <http://linkinghub.elsevier.com/retrieve/pii/0169809594900841>.
- D. Winker, B. Getzewich, and M. Vaughan. Cloud Properties from CALIPSO / CALIOP. In *GEWEX Cloud Assesment*, number June, Berlin, Germany, 2010.
- D. M. Winker, J. Pelon, and M. P. Mc Cormick. The CALIPSO mission: Spaceborne lidar for observation of aerosols and clouds. In *Proc. of SPIE - Lidar Remote Sensing for*

- Industry and Environment Monitoring III, Vol. 4893*, pages 24–25, Hangzhou, China, 2002.
- D. M. Winker, W. H. Hunt, and M. J. McGill. Initial performance assessment of CALIOP. *Geophys. Res. Lett.*, 34(19):L19803, 2007. ISSN 0094-8276. doi: 10.1029/2007GL030135. URL <http://www.agu.org/pubs/crossref/2007/2007GL030135.shtml>.
- D. M. Winker, M. A. Vaughan, A. Omar, Y. Hu, K. A. Powell, Z. Liu, W. H. Hunt, and S. A. Young. Overview of the CALIPSO Mission and CALIOP Data Processing Algorithms. *J. Atmos. Ocean. Tech.*, 26(11):2310–2323, Nov. 2009. ISSN 0739-0572. doi: 10.1175/2009JTECHA1281.1. URL <http://journals.ametsoc.org/doi/abs/10.1175/2009JTECHA1281.1>.
- WMO and World Meteorological Organisation. International Cloud Atlas, Plates. Technical report, WMO, Geneva, 1987.
- WMO and World Meteorological Organisation. International Cloud Atlas, Manual on the Observation of Clouds and other Meteors. Technical report, WMO, Geneva, 1995.
- S. E. Wood, M. B. Baker, and B. D. Swanson. Instrument for studies of homogeneous and heterogeneous ice nucleation in free-falling supercooled water droplets. *Rev. Sci. Instrum.*, 73(11):3988, 2002. ISSN 00346748. doi: 10.1063/1.1511796. URL <http://link.aip.org/link/RSINAK/v73/i11/p3988/s1&Agg=doi>.
- D. P. Wylie. Cirrus and weather: A satellite perspective. In D. Lynch, editor, *Cirrus*, pages 136–146. Oxford Univ. Press, New York, 2002.
- D. P. Wylie and W. P. Menzel. Two Years of Cloud Cover Statistics Using VAS. *J. Climate*, 2(4):380–392, Apr. 1989. ISSN 0894-8755. doi: 10.1175/1520-0442(1989)002<0380:TYOCCS>2.0.CO;2. URL [http://journals.ametsoc.org/doi/abs/10.1175/1520-0442\(1989\)002<0380:TYOCCS>2.0.CO;2](http://journals.ametsoc.org/doi/abs/10.1175/1520-0442(1989)002<0380:TYOCCS>2.0.CO;2).
- D. P. Wylie and W. P. Menzel. Eight years of high cloud statistics using HIRS. *J. Climate*, 12:170–184, 1998.
- S. A. Young. Analysis of lidar backscatter profiles in optically thin clouds. *Appl. Opt.*, 34(30):7019, 1995. ISSN 0003-6935. doi: 10.1364/AO.34.007019. URL <http://www.opticsinfobase.org/abstract.cfm?URI=ao-34-30-7019>.
- S. A. Young, D. M. Winker, M. A. Vaughan, Y. Hu, and R. E. Kuehn. CALIOP Algorithm Theoretical Basis Document, Part 4: Extinction Retrieval Algorithms. Technical report, NASA Langley Research Center, Hampton, Virginia, USA, 2008.

-
- W. Zdunkowski, T. Trautmann, and A. Bott. *Radiation in atmosphere, A course in theoretical meteorology*. Cambridge University Press, New York, 2007.
- A. Zeil. *Simulation Neuronaler Netze*. Oldenbourg Wissenschaftsverlag, 1997. ISBN 978-3486243505.

Danksagung

Diese Arbeit wäre ohne die Hilfe zahlreicher Personen nicht möglich gewesen, bei denen ich mich an dieser Stelle bedanken möchte.

Zuerst möchte ich mich bei meinem Doktorvater Prof. Dr. Mayer dafür bedanken, dass er mir nicht nur die Gelegenheit zur Durchführung dieser Arbeit gegeben hat, sondern auch mit interessanten Ratschlägen, Diskussionen, Anmerkungen und Ideen wesentlich zum Erfolg dieser Arbeit beigetragen hat.

Ein großer Dank gilt Prof. Dr. Schumann, der diese Arbeit am Institut für Physik der Atmosphäre (DLR) erst ermöglicht hat, für seine konstruktiven Verbesserungsvorschläge und die Übernahme des Zweitgutachtens.

Ein ganz besonderer Dank gilt Dr. Mannstein für die Betreuung dieser Arbeit. Seine Hilfsbereitschaft, sein umfassendes Wissen auf dem Gebiet der Meteorologie und Fernerkundung der Atmosphäre, seine Experimentierfreudigkeit und seine wertvollen Ratschläge waren für mich eine unschätzbare Hilfe. Das von ihm in IDL programmierte Neuronale Netz formt die Basis für den in dieser Arbeit entstandenen Algorithmus.

Ebenfalls möchte ich mich bei Dr. Bugliaro für seine immer interessanten Anregungen und für die große und freundliche Hilfe im Umgang mit IDL, MSG und Condor bedanken. Gleicher Dank gilt auch Kaspar Graf.

Einen wesentlichen Beitrag zur Validierung des Algorithmus mit dem HSRL lieferte Andreas Ostler mit seiner gelungenen Masterarbeit, die allerdings ohne die sehr gute Kooperation mit der Abteilung Lidar des Instituts, namentlich Dr. Wirth, nicht möglich gewesen wäre.

Bedanken möchte ich mich auch bei meinem ehemaligen Zimmerkollegen Dr. Hamann, der gerade zu Beginn dieser Arbeit durch seine Bereitschaft zur Beantwortung zahlreicher Fragen und mit Rat und Tat eine große Hilfe war.

Dieser Dank gilt natürlich auch allen Kolleginnen und Kollegen der Abteilung, deren Arbeitsatmosphäre und Zusammenhalt ich sehr zu schätzen gelernt habe und ebenso den Kolleginnen und Kollegen des Meteorologischen Instituts der LMU München.

Ich bedanke mich ganz herzlich bei meinen Eltern, Marion und Hans Jürgen, meinem Bruder Wolfgang, meiner Freundin Mariana und Charly, die mich immer ermutigt haben und für ihre enorme Unterstützung in den schwierigen Zeiten der letzten drei Jahre.

CALIOP/CALIPSO data were obtained from the NASA Langley Research Center Atmospheric Science Data Center. I would like to thank the CALIPSO science team for providing these data.

Lebenslauf

Persönliche Daten:

Name Stephan Kox
geboren am 09.01.1982
in München, Deutschland
Familienstand ledig

Schulbildung:

1988 - 1992 Grundschule Putzbrunn
1992 - 2002 Gymnasium Neubiberg (Abschluss: Abitur)

Studium:

Sep. 2003 - Dez. 2008 Studium Meteorologie
an der Ludwig-Maximilians-Universität München (LMU)
Dez. 2008 Diplom in Meteorologie, Diplomarbeit zum Thema
*Development and validation of a multilayer cloud detection
algorithm for the airborne demonstrator of the direct
detection Doppler lidar on ADM-Aeolus.*

Seit Feb. 2009 Doktorand
am Institut für Physik der Atmosphäre, DLR Oberpfaffenhofen

München, den 28.06.2012

